Lehrstuhl für Biomedizinische Physik
Technische Universität München

Quantitative X-ray imaging with high-energy grating interferometry at conventional sources

Adrian Sarapata

Dissertation

July 2015

Supervisors:
Dr. Julia Herzen
Dr. Dan Stutman
Prof. Dr. Franz Pfeiffer

Technische Universität München

Technische Universität München
Physik Department
Lehrstuhl für Biomedizinische Physik

Quantitative X-ray imaging with high-energy grating interferometry at conventional sources

Adrian Sarapata

Vollständiger Abdruck der von der Fakultät für Physik der Technischen Universität München zur Erlangung des akademischen Grades eines

Doktors der Naturwissenschaften (Dr. rer. nat.)

genehmigten Dissertation.

Vorsitzender:	Univ.-Prof. Dr. Björn Garbrecht
Prüfer der Dissertation:	1. Univ.-Prof. Dr. Franz Pfeiffer
	2. Univ.-Prof. Dr. Jan Wilkens

Die Dissertation wurde am 13.07.20015 bei der Technischen Universität München eingereicht und durch die Fakultät für Physik am 22.07.2015 angenommen.

Dla moich ukochanych - Babci i Mamy.

Abstract

This thesis presents research results on high-energy X-ray grating interferometry and its implementation at conventional polychromatic X-ray sources. Identical to other phase-sensitive techniques, the image contrast is created based on refraction of X-rays propagating through matter, and not their absorption. Demonstrated for the first time over a decade ago, grating interferometry provides increased contrast over absorption-based imaging at photon energies below 30-40 keV, and of low-atomic-number materials, mainly soft tissues. However, imaging of large and dense objects requires X-ray photons with higher energies. Therefore, the feasibility of this technique with high-penetration-depth photons above 40 keV is being investigated.

In this work, the potential of high-energy grating interferometry is evaluated by means of experiments performed with X-ray spectra comprised of high energy photons (>45 keV). Several important questions concerning the applicability and possible benefits of the technique for medical imaging and materials science research are answered.

The quantitativeness and accuracy of the technique is assessed with measurements performed both in projection and tomography mode. In order to ensure fast and reliable measurements of the electron density on a vast number of various homogeneous materials, a special sample geometry is presented and its validity confirmed experimentally. Further, quantitative measurements are extended to a tomography mode. Quantitative results of phase-contrast CT scans show the changing complementarity of attenuation and phase-contrast images of materials with various atomic numbers at photon energies of 45 keV and above. The benefits of a high-energy X-ray phase-contrast CT system over conventional attenuation-based CT are presented, with imaging results of a part of a human cervical spine with intervertebral discs in between the vertebral bones. The phase-contrast tomogram reveals the internal structure of the discs, a feature expected to be seen only in magnetic resonance imaging. Furthermore, based on the experimental values of electron density obtained with the technique, dedicated phase-contrast imaging phantoms are designed, presented and characterized experimentally. Their benefits for phase-contrast CT system characterizations are reported. Moreover, a simple design change applied to the interferometer is shown to provide phase-contrast CT images with increased soft-tissue contrast at (as estimated by computer simulation) dose levels comparable to conventional attenuation-based CT. Finally, the technique's big potential for imaging porous and composite materials is indicated by a proof-of-concept measurement performed on a concrete sample.

The results presented in this thesis characterize the performance of grating-based imaging at photon energies above 40 keV; additionally, they indicate the potential of the method for specific biomedical applications which take advantage of high-resolution soft-tissue imaging, and for imaging highly heterogeneous and dense porous materials such as concrete.

Table of Contents

1 Introduction **1**

I Theoretical background **6**

2 Imaging with X-rays **7**
2.1 Interaction of X-rays with matter . . . 7
2.1.1 Attenuation and phase shift . . . 8
2.1.2 Complex atomic scattering factor . . . 9
2.2 Attenuation-contrast imaging . . . 10
2.2.1 Image contrast formation . . . 10
2.2.2 Total attenuation cross section . . . 11
2.3 Phase-sensitive imaging . . . 13
2.3.1 Phase shift and refraction . . . 13
2.3.2 Phase-sensitive techniques . . . 14

3 X-ray grating interferometry **19**
3.1 Principles . . . 20
3.1.1 Talbot (self-imaging) effect . . . 20
3.2 Components of a Talbot-Lau interferometer . . . 22
3.2.1 The phase grating . . . 22
3.2.2 The analyzer grating . . . 23
3.2.3 The source grating . . . 23
3.3 Data collection and analysis . . . 24
3.3.1 Phase stepping . . . 24
3.3.2 Fourier processing . . . 26
3.3.3 Three contrast channels . . . 26
3.4 Operation at high X-ray energy . . . 29
3.4.1 Influence on fringe visibility . . . 30
3.5 High-energy experimental implementation . . . 32

II Experimental results **34**

4 Quantitative measurements in radiography **35**
4.1 Introduction and motivation . . . 36
4.2 Materials and methods . . . 37
4.2.1 Measurement of the electron density . . . 37
4.2.2 Data acquisition and analysis . . . 39

4.2.3 Samples . . . 40
4.3 Results and discussions . . . 41
4.3.1 Synchrotron source . . . 42
4.3.2 Laboratory source . . . 44
4.4 Conclusions and summary . . . 44

5 Quantitative computed tomography 46
5.1 Introduction . . . 47
5.2 Materials and methods . . . 48
5.2.1 Grating size as a limiting factor of a large field of view . . . 48
5.2.2 Image contrast dependence / formation . . . 49
5.2.3 Samples . . . 51
5.2.4 Experimental setup, data acquisition and analysis . . . 51
5.3 Results and discussions . . . 53
5.3.1 Low-Z materials phantom . . . 53
5.3.2 High-Z materials phantom . . . 55
5.3.3 Intervertebral discs . . . 58
5.4 Conclusions . . . 59

6 Design of dedicated phase-contrast phantoms 61
6.1 Introduction . . . 61
6.2 Breast tissue-substitute materials . . . 63
6.2.1 Electron density of breast tissue in literature . . . 63
6.2.2 Results and discussions . . . 66
6.2.3 Summary . . . 66
6.3 CT phantoms for image quality assesment . . . 67
6.3.1 Quantitative phantom . . . 68
6.3.2 Low-contrast phantom . . . 68
6.3.3 Results and discussions . . . 70
6.4 Conclusions . . . 73

7 Towards dose-relevant CT 74
7.1 Introduction . . . 75
7.2 Materials and methods . . . 76
7.2.1 Experimental setup . . . 76
7.2.2 Image acquisition and processing . . . 77
7.2.3 Samples . . . 80
7.2.4 Experiments . . . 80
7.2.5 Monte Carlo estimation of dose . . . 81
7.3 Results and discussions . . . 81
7.3.1 Fringe visibility . . . 81
7.3.2 Dose estimation by computer simulation . . . 84

7.3.3 Comparison between the two phase-stepping methods 84
7.3.4 High- versus low-visibility system comparison 85
7.3.5 Soft tissue phantom at different exposure times 86
7.3.6 Soft tissue phantom filled with water 88
7.4 Conclusions 90

8 Multi-contrast imaging for materials science applications 92
8.1 Introduction 93
8.2 Materials and methods 94
8.2.1 Experimental setup 94
8.2.2 Sample 95
8.2.3 Image acquisition and processing 95
8.2.4 Analysis of spatial resolution 95
8.3 Results 96
8.4 Discussions and conclusions 99

9 Summary and outlook 102

References 105

List of publications 121

List of scientific presentations 122

Acknowledgements 123

Chapter 1
Introduction

Since the discovery of X-rays by W. C. Röntgen in 1895, X-ray imaging has become an important tool in many fields of research and medical imaging. Their high penetration power, short wavelengths, which result in high spatial resolutions, and easy accessibility thanks to affordable lab-based sources enabled the technique to spread widely across various disciplines, such as medical diagnostics, biomedical research, materials science, security screening, and so forth.

Conventionally, images are created based on varying attenuation properties of different elements and materials densities inside a human body or an arbitrary object. An object illuminated with an X-ray beam modulates its intensity such that it creates a "shadow" which can be detected with analog film or a digital detector sensitive to X-rays. In conventional radiography only a two-dimensional image is produced. In computed tomography, the tube and the detector are rotated around the object so that multiple images can be acquired, resulting in a three-dimensional visualization. However, when the object's attenuation is not strong enough or the differences in density and elemental composition are small, the contrast generated by X-ray attenuation is insufficient.

Since phase-sensitive techniques rely on a different physical phenomenon than attenuation, the possibility for increased contrast exists. For a long time phase-sensitive imaging has been, however, reserved only to the visible part of the electromagnetic spectrum because of difficulties in creating optical elements efficient enough in the short wavelengths of X-rays. This all changed in 1965 with a demonstration of the first interferometer in the hard X-ray regime by [Bonse & Hart 1965]. Although very impractical at the time, it fortunately caught the necessary attention and phase-sensitive imaging has been under constant development since then. Various phase-sensitive techniques emerged, varying in experimental means of measuring the phase front and its changes [Fitzgerald 2000, Momose 2005]. At the beginning, most of them required highly spatially coherent beams, which made the possible use cases very limited. Performance of phase-sensitive techniques excels at synchrotron sources, which provide high brilliance and highly coherent radiation. Contrast of low-absorbing objects was shown to increase tenfold and beyond [Pfeiffer *et al.* 2007a, Schulz *et al.* 2010, Zanette *et al.* 2013]. Unfortunately, access to synchrotron facilities is very limited as there are approximately only 70 synchrotrons around the world in various stages of development. Their operation costs are very high and therefore their accessibility is limited.

Of all X-ray phase-sensitive techniques only a handful can be operated with conventional, polychromatic X-ray sources, such as X-ray tubes used standardly in hospitals and materials science labs. Theoretically, by slitting down the exit window of an X-ray tube, a beam can be produced that is spatially coherent enough to work with any of the techniques. However, the practicality of such systems is questionable. The already low flux of such sources behind a single small aperture becomes practically unusable since its low throughput requires exposure times of up to tens of seconds per single image.

The method utilized in this work, *Talbot-Lau grating interferometry*, does not have this drawback. It can be successfully used with conventional sources because the coherence requirements are not as strict as in the other techniques. Therefore, "only" half of the photons are lost in the process needed to meet the coherence requirements, which is still sufficient for a realistic operation from the exposure time point of view. After its demonstration by [Pfeiffer *et al.* 2006] it caught a lot of attention among research groups around the world. First demonstrations showed huge gains in image contrast [Donath *et al.* 2010] and first medical applications were investigated with hopes for dose-compatible examinations in the near future [Stampanoni *et al.* 2011, Scherer *et al.* 2014].

Because grating interferometry heavily depends on optical elements produced with micrometer precision, called gratings [Reznikova *et al.* 2008, Mohr *et al.* 2012], which are difficult to manufacture for high-energy X-rays, it has been mostly used at X-ray energies below 30-40 keV [Hetterich *et al.* 2014, Willner *et al.* 2014, Herzen *et al.* 2014]. This energy range is enough for experiments performed on dissected tissue samples the size of at most a few centimeters, but could never be suitable for imaging human body parts containing bones, or for materials science applications. Hence, there has always been a need for grating interferometry operated at high X-ray energies. Additionally, operation at high energies can potentially lower the radiation dose delivered to a patient because fewer photons are absorbed in the sample and transfer their energy to the tissue. As phase-contrast techniques rely only on the transmitted part of the radiation, they show great potential as dose-compatible diagnostics tools. It does, however, have its own drawbacks. Photon interaction cross sections fall off pretty quickly with increasing photon energy, and this demands high-quality optical elements such that every available photon carrying the phase-shift information is used in image contrast creation.

In addition to high contrast in the images resulting from the X-ray illumination, the ability to relate the gray values of an image to the physical properties of the investigated sample, such as its mass and electron density, is advantageous and therefore desirable in many research fields. Grating interferometry allows for simultaneous determination of the linear attenuation coefficient and the refractive index decrement distribution inside an object in three dimensions [Herzen *et al.* 2009]. The refractive index decrement can be further related to the electron density distribution, and

by combining the two parameters, effective atomic number of the materials can be determined [Qi *et al.* 2010].

As grating fabrication processes improve, grating interferometry becomes more and more feasible at higher X-ray energies. New possible applications are being investigated thanks to the higher penetration depth of photons above 40 keV. For instance, grating interferometry at 82 and 130 keV photon energy using a synchrotron source has already been demonstrated [Willner *et al.* 2013, Ruiz-Yaniz *et al.* 2015]. However, as already mentioned, access to synchrotron radiation sources is severely limited because of their high operation costs. The first demonstration of a grating interferometer operated with a conventional X-ray source and a polychromatic spectrum with a mean energy of 60 keV was demonstrated earlier in [Donath *et al.* 2009b], but due to limitations in the grating fabrication process at that time, performance of the interferometer was inferior and not sufficient to perform imaging with satisfactory image quality gain between the phase and the attenuation-contrast reconstructions. A slightly different approach have been presented to build improved laboratory systems [Thuering *et al.* 2014], but the field of view in this case is severely limited. Therefore, a high-energy phase-contrast CT system using a conventional X-ray source with a big field of view and a high optical performance is desirable.

The aim of this PhD thesis was to implement, characterize and evaluate possible applications of high-energy X-ray Talbot-Lau interferometry with a conventional, polychromatic X-ray source. With the help of other members of the Chair of Biomedical Physics of the Technical University Munich, the complete processing chain has been developed: beginning with semi-automatic data acquisition, and concluding with quantitative tomography reconstructions of three different physical quantities. Subsequently, the technique was investigated for its advantages, practicality, complementarity, and improvements in image quality of phase-contrast and dark-field modalities over standard attenuation-based imaging. Possible applications which could benefit the most from the technique were experimentally assessed; results of these experiments are presented in Part II of this thesis.

This thesis is structured as follows. After the introduction, **Chapter 2** outlines the theoretical background of X-ray imaging and presents the corresponding mathematical formalism. **Chapter 3** explains the operating principles of X-ray grating interferometry and the processing chain used to acquire the three different contrast modalities. Section 3.5 describes the experimental setup used to obtain the majority of the results reported in this thesis.

Chapters 4 to 8 contain the main experimental results:

Chapter 4 presents a special sample geometry for fast and reliable projection-only-based measurements of electron density of homogeneous objects. The experimental results for nearly 20 samples are shown and further compared with point-of-reference measurements obtained using monochromatic synchrotron radiation. Limitations of the projection-only-based method are discussed.

Chapter 5 extends the quantitative measurements to a tomography mode and evaluates the complementarity of attenuation and phase-contrast images of materials with various atomic numbers at photon energies of 45 keV and above. The benefit of a high-energy X-ray phase-contrast system over conventional attenuation-based CT is showcased by the phase-contrast tomography of a part of a human cervical spine with intervertebral discs surrounded by bones and various soft tissue types.

Chapter 6 discusses the design and experimental evaluation of dedicated phase-contrast imaging phantoms. Polymer plastics suitable as tissue-substitute materials for X-ray phase-contrast imaging are chosen based on their refractive properties. Imaging results of both a low-contrast and an image-quality phantom are presented, and their benefits for a PC-CT system characterization are reported.

Chapter 7 describes a possible design change for the high-energy interferometer which improves its optical performance and contributes to making the technique dose-relevant and clinically applicable. A few low-dose comparisons of phase-contrast CT images with attenuation-based CT images show greatly improved soft tissue contrast in the former.

Chapter 8 investigates possible applications of high-energy X-ray grating inter-

ferometry for porous and composite materials. Multi-contrast grating-based tomography of a concrete sample demonstrates that the supplementary information provided by phase-contrast and dark-field images improves differentiation of material phases and visibility of micro-cracks. Prospects for further studies on porous and composite materials are discussed.

The scientific results are summarized and perspectives are discussed in Chapter 9.

Part I

Theoretical background

Chapter 2

Imaging with X-rays

Contents

2.1 Interaction of X-rays with matter 7

2.1.1 Attenuation and phase shift 8

2.1.2 Complex atomic scattering factor 9

2.2 Attenuation-contrast imaging 10

2.2.1 Image contrast formation 10

2.2.2 Total attenuation cross section 11

2.3 Phase-sensitive imaging 13

2.3.1 Phase shift and refraction 13

2.3.2 Phase-sensitive techniques 14

X-rays have been used for imaging since their discovery in 1895 by Röntgen. In fact, the first documented experiment with X-rays was a projection image of a human hand recorded on analog film. Their high penetration power has been exploited since then.

This chapter presents the fundamentals of imaging with X-rays. Section 2.1 describes the basic principles of X-ray interaction with matter, including the attenuation and phase shift of the X-ray wave. Section 2.2 describes the contrast formation in attenuation-based imaging. The basic interactions relevant to imaging, namely photoelectric effect, Rayleigh, and Compton scattering, are described in Subsection 2.2.2. Section 2.3 explains how a phase shift of an X-ray wave can be used for imaging purposes. A short overview of various phase-sensitive imaging technques is presented in Subsection 2.3.2.

2.1 Interaction of X-rays with matter

Let us consider two waves of a linearly-polarized electromagnetic wave propagating in the z-direction with frequency ω, amplitude E_0, and a wave vector $k = 2\pi/\lambda$ (see Figure 2.1). For simplicity, only the electric field is considered in the following. One of them travels through vacuum, while the other traverses a block of material with refractive index n and length L. The first wave travels undisturbed. The second

wave traveling through matter interacts with it in various ways. The interaction is described by the *complex index of refraction* defined as

$$n = 1 - \delta + i\beta \ , \tag{2.1}$$

where δ is the *refractive index decrement* related to the phase shift, and β is the *absorption index* related to the absorption of X-rays by the linear attenuation coefficient μ.

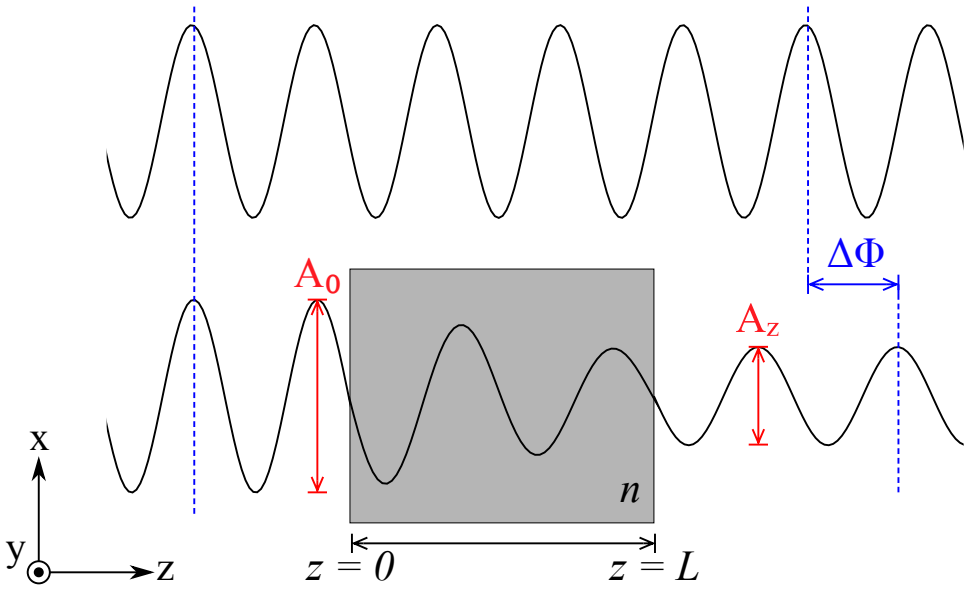

Figure 2.1: A plane monochromatic wave that traverses a material of complex refractive index n experiences an amplitude decrease $\Delta A = A_0 - A_z$ and a phase shift $\Delta\Phi$ compared to an unperturbed wave traveling in vacuum.

The second wave, after traversing the material can be described by

$$E(z,t) = E_0 \exp(inkz - \omega t) = E_0 \exp(-\beta kz) \exp(i\delta kz - \omega t) \ , \tag{2.2}$$

where the first exponential term describes the attenuation, and the second exponent describes a change of the phase. Both effect are schematically represented in Figure 2.1. The amplitude is decreased by a factor ΔA and the phase shifted by $\Delta\Phi$. These changes can be further related to material specific parameters β and δ.

2.1.1 Attenuation and phase shift

Attenuation The decrease of wave's amplitude ΔA is related to the drop of the beam's intensity

$$\frac{I(z)}{I_{z=0}} = \frac{|E(z)|^2}{|E_0|^2} = \exp(-2k\beta z) \ . \tag{2.3}$$

The above relation can be rewritten to calculate the intensity of the beam after traveling through a material of thickness z with refractive index n, which is known as the Lambert-Beer law:

$$I(z) = I_0 exp(-\mu z) \ , \tag{2.4}$$

where I_0 is the initial intensity before the material, and the quantity $\mu = 2k\beta$ is the *linear attenuation coefficient*. In a more general case of an object composed of materials with various linear attenuation coefficients, Equation 2.4 has to be extended to the line integral of μ along the beam path in z-direction:

$$\ln\left(\frac{I}{I_0}\right) = -\int_0^z \mu(z)dz. \tag{2.5}$$

Phase shift In the absence of absorption, the phase shift $\Delta\Phi$ of the X-ray wave after traveling through the material with a thickness of z and a refractive index decrement of δ is given by

$$\Delta\Phi(z) = k\delta z \ , \tag{2.6}$$

which is measured with respect to an undisturbed wave. A varying phase shift of the X-ray wave causes a refraction of the beam by an angle α, in the direction perpendicular to the propagation direction (in our case x). This angle is related to the first derivative of the phase shift $\partial\Phi/\partial x$ by

$$\alpha_x = \frac{\lambda}{2\pi}\frac{\partial\Phi}{\partial x} \ , \tag{2.7}$$

where λ is the wavelength of the beam propagating in z-direction [Paganin 2006].

Similar to attenuation, if the beam traverses an object composed of materials with various refractive index decrements, Equation 2.6 has to be extended to the line integral of δ along the beam path in z-direction:

$$\Delta\Phi = -\int_0^z k\delta(z)dz. \tag{2.8}$$

2.1.2 Complex atomic scattering factor

In the X-ray regime, δ and β can be also described in terms of the components of the complex atomic scattering factor $f^0(\omega) = f_1^0(\omega) - if_2^0(\omega)$ of the individual atoms in a material for forward scattering ($\theta = 0$) as [Attwood 2007]

$$\delta = \frac{n_a r_e \lambda^2}{2\pi} f_1^0(\omega) \ , \tag{2.9}$$

$$\beta = \frac{n_a r_e \lambda^2}{2\pi} f_2^0(\omega) \ , \tag{2.10}$$

where n_a is the atomic density, r_e is the classical electron radius, and λ is the

wavelength of the radiation. Values of the imaginary atomic scattering component $f_2^0(\omega)$ can be determined by measurements of the absorption through thin foils (or gases) made of elements of interest for a broad range of photon energies. The real part of the atomic scattering component $f_1^0(\omega)$ is then calculated through mathematical relations between f_1^0 and f_2^0, known as Kramers-Kronig relations. Therefore, by measuring β it is possible to determine $f_1^0(\omega)$, and thus the refractive index decrement δ. Both atomic scattering components were tabulated by [Henke *et al.* 1993].

By combining Equations 2.1, 2.2, and 2.3 we can see an explicit connection between scattering in forward direction and the refractive index:

$$n(\omega) = 1 - \frac{n_a r_e \lambda^2}{2\pi}\left[f_1^0(\omega) - i f_2^0(\omega)\right] . \tag{2.11}$$

We will see later that if the photon energy of the incident radiation lies considerably above the absorption edges of the material, the real part of the atomic scattering component $f_1^0(\omega)$ can be substituted by the atomic number Z. Consequently then $\delta \propto \rho_e$, where ρ_e is the electron density of the material.

2.2 Attenuation-contrast imaging

2.2.1 Image contrast formation

An X-ray beam traversing a material is attenuated as photons are continuously removed from it. The attenuation is a result of two competing processes: absorption and scattering. Absorption refers to photons being removed from the primary beam as a result of them being absorbed and transferring their energy to the material. Scattering refers to the photons being removed from the primary beam on account of them being redirected by (mainly Compton) scattering events. The energy is partially carried away from the site of the primary interaction [Barrett & Swindell 1996].

Additionally, photons can also be redirected by Raleigh scattering. However, for diagnostic-energy X-rays and low-atomic-number elements, the beams are separated by less than a milliradian and practically follow their original paths until they reach the detector. Therefore, Rayleigh scattering does not contribute to attenuation of the beam, but it is the basis of a phase-contrast image.

An attenuation-contrast image is created based on the difference in attenuation properties of materials inside the investigated object. A parameter describing these properties is the linear attenuation coefficient μ, which it is related to β as

$$\mu = 2k\beta = \frac{4\pi}{\lambda}\beta. \tag{2.12}$$

In the photon energy range of interest for biomedical CT scanning (10 - 150 keV), the linear attenuation coefficient is a result of photoelectric absorption, Compton scat-

tering and Raleigh scattering [McCullough 1975]. Therefore, it can be decomposed into contributions from each mode of X-ray photon interaction as

$$\mu = \mu_{pe} + \mu_{coh} + \mu_{incoh} \ , \tag{2.13}$$

where subscript *pe* denotes the photoelectric effect, *coh* denotes the coherent Raleigh scattering, and *incoh* denotes the incoherent Compton scattering. Furthermore, the linear attenuation coefficient μ is the product of the total electronic cross section σ^e_{tot} (cross section per electron) and the electron density of the material ρ_e

$$\mu = \rho_e \sigma^e_{\text{tot}} \ , \tag{2.14}$$

where $\rho_e = \rho N_0 Z/A$, which is described in detail in the following.

2.2.2 Total attenuation cross section

In the photon energy range relevant for imaging purposes, total attenuation cross section per electron σ^e_{tot} is given by the sum of contributions of three photon interaction mechanisms [McCullough 1975]:

$$\sigma^e_{\text{tot}} = \sigma^e_{\text{pe}} + \sigma^e_{\text{coh}} + \sigma^e_{\text{incoh}} \ , \tag{2.15}$$

where

σ^e_{pe} - photoelectric effect (pure absorption),

σ^e_{coh} - coherent (Rayleigh) scattering,

σ^e_{incoh} - incoherent (Compton) scattering.

The cross sections depend strongly on the X-ray photon energy (E) and the atomic number (Z) of the material. The dependence varies for each of the cross sections; therefore they contribute to the final contrast in the image with different strengths. For low-Z materials typically found in soft tissues, the dominant process at X-ray energies of up to 20-30 keV is the photoelectric effect. Since it is purely an absorption process, very often an image of soft tissues created at this energy range is called an *absorption image*. At energies above 30 keV the situation changes so that the Compton effect contributes most to the image formation.

Figure 2.2 shows the partial interaction coefficients for carbon (Z=6), germanium (Z=32), and lead (Z=82) in units of barn/atom (1 barn = 10^{-24} cm^2).

Both the electronic cross sections for photoelectric effect and the coherent scattering depend strongly on the photon energy E and on the material specific effective atomic number Z_{eff}

$$\sigma_{\text{pe}} \propto \frac{Z^k_{eff}}{E^l} \tag{2.16}$$

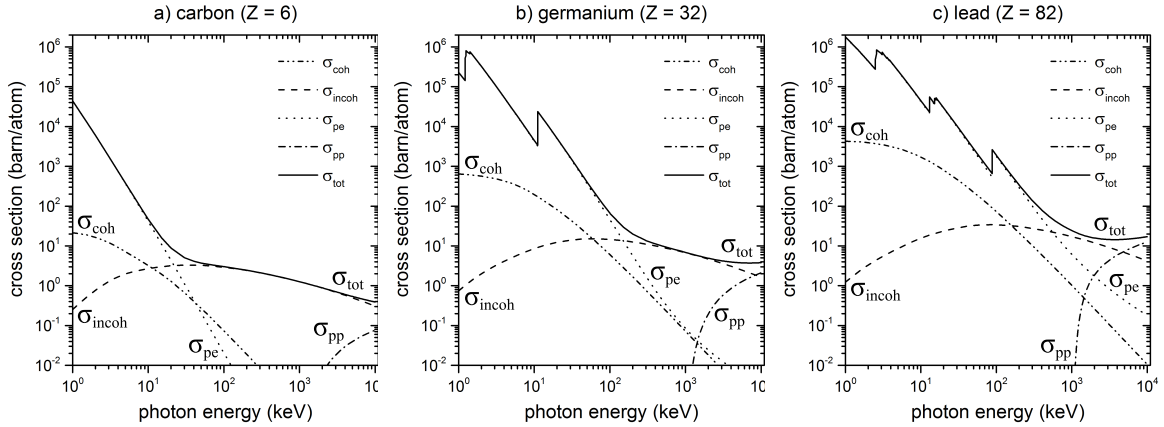

Figure 2.2: Total photon cross section σ_{tot} in carbon (Z=6), germanium (Z=32), and lead (Z=82), as a function of photon energy, showing the contributions of different processes: σ_{pe} - atomic photoelectric effect; σ_{coh} - coherent Rayleigh scattering; σ_{incoh} - incoherent Compton scattering; σ_{pp} - pair production in a nuclear field. Based on the data from XCOM database [Berger *et al.* 2010].

and

$$\sigma_{\text{coh}} \propto \frac{Z_{eff}^{m}}{E^{n}} \ , \tag{2.17}$$

where values for k and m are typically 3.8 and 2.0, respectively, and values for l and n are 3.2 and 1.9, respectively, but vary slightly depending on the photon energy and on the composition of the material [McCullough 1975].

On the other hand, the Compton scattering cross section σ_{incoh} can be determined from the Klein and Nishina function $f_{KN}(\alpha)$ [Barrett & Swindell 1996]

$$\sigma_{\text{incoh}} = \sigma_0 f_{KN}(\alpha) \ , \tag{2.18}$$

where α is the angle of scattering, and $\sigma_0 = 8\pi r_0^2/3$ is the cross section for (classical) Thomson scattering. If we assume that all electrons are free electrons and participate in Compton scattering equally (which is not strictly true, especially for heavy elements and low-energy X-rays below 1 keV), the Compton cross section depends only on the X-ray energy and is essentially independent of the atomic number Z [Hubbell 1969, McCullough 1975].

As seen in Figure 2.2, the influence of photoelectric absorption and coherent scattering on the linear attenuation coefficient μ decreases with increasing X-ray energy. It is the opposite for the Compton scattering. The "turning point" at which the Compton scattering contributes to the image contrast more than photoelectric effect increases with increasing Z of the material. For instance, for carbon the photoelectric absorption dominates up to around 20 keV, while for lead - up to around 600 keV. This fact has an interesting implication on complementarity between attenuation-based and phase-contrast imaging.

For soft tissues composed of low-Z materials and at X-ray energies of up to 20-30 keV, the attenuation process is dominated by the photoelectric effect so that the resulting image can be called an absorption image. Such image yields information on both density and material composition. And because phase contrast is proportional only to the electron density ρ_e, the two contrast channels are complementary, which was experimentally proven on many different types of soft tissue.

The situation changes for the same low-Z materials but at X-ray energies above 40 keV. The attenuation process starts being the result of mostly the Compton effect. Once it is purely caused by the Compton effect, the signal in attenuation contrast is proportional to the electron density ρ_e, as is also the case in the phase contrast. Thus, between various low-Z materials similar contrast differences are expected in attenuation and phase contrast images at high X-ray energies. An experimental validation of that theoretical fact is presented in Chapter 5.

In case of higher atomic number materials, such as germanium or lead (see Fig. 2.2), the X-ray energy at which the Compton scattering contributes to the image contrast more than the photoelectric effect is shifted to higher values. Therefore, at energies up to few hundreds of keV the attenuation contrast is again dominated by the photoelectric effect, which means that the attenuation and phase-contrast images provide complementary information and materials can be distinguished more easily. This fact was used to obtain multi-contrast micro-tomography reconstructions of a concrete sample presented in Chapter 8 as a proof-of-concept indicating the high potential of phase-contrast imaging for materials science applications.

2.3 Phase-sensitive imaging

2.3.1 Phase shift and refraction

Since a detector measures only the intensity of the X-ray beam as a square root of the wave's amplitude $|E(z)|^2$, any change in the phase of the wavefront is lost. However, the propagation direction of a wavefront phase shifted by a factor $\Delta\Phi$ is also slightly changed[1]. Such a wave is refracted by an angle α_x with respect to the propagation direction. The relation between the refraction angle and the phase change is given by equation 2.7.

The refraction angles are typically too small for the effect to be measured directly behind the sample. Only by moving the detector far away from the object and letting the refracted waves interfere with each other or by using additional optical elements, can those small refraction angles be detected. Various experimental methods to achieve that are described in Subsection 2.3.2.

We saw already (Eq. 2.8) that a phase-contrast image represents the projected local distribution of the refractive index decrement δ. It can be further related to the

[1] Only when $\Delta\Phi \neq$ const

X-ray energy and the density of the material by [Wilson 1950]:

$$\delta = \frac{r_0 h^2 c^2}{2\pi E^2} \sum_{i=1}^{n} N_i f_i^1, \tag{2.19}$$

where r_0 is the classical electron radius, h is the Planck's constant, c is the speed of light, E is the X-ray photon energy, N_i is the atomic density of an atom i given per-unit volume, and f_i^1 is the real part of the atomic scattering factor in the forward direction as in Eq. 2.9. If the X-ray photon energy of the incident beam is far away from the absorption edges of the elements of the investigated material, f_i^1 can be replaced by the element's atomic number Z_i, such that the sum $\sum_{i=1}^{n} N_i f_i^1$ reflects the electron density ρ_e of the material [Guinier 1994]. Therefore, the electron density ρ_e is related to the refractive index decrement δ and the energy of the X-ray photons by [James 1967]:

$$\rho_e = \frac{2\pi E^2}{r_0 h^2 c^2} \delta. \tag{2.20}$$

It is interesting to note that this equation was used in the following chapters to relate the grey values of phase-contrast images to quantitative properties of the investigated samples.

2.3.2 Phase-sensitive techniques

In biomedical and medical imaging contrast is often not high enough because absorption is small and differences in densities and composition are slight. Also, in materials science there are plenty of various composites made of materials with very similar densities, which makes them hard to distinguish with attenuation contrast only. Image contrast in such cases can be significantly improved by utilizing the phase change of the transmitted X-ray wave. At typical X-ray energies used in medical computed tomography, δ tends to be up to three orders of magnitude higher than β. Additionally, utilizing the phase shift for image contrast has the potential to create images with comparable contrast at higher X-ray energies than attenuation contrast, because it falls off slower with increasing energy: $\delta \propto 1/E^2$, whereas $\beta \propto 1/E^4$. As less radiation is absorbed at higher energies, it helps lower the radiation dose delivered to the patient. In order to take advantage of these properties, various phase-sensitive X-ray imaging methods have been developed [Fitzgerald 2000, Momose 2005]. They differ in many aspects: in the experimental setup used to detect the refraction of X-rays, the nature of the recorded signal, the resulting spatial resolution, and the requirements on the X-ray beam and the detector properties.

Crystal interferometry: An X-ray crystal interferometer consists of three beam-splitting crystals in Laue geometry, arranged in parallel as seen in Figure 2.3(a). The

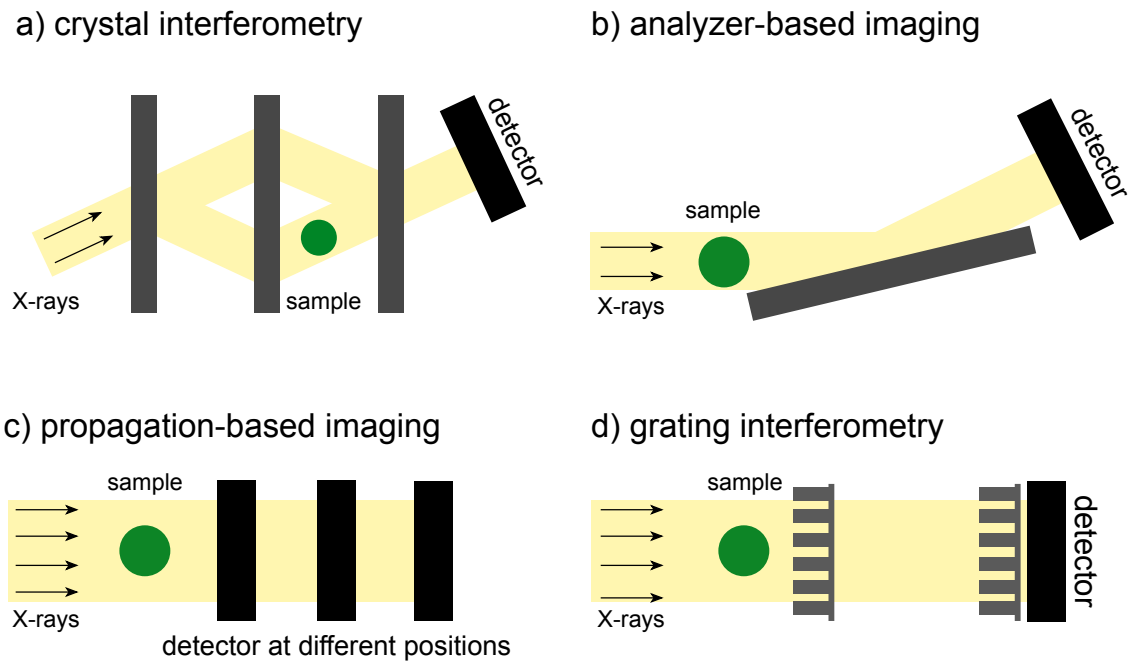

Figure 2.3: Schematic representation of various X-ray phase-sensitive imaging techniques.

collimated and monochromatic incident beam is split by the first crystal into diffracted and forward-diffracted beams. The second crystal redirects the split beams towards each other. One of them, the reference beam, remains undisturbed while the other passes through a sample. The two beams recombine at the third crystal where they produce an interference pattern, recorded by a detector placed directly behind the crystal. The form of that pattern depends on the optical path difference between the two beams. A phase shift of the wavefront caused by the sample is obtained by analyzing the fringe pattern by means of Fourier filtering or a fringe-scanning method.

Crystal interferometry is known to have the highest density resolution of all available phase-contrast techniques and the highest sensitivity to low spatial frequencies [Momose 2005], but is limited by mechanical stability issues. The path length difference between the two beams should stay constant and be on the order of the X-ray wavelength, which makes it sensitive to vibrations. To overcome this limitation, the first experimentally demonstrated crystal interferometer operated in hard X-ray regime [Bonse & Hart 1965] was monolithically cut off from a single silicon crystal. However, the Czochralski process which is used to create such crystals has certain technological limitations: only restricted in size, single crystals can be manufactured. This strongly limits the interferometer's field of view. Additionally, since the method relies on the Bragg diffraction condition, the X-ray beam has to be monochromatized and highly collimated. Therefore, synchrotron radiation has to be used or the technique is very impractical due to excessive measurement time.

Analyzer-based imaging: In this type of phase-sensitive technique, also known as diffraction-enhanced imaging, a crystal analyzer is placed in Bragg geometry in between the sample and the detector [Davis *et al.* 1995, Chapman *et al.* 1997] (see Figure 2.3(b)). The collimated and monochromatic incident beam first illuminates the sample, which deforms the wavefront and slightly changes its propagation direction. Downstream from the sample, the distorted beam hits the crystal, which acts as an angular filter. It reflects only the X-rays, which satisfy the Bragg diffraction condition within a very narrow angular range (typically up to tens of micro-radians). By slightly changing the tilt angle of the crystal, the intensity in each pixel varies and creates a so-called rocking curve. The image contrast is based on the angles at which X-rays are refracted by the sample and therefore it is proportional to the first derivative of the phase of the X-ray wavefront. This makes this technique less sensitive to low spatial frequencies than crystal interferometry, which measures the phase directly. Additionally, it is sensitive only in the diffraction direction, similarly to the grating-based imaging.

Qualitative images can be obtained from a measurement at a single point on the rocking curve. In that case, a clear separation between the absorption and refraction contributions is not possible. For quantitative information, a few images at different tilt angles of the analyzer crystal have to be recorded. By doing that, information not only on refraction angles but also on scattering can be extracted from a broadening of the rocking curve [Pagot *et al.* 2003].

Similarly to crystal interferometry, the X-ray beam has to be monochromatized and highly collimated. Hence, the analyzer-based imaging is practically performed only with high-flux synchrotron radiation. Measurements at conventional X-ray sources suffer from very long exposure times. The stability requirements of the crystals are less strict than these for crystal interferometry. Nonetheless, the field of view is limited by the size of the analyzer crystal and the fact that the X-ray beam has to be parallel.

Propagation-based imaging: In propagation-based imaging no additional optical elements are needed to detect the phase shift of the X-ray wavefront (see Figure 2.3(c)). Under spatially coherent illumination, a Fresnel diffraction pattern is generated when the detector is placed at a certain propagation distance after the sample. Interference of the diffracted beams results in intensity modulations at the object interfaces. As a result, edge-enhancement contrast can be observed and detected [Snigirev *et al.* 1995, Cloetens *et al.* 1996, Nugent *et al.* 1996].

Image contrast in the near field is proportional to the second derivative of the phase of the X-ray wavefront. In order to retrieve the phase and further the refractive index decrement δ, a solution of the transport of intensity equation (TIE) has to be found. In case of a homogenous object, this can be done easily by recording images at only one propagation distance [Paganin *et al.* 2002]. Objects made of multiple materials have to be measured at different sample-to-detector distances in so-called

holotomography [Cloetens *et al.* 1999].

An interesting feature of propagation-based imaging is the fact that, unlike analyzer-based and grating-based imaging techniques, it is sensitive to phase changes in all directions. The requirement for a high-resolution detector (pixel size of few µm) necessary to resolve the interference fringes can in some cases be a limiting factor of this technique. At moderate resolutions, large distances are required, which is impractical even at synchrotron radiation beam lines. The technique is also compatible with a micro-focus X-ray tube emitting a polychromatic spectrum [Wilkins *et al.* 1996]. The field of view is limited only by the projected beam size at the sample position and the size of the detector.

Grating interferometry: A typical X-ray grating interferometer consists of two micro-periodic gratings placed between the X-ray tube and the detector [David *et al.* 2002, Momose *et al.* 2003] (see Figure 2.3(d)). One of them is an absorption grating (analyzer) typically made of gold, while the other is a phase grating made of nickel, silicon or gold. The phase grating (G1) is used to split the incoming beam, which then interferes downstream and creates a periodic fringe pattern. An object put into the X-ray beam leads to a displacement of that pattern. Since the period of the interference fringes (of the order of a few micrometers) is too small to be directly resolved by the detector pixels, the absorption grating (G2) acts as an analyzer. It is placed in front of the detector and transforms local fringe position into signal intensity variation. One of the gratings is laterally moved in steps of a fraction of the fringe period (so-called phase-stepping) perpendicularly to the grating lines and several images are acquired. During this phase-stepping approach, a quasi-sinusoidal intensity-oscillation curve is recorded. For each pixel independently, the change in lateral position of the interference pattern is determined by Fourier analysis of the intensity oscillation curve, and the differential phase image is extracted [Weitkamp *et al.* 2005, Pfeiffer *et al.* 2007b].

The image contrast is proportional to the first derivative of the phase front, which results in low sensitivity to low spatial frequencies, similar to analyzer-based imaging. Yet another similarity between these two techniques is their sensitivity only in the diffraction direction (in case of grating interferometry: perpendicular to the grating lines). In a parallel-beam configuration, the field of view is limited by the beam size and the size of the gratings. In a cone-beam setup, the size of the analyzer grating is the limiting factor. A more detailed explanation of this issue can be found in Subsection 5.2.1.

Interestingly, requirements for the spatial coherence of the X-ray beam are not as stringent as in the other phase-sensitive techniques. Therefore, after an addition of a source grating (G0), grating interferometry can be used with conventional laboratory X-ray tubes. This additional grating splits a conventional extended X-ray source into an array of smaller sources with enough spatial coherence for the interference effects to occur [Pfeiffer *et al.* 2006].

Similarly to analyzer-based imaging, an image related to the small-angle scattering

power of the sample [Wang *et al.* 2009, Bech *et al.* 2010] at structures typically below the spatial resolution of the imaging system is accessible.

Since grating interferometry and its implementation at high X-ray energies is the subject of this thesis, a more in-depth description can be found in Chapter 3.

Chapter 3
X-ray grating interferometry

Contents

3.1 Principles 20
3.1.1 Talbot (self-imaging) effect 20
3.2 Components of a Talbot-Lau interferometer 22
3.2.1 The phase grating 22
3.2.2 The analyzer grating 23
3.2.3 The source grating 23
3.3 Data collection and analysis 24
3.3.1 Phase stepping 24
3.3.2 Fourier processing 26
3.3.3 Three contrast channels 26
3.4 Operation at high X-ray energy 29
3.4.1 Influence on fringe visibility 30
3.5 High-energy experimental implementation 32

This chapter presents the theory and fundamentals of X-ray grating interferometry.

Section 3.1 describes the basic principles, including the self-imaging phenomenon called the Talbot effect. The functions of the three gratings forming the interferometer are presented in Section 3.2. The phase-stepping procedure commonly used to collect the data is described in Subsection 3.3.1, while the signal extraction and analysis is explained in Subsection 3.3.2. The three contrast channels, related to the attenuating, phase shifting and scattering properties of an object, obtained from the Fourier analysis of the stepping curves, are presented in Subsection 3.3.3. Section 3.4 discusses operation of an interferometer at X-ray energies above 40 keV and the limitations that come with it. An important parameter, which determines the optical performance of an interferometer, fringe visibility, is detailed in Subsection 3.4.1. The experimental implementation of a Talbot-Lau interferometer at a design energy of 45 keV is presented in section 3.5.

3.1 Principles

X-rays passing through an object are not only absorbed but also refracted. This additional physical process can be utilized to produce additional image-contrast modalities. Unfortunately, the micro-radian deviations of X-rays caused by refraction in the sample are typically too small to be measured directly by modern state-of-the-art detectors. A different approach is therefore needed. Various refraction-sensitive techniques exist [Fitzgerald 2000]. They differ in many aspects: the experimental setup used to detect the refraction of X-rays, the nature of the recorded signal, the spatial resolution, and the requirements on the X-ray beam and the detector properties. This thesis focuses on one of these techniques, i.e., *Talbot-Lau grating interferometry* [David *et al.* 2002, Momose *et al.* 2003, Weitkamp *et al.* 2005], which does not require a highly spatially coherent, parallel, and monochromatic beam, and thus can be used with conventional, polychromatic X-ray sources [Pfeiffer *et al.* 2007c]. It measures the displacement of the interference pattern caused by the sample in reference to an undisturbed system, i.e. without a specimen. Such an experimental setup consists of three micro-periodic gratings placed between the X-ray tube and the detector, which create and analyze the interference pattern. Grating interferometry provides different optical properties of the object of interest. From a single measurement, three different images can be obtained: the first is proportional to the linear attenuation coefficient μ (attenuation-contrast image); the second to the refractive index decrement δ (phase-contrast image); and the third to the linear scattering coefficient ϵ (dark-field image), which is related to the small-angle scattering power of the sample [Wang *et al.* 2009, Bech *et al.* 2010] at structures typically below the spatial resolution of the imaging setup. The technique was developed at synchrotron facilities and later successfully transitioned to laboratory X-ray tubes [Pfeiffer *et al.* 2006].

3.1.1 Talbot (self-imaging) effect

The working principle of grating interferometry is based on a self-imaging phenomenon called the Talbot effect. It was observed for the first time by Talbot in 1836 with visible light and analytically explained later by Lord Rayleigh in 1881. It describes the self-imaging phenomenon of periodic structures under coherent illumination. Talbot observed that an absorbing periodic object, illuminated by spatially coherent radiation, produces a "self image" at certain propagation distances along the optical axis. It is a consequence of the Fresnel diffraction and leads to the repetition of a periodic wavefront after a certain distance, referred to as *Talbot distance* d_T, which depends on the periodicity of the object p and the wavelength λ:

$$d_T = m\frac{2p^2}{\lambda} \ , \text{ where } m = 1, 2, 3, ... \tag{3.1}$$

Instead of an absorbing periodic object, a phase grating can be used. We will see in

the following that this is preferable for imaging applications because of a difference in transmission of X-rays through such gratings. A phase shift induced by a phase grating creates periodic intensity modulations at particular distances, resembling the self-imaging effect of absorbing objects. The distances, however, are fractions of the Talbot distances d_T calculated for absorbing gratings, and are thus called *fractional Talbot distances*. Depending on the phase shift determined by the height of the phase grating bars and the wavelength of the illumination, different fractional Talbot distances are observed. Figure 3.1 presents X-ray intensities behind a binary absorption grating and binary phase gratings inducing phase shifts of $\pi/2$ and π.

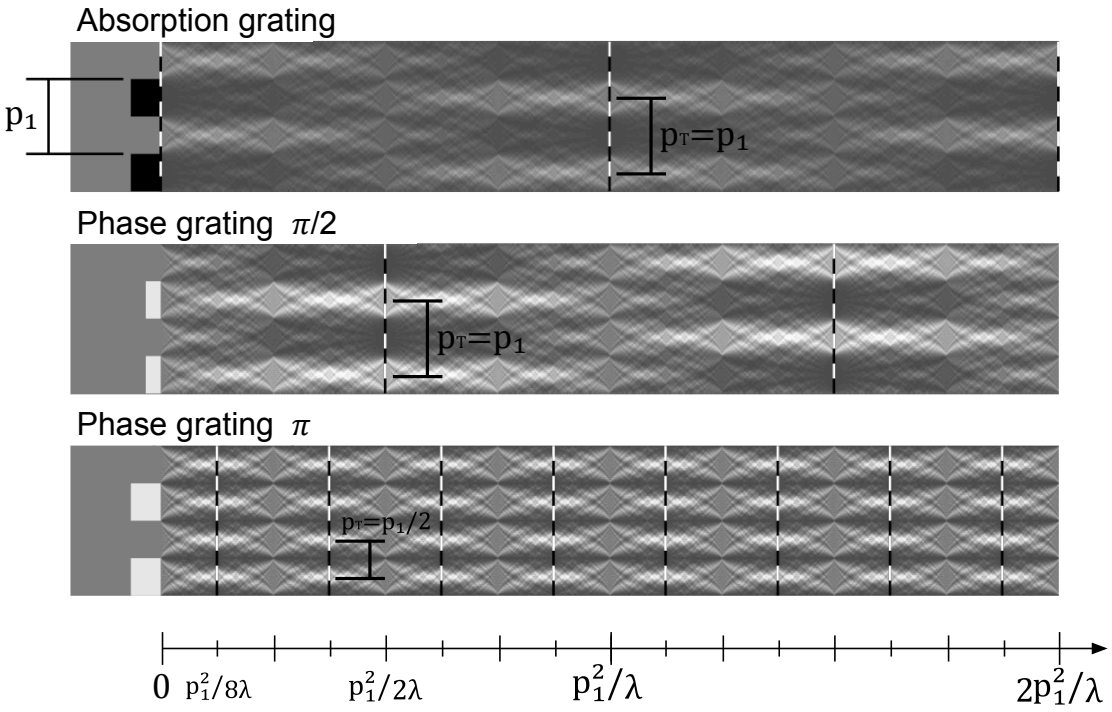

Figure 3.1: X-ray intensity patterns behind different types of binary gratings with a period of p_1 and a duty cycle of 0.5 illuminated by a coherent monochromatic plane wave. Each of the gratings has different optical properties. The absorption grating has purely absorbing lines, while the phase gratings have negligible absorption but shift the phase of the X-rays by $\pi/2$ or π. The maxima of the intensity modulations are indicated by the dashed lines. Figure adapted from [Weitkamp *et al.* 2006].

The self-imaging effect can be also observed in case of incoherent illumination. It was first described by [Lau 1948] with visible light. By placing an additional grating directly after the source, an array of individually coherent, but mutually incoherent line sources is created. Interference patterns produced by two adjacent line sources illuminating the periodic structure overlap, increasing the total intensity in the self-image plane. This effect serves as a basis for enabling the technique to be used at large-sized incoherent radiation sources [Pfeiffer *et al.* 2007c].

3.2 Components of a Talbot-Lau interferometer

A Talbot-Lau interferometer consists of three micro-periodic gratings placed between the X-ray tube and the detector. The purpose of each of the gratings is described in the following.

3.2.1 The phase grating

The first of the three gratings, denoted by G1 with a period p_1, is used to split the incoming beam into the $\pm 1^{st}$ diffraction orders, which then interfere downstream and create a periodic rectangular-shaped interference pattern. In the presence of a refractive object, the pattern is laterally shifted. Analysis of that distortion yields information about the object's optical properties.

The beam-splitter grating can be either a phase-shifting or an absorbing structure, since both lead to interference fringe patterns through the Talbot self-imaging effect. Phase gratings are used preferably because of their much higher photon efficiency compared to absorption gratings. When using phase gratings, their material and thickness are chosen so as to introduce a phase shift equal to $\pi/2$ or π, because only then is the highest contrast interference pattern created.

The position of the fractional Talbot distances along the optical axis depends on the phase shift ϕ induced by the grating lines. Maximum intensity modulations can be found at fractional Talbot distances d_T:

$$d_T = \frac{1}{\eta^2}\frac{np_1^2}{2\lambda} \quad (n = 0, 1, 2, ...) \ , \tag{3.2}$$

where λ is the X-ray wavelength, and p_1 is the period of G1. Phase gratings produce fringes with maximum contrast at odd Talbot orders ($n = 1, 3, 5, ...$), while absorption gratings produce maximum intensity modulations at even Talbot orders ($n = 0, 2, 4, ...$). The resulting fringe period depends on the phase-shifting properties of the beam splitter G1 (phase shift ϕ), and equals p_1/η, where:

$$\eta = \begin{cases} 1, & \text{for } \phi = \pi/2 \text{ or an absorption grating} \\ 2, & \text{for } \phi = \pi. \end{cases} \tag{3.3}$$

When the beam splitter G1 is illuminated by a spherical wave from a source situated at a distance l, the fractional Talbot distances become:

$$D_T = d_T \frac{l}{l - d_T} \ . \tag{3.4}$$

where d_T denotes the Talbot distances for a plane wave. At the distances D_T the period of the interference pattern is magnified by a factor $M = (l + D_T)/l$.

3.2.2 The analyzer grating

The second of the three gratings, denoted by G2 with a period p_2, is a purely absorbing grating that matches the period of the observed interference pattern:

$$p_2 = p_1/\eta \ . \tag{3.5}$$

The period of the interference pattern fringes is too small to be directly resolved by the modern state-of-the-art detectors with reasonable field of view and pixel size. The analyzer grating G2 transforms local fringe position into signal intensity variations. The grating is placed directly in front of the detector at a fractional Talbot distance from G1. Its lines are made of opaque material, usually gold, with thickness depending on the X-ray energy. Thanks to the analyzer grating the detector's pixels may be of a size much larger than the period of the fringes, which allows them to collect the amount of photons sufficient for imaging purposes with reasonable acquisition times.

The analysis of the interference pattern and its changes caused by the sample can be performed with a so-called phase-stepping technique or by direct processing of the moiré pattern generated by the grating pair. The phase-stepping method allows for the best separation of the phase signal from the absorption information. The moiré technique has the advantage of simpler and faster measurements, but at the cost of reducing the spatial resolution significantly.

Throughout this thesis, only the phase-stepping mode was used. The next section describes this technique and the separation of three signals. A detailed description of imaging with moiré pattern can be found in [Momose *et al.* 2006].

3.2.3 The source grating

For interference effects to occur and to create fringes of sufficient contrast, special requirements on transverse coherence of the wavefront have to be fulfilled. This requirement has to be met only in the direction perpendicular to the grating lines.

The transverse, or spatial, coherence is related to the source size and is defined as:

$$\xi_c = \frac{\lambda l}{s} \ , \tag{3.6}$$

where λ is the wavelength of the radiation, l is the distance between the source and the beam splitter G1, and s is the width of the source spot.

The source grating, denoted by G0 with a period p_0, is placed close to the X-ray source and creates an array of individually coherent but mutually incoherent sources. The grating acts as a set of slit apertures creating virtual sources of smaller size. Each of these sources creates a fringe pattern with good contrast in the analyzer plane because of sufficient spatial coherence. The patterns add up constructively if the spacing of the slits is chosen so that the fringe patterns of adjacent slits are displaced by one or integer multiples of the fringe period. This is achieved with a

period of the source grating p_0 of:

$$p_0 = p_2 \frac{L}{d} \,, \tag{3.7}$$

where L is the distance between G0 and G1, p_2 is the period of G2, and d is the distance between G1 and G2.

It is important to note that the spatial resolution of the images is independent of the spatial coherence and is determined only by the projected source size $w = s \cdot d/L$ like in the case of a non-interferometric imaging system. In that sense, the arrayed source decouples spatial resolution from spatial coherence.

Analytically, the influence of an extended source can be described by a convolution of the interference pattern profile with the source profile at the plane of the analyzer grating. It was shown in [Weitkamp *et al.* 2006, Bech 2008] that the visibility decreases exponentially with increasing source size, and it reaches almost zero for projected source sizes, which are bigger than half the period of the interference pattern:

$$s \leq \frac{p_2 L}{2d} \,. \tag{3.8}$$

The requirements on monochromaticity, on the other hand, are quite relaxed so that the grating interferometer can be operated with broad polychromatic spectrum. Good fringe contrast is obtained when

$$\frac{\lambda_0}{\Delta\lambda} \gtrsim n \,, \tag{3.9}$$

where λ_0 is the design wavelength of the instrument, $\Delta\lambda$ is the width of the wavelength distribution around λ_0, and n is the Talbot order.

The three-grating system is known as a Talbot-Lau interferometer and can be used with standard X-ray tubes with source sizes of up to a few millimeters and wide polychromatic spectra, which was demonstrated for the first time by [Pfeiffer *et al.* 2006].

3.3 Data collection and analysis

3.3.1 Phase stepping

In grating interferometry, the phase-stepping method is used to sample the interference pattern at its different relative positions and to further retrieve three separate image contrasts related to different optical properties of a sample. When a phase-stepping method is performed, one of the gratings is laterally moved in steps of a fraction of the period (the so-called phase stepping) perpendicularly to the grating lines and the beam direction. The movement is done over at least one period of the interference pattern in no less than three steps per period. At each grating position an image is acquired. The relative movement of the interference pattern to the analyzer grating

lines allows sampling the shape of the interference pattern. To avoid moiré fringes, the period of the analyzer grating matches the period of the interference pattern. This phase-stepping procedure results in a periodic intensity modulation $I(x, y)$ recorded at the detector plane in each pixel separately, which can be seen in Figure 3.2.

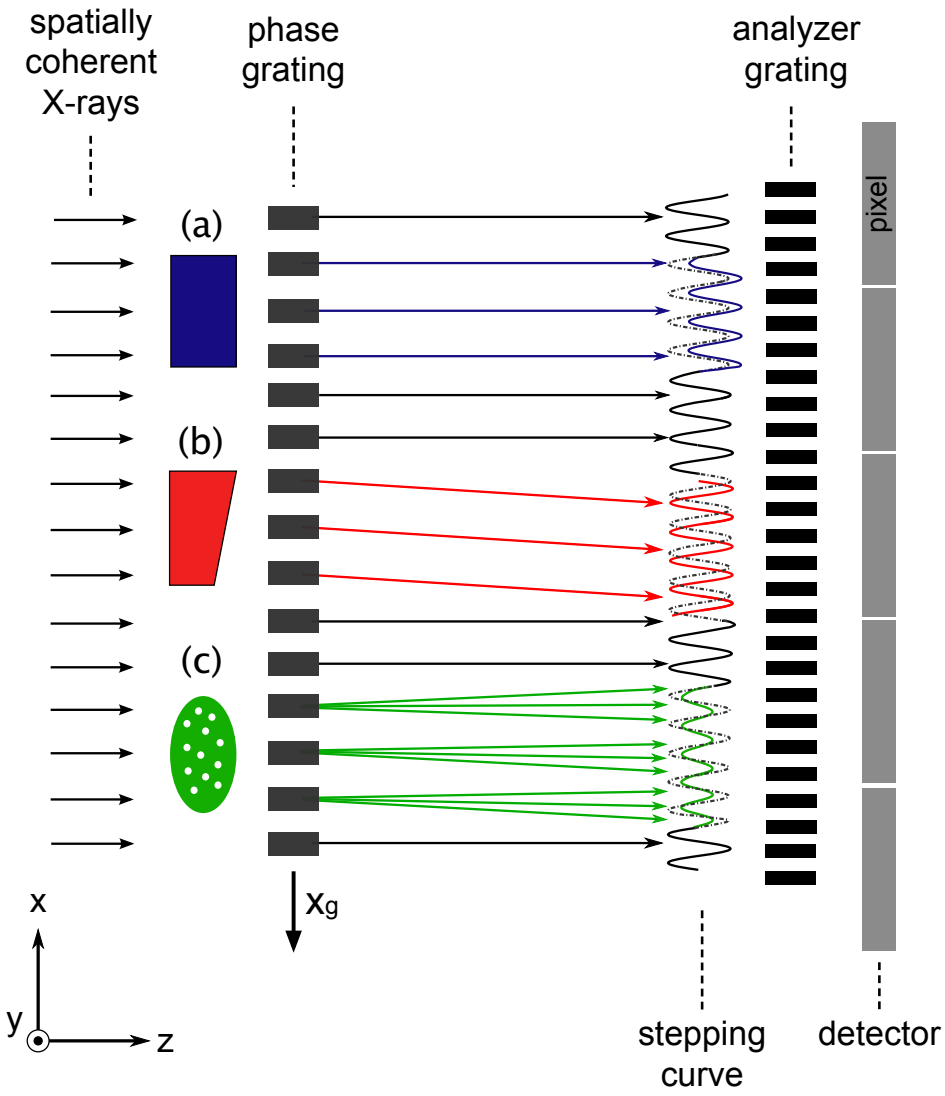

Figure 3.2: Working principle of X-ray grating interferometry with a spatially coherent source.

The shape of the stepping curve is determined by the convolution of the interference pattern with the local transmission function of the analyzer grating. In the ideal case of a fully coherent irradiation, the intensity pattern can be described by a top-hat transmission function. Its convolution with a top-hat transmission function of an ideal analyzer grating yields a triangular function. However, in the usual case of moderate spatial coherence (extended source size) the addition of a projected Gaussian-shaped source results in a nearly sinusoidal intensity oscillation.

3.3.2 Fourier processing

Extraction of three image contrast channels is performed by analyzing the displacement of the interference pattern caused by the sample in reference to an undisturbed system, i.e. one without a specimen. For that, phase-stepping curves with and without the sample are recorded and the difference between them is analyzed (see Fig. 3.3).

For each detector pixel, the recorded intensity oscillation resulting from the phase-stepping scan has an approximately sinusoidal shape. Therefore, it can be described by a Fourier series:

$$I(x_g, x, y) = a_0(x, y) + \sum_{m=1}^{\infty} a_m(x, y) \cos(m\frac{2\pi}{p_2}x_g + \varphi_m(x, y)) \ , \tag{3.10}$$

where a_m are the amplitude coefficients, φ_m are the corresponding phase coefficients, p_2 is the period of the analyzer grating G2, x_g is the relative grating position during the phase-stepping scan, and (x, y) denotes a specific point on the analyzer plane, or a detector pixel.

Higher order terms can be neglected in case of moderate coherence (extended source size). The first order term ($m = 1$) is sufficient to describe the intensity oscillation as:

$$I(x_g, x, y) = a_0(x, y) + a_1(x, y) \cos(\frac{2\pi}{p_2}x_g + \varphi_1(x, y)) \ , \tag{3.11}$$

with the average value (offset) a_0, phase φ_1, and the oscillation amplitude a_1. The parameters a_0, φ_1, and a_1, or more specifically their relative change, relate to the optical properties of an object placed into the beam path.

In order to extract these parameters for each pixel, Fourier analysis (with the implementation of Fast Fourier Transform (FFT)) is commonly used for simplicity and speed. The absorption parameter a_0 is extracted from the DC (zero-frequency) term, while the differential phase and the dark-field parameters φ_1 and a_1 are extracted from the phase and magnitude of the first harmonic peak. However, FFT can be used only when the stepping curve, created by the movement of one of the gratings, is sampled with equidistantly spaced points and covers the exact multiple of a full period.

In cases of quasi-randomized phase stepping, other algorithms such as least-squares fitting, principal components analysis or generalized phase shifting algorithms can be utilized. Their detailed explanation and comparison can be found in [Baur 2013].

3.3.3 Three contrast channels

Attenuation, differential phase and scattering signals can be obtained from the three Fourier components extracted from the phase-stepping curves. In a realistic experimental implementation of grating interferometry, a reference phase-stepping scan is

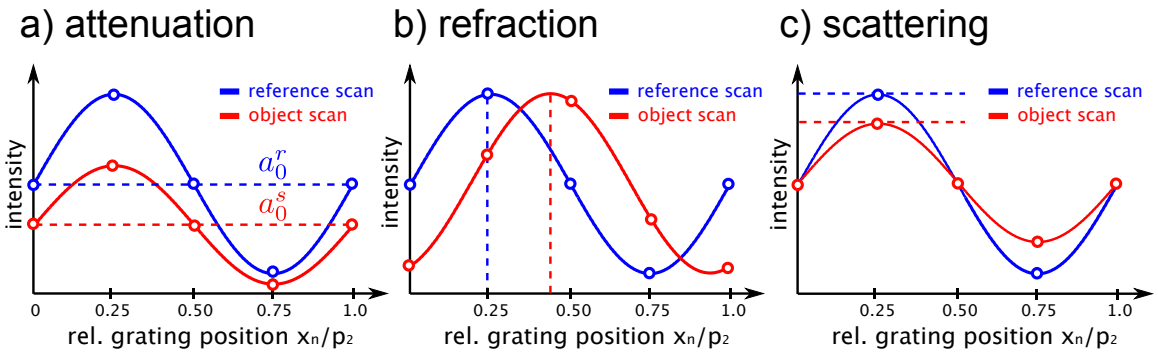

Figure 3.3: Intensity oscillation recorded at each detector pixel size. Each point on the stepping curve corresponds to an intensity recorded.

needed to correct for inhomogeneities of the beam profile. In the following, components of the intensity oscillation of the reference scan without the sample in the beam path are indicated by the superscript 'r'. The components obtained from a scan with the sample are marked with the superscript 's'.

Attenuation image: Attenuation in the sample is given by:

$$A = 1 - \frac{a_0^s}{a_0^r} \,, \tag{3.12}$$

but what is actually often displayed as the so-called "attenuation image" is the transmission:

$$T = 1 - A = \frac{a_0^s}{a_0^r} \,, \tag{3.13}$$

By taking the negative logarithm of the projection, T is related to the attenuation coefficient β through the line integral in Eq. 2.5, known as the Lambert-Beer law.The attenuation image recorded with a grating interferometer is very similar to the image that would have been obtained for otherwise identical conditions, but without the interferometer in the beam.

Phase image: The transverse shift of the intensity oscillation curve is given by:

$$\Delta\varphi_x = \varphi_1^s - \varphi_1^r \,, \tag{3.14}$$

and is related to the phase shift of the X-ray wave front $\Phi(x, y)$. The phase shift caused by the sample causes a refraction of the beam by an angle α, in the direction perpendicular to the grating lines. This angle is connected with the differential phase shift $\partial\Phi/\partial x$ by

$$\alpha_x = \frac{\lambda}{2\pi}\frac{\partial\Phi}{\partial x} \,, \tag{3.15}$$

where λ is the wavelength of the beam propagating in z-direction [Weitkamp *et al.* 2005].

Furthermore, the refraction angle α is proportional to the measured phase shift $\Delta\varphi_x$ of the intensity oscillation, the period p_2 of the analyzer grating, and the distance d between the gratings G1 and G2,

$$\alpha_x = \Delta\varphi_x \frac{p_2}{2\pi d} \,. \tag{3.16}$$

By combining equations 3.15 and 3.16, we see that the measured phase shift of the stepping curve is proportional to the first derivative of the phase shift of the X-ray wave front $\Phi(x, y)$

$$\Delta\varphi_x = \frac{\lambda d}{p_2} \frac{\partial \Phi}{\partial x} \,. \tag{3.17}$$

An image formed by the measured phase shift $\Delta\varphi_x$ of the stepping curve is called the *differential phase-contrast image*.

Dark-field image: The dark-field (scattering) signal is defined as a change in the amplitude of the intensity oscillation, called for simplicity the visibility of the stepping curve. It is calculated as a ratio of the oscillation amplitude a_1^s to the average value of the stepping curve a_0^s in the presence of the sample, and normalized by the visibility of a reference scan:

$$D_x = \frac{V^s}{V^r} = \frac{a_0^r}{a_0^s} \frac{a_1^s}{a_1^r} \,, \tag{3.18}$$

where V is the aforementioned visibility or contrast of the interference fringes defined as in Eq. 3.21.

The dark-field signal describes a reduction in the visibility of the interference fringes caused by a decoherence of the beam from small-angle scattering in the sample. The scattering usually takes place on structures which size is below the spatial resolution of the detector.

The scattering signal can be expressed in terms of the material-dependent linear diffusion coefficient ϵ which exhibits an exponential dependence on the thickness of the traversed material [Bech 2008]:

$$D_x = exp\Big(- \frac{2\pi^2 d^2}{p_2^2} \int \epsilon(z) dz \Big) \,, \tag{3.19}$$

similar to that of the attenuation signal, under the assumption that the scattering of the X-rays is isotropic.

Projections of a test sample in each of the contrasts explained above are shown in Figure 3.4.

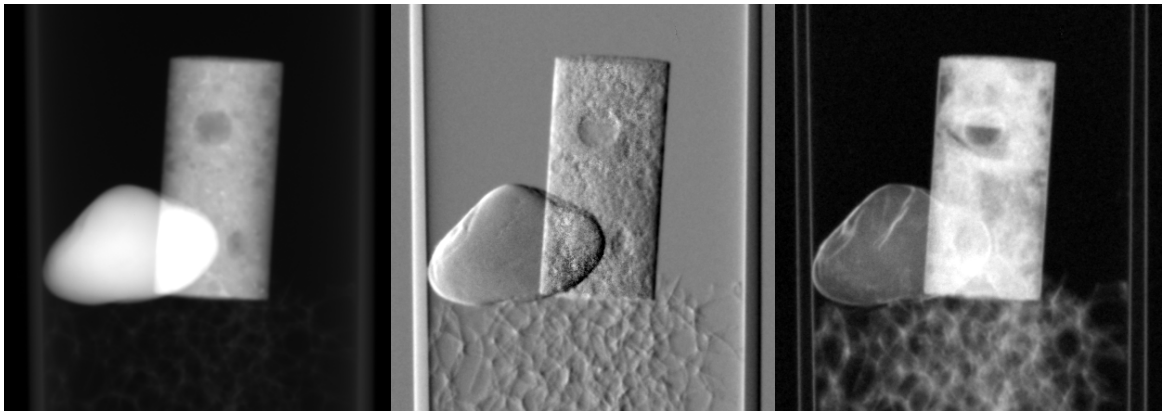

Figure 3.4: Attenuation, differential phase, and dark-field projections of a test sample consisting of a rock, a concrete cylinder block and a piece of foam. Complementary information is provided by the three images.

3.4 Operation at high X-ray energy

Operation of an X-ray grating interferometer at X-ray energies above 40, 50 keV is limited by the absorption grating fabrication processes; the gold grating bars cannot be easily made high enough to be opaque to X-rays, especially for small period gratings. This causes radiation to "leak" through the gratings and drastically reduces the fringe visibility of the interferometer. It is not only the height but also the quality of the structures which influence the visibility. Because of these limitations, performance of X-ray grating interferometry is not at its theoretical maximum at X-ray energies above 50 keV.

The ratio of the grating bars height h_g to the bars width $p_g/2$ is called the aspect ratio and is defined as:

$$R_g = \frac{2h_g}{p_g} \,, \tag{3.20}$$

with g being 0, 1 or 2 depending on the grating type.

It turns out that the production of absorption gratings with high aspect ratios (>100) poses a lot of technical challenges. In order to increase the mechanical stability of the resist after development, the commonly used layout incorporates the so-called bridges (as seen in Figure 3.5). They are frequent connections between the resist bars used to prevent the resist structures from collapsing. However, these connections result in interruptions of the gold grating bars, which in turn decreases the visibility and limits the performance of the interferometer.

New techniques are under development to discard the bridges, which would in turn improve the gratings absorption properties. The bridges can be substituted by thin (2 µm in diameter) reinforcement pillars penetrating the substrate lines under a certain angle ranging from 30°to 45° [Kenntner 2012]. This so-called "sun-ray" design

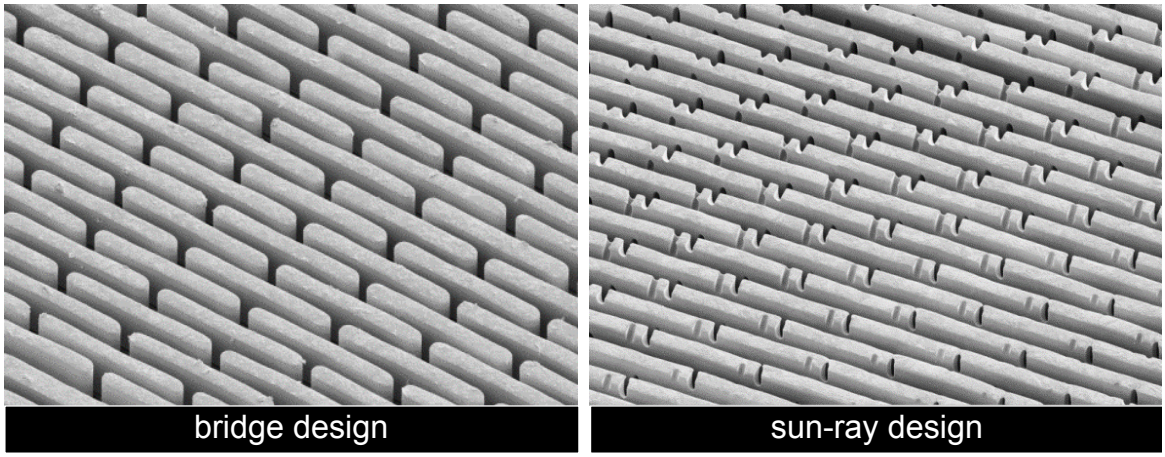

Figure 3.5: Scanning electron microscope images of an absorption grating G2 using a so-called "bridge" and "sun-ray" design. The supporting resist is removed, thus only the gold structures are visible. Image courtesy of Pascal Meyer (KIT).

shows a significant increase of the achievable visibility, but it is commonly used only for gratings with aspect ratios of up to 80.

3.4.1 Influence on fringe visibility

Insufficient absorption of the X-rays by the absorption grating bars causes unwanted decrease of the fringe visibility.

The visibility of the interference fringes characterizes the amplitude or contrast of the intensity modulation in the interference pattern, and is defined as:

$$V = \frac{I_{max} - I_{min}}{I_{max} + I_{min}} \cdot 100\%, \tag{3.21}$$

where I_{max} and I_{min} are, respectively, the maximum and minimum values of the intensity pattern produced by the phase grating in each detector pixel. It is the most important figure of merit for the efficiency of the interferometer [Weitkamp *et al.* 2006]. It describes the quality of the interference; the bigger its value is, the better the fitting of the stepping curve works in the presence of noise. It is a setup- and spectrum-dependent parameter, which determines the quality of the differential phase-contrast image as its signal-to-noise ratio depends on

$$SNR_{\Delta\varphi_x} \propto S \cdot V \cdot \frac{1}{\sqrt{a_0}}\,, \tag{3.22}$$

where S is the sensitivity, V is the visibility, and a_0 is the number of photons (flux).

The value of visibility is usually given as a mean calculated over many detector pixels covering the whole field of view. From its theoretical maximum it is reduced

by the extended projected Gaussian shaped source size, and consequently by the reduced transverse coherence length ξ_c. The reduced visibility can be calculated by [Weitkamp *et al.* 2006, Bech 2008]:

$$V = \exp\left(-0.94 n p_2 / \xi_c\right) \tag{3.23}$$

which is valid for extended sources whose size of w fulfill the relation $w/p > 1/2\pi$.

The visibility of a grating interferometer with design energy of 45 keV and above is additionally decreased by the insufficient absorption grating height and the overall quality of such gratings. Simulations and energy-resolved measurements of visibility (see Figure 3.6) show that the maximum performance is reached approximately at the design energy of the interferometer and decreases on both sides. By comparing simulated visibility spectra for a grating with and without imperfections, one can see that the actual quality of the G2 grating used in the experimental setup is quite poor. This, however, opens possibilities for higher fringe visibility when the quality of the gratings improves in the near future.

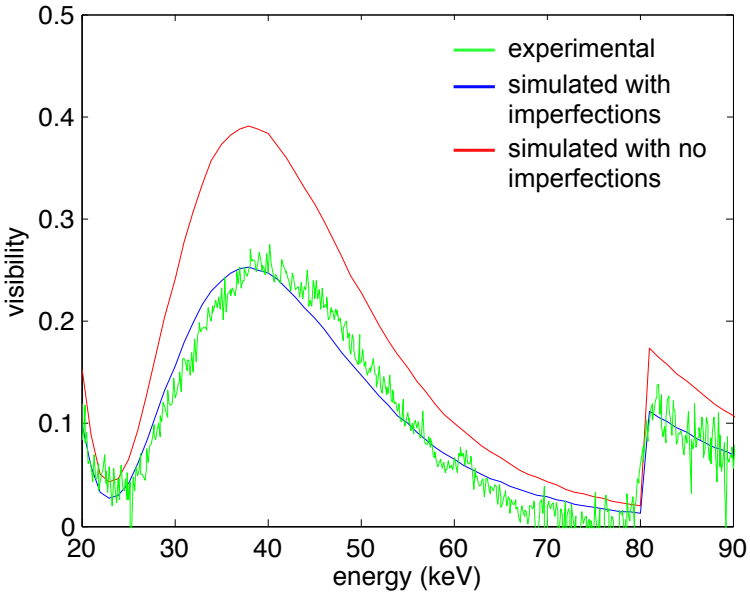

Figure 3.6: Comparison of simulated visibility spectra with an energy-resolved visibility measurement of the high-energy experimental setup presented in Section 3.5. The increase in visibility above 80 keV is the result of a gold absorption edge at 82 keV which strongly decreases the transmission of X-rays through the grating lines.

The optimum spectrum for such an experimental system would be X-ray photons with energies approximately between 30 and 50 keV. The low energy part of the spectrum can be easily filtered out with an aluminum filter, which results in the

increase of the overall visibility. The high-energy tail of the spectrum can only be dealt with by increasing absorption of the grating lines, either by increasing their height or by changing to a material with an absorption coefficient higher than gold. The former, achieved by tilting the gratings along the beam axis, is discussed in detail in Chapter 7.

3.5 High-energy experimental implementation

The experimental results with a polychromatic source presented in this thesis (except for Chapter 7) were obtained with a high-energy X-ray grating interferometer installed at the Technical University of Munich, Germany. It is a symmetric Talbot-Lau grating interferometer employing three gratings. It was operated at the 1st fractional Talbot order with distances between the consecutive gratings of approximately 91 cm. By having equal distances between the gratings, the highest angular sensitivity for a given system length was achieved [Donath *et al.* 2009a].

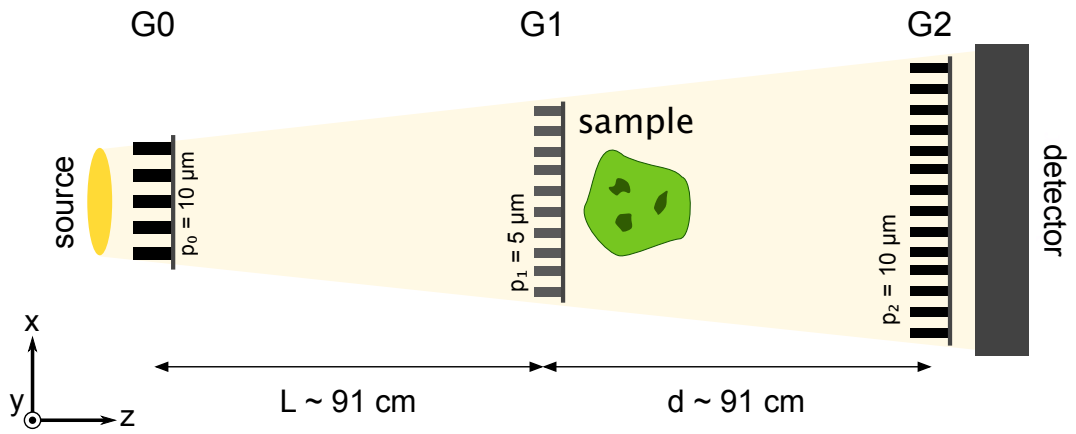

Figure 3.7: Schematic representation of the high-energy Talbo-Lau interferometer at its design energy of 45 keV. The sample can be placed either before or after the phase grating G1 depending on the required magnification.

Gratings: All the gratings were produced by microworks GmbH (Karlsruhe, Germany) using X-ray lithography and electroplating [Reznikova *et al.* 2008]. The gratings' parameters can be found in Table 3.1. For the experiments, the phase grating with bars of 8 µm in height was used, which resulted in a $\pi/2$-phase shift at the X-ray wavelength of 45.5 keV. The system's overall length (distance between the source and the detector) was slightly over 2 meters.

X-ray source: As an X-ray source, a COMET MXR-160HP/11 tube with a tungsten anode was used. The tube can be operated with two focal spots varying in size.

Table 3.1: Parameters of the gratings available at the high-energy grating interferometer at TUM. Gratings with highly-absorbing gold structures were use to deliver satisfactory fringe visibility.

			Nominal		
Type	Material	Energy (keV)	Period (µm)	Height (µm)	Diameter (mm)
G1 ($\pi/2$)	Ni	34.5	5	6	70
G1 ($\pi/2$)	Ni	45.5	5	8	70
G1 ($\pi/2$)	Ni	57.0	5	10	70
G0	Au	-	10	150	70
G2	Au	-	10	150	70
G2	Au	-	10	150	100

The small focal spot has a size of 0.4 mm and can deliver maximum power of 800 W. The big spot has a size of 1 mm with 1800 W of maximum power. The output of the tube is covered with an 0.8 mm beryllium window. The mean fringe visibility calculated over the whole field of view was independent of the focal spot size. Image blurring and degradation of the Modulation Transfer Function (MTF) was observed for the big focal spot due to the increased projected spot size.

X-ray detector: An amorphous silicon Varian PaxScan 2520D receptor with a 600 μm-thick structured cesium iodide doped with thallium - CsI(Tl) scintillation layer and 127 μm physical pixel size was used as a detector. It was chosen because of its high absorption efficiency of the thick scintillation material at energies above 35 keV and a relatively good DQE(0) of 70% ±5% at RQA5 spectra [Ranger *et al.* 2007].

Part II

Experimental results

Chapter 4

Quantitative measurements in radiography

Contents

4.1 Introduction and motivation 36

4.2 Materials and methods 37

4.2.1 Measurement of the electron density 37

4.2.2 Data acquisition and analysis 39

4.2.3 Samples 40

4.3 Results and discussions 41

4.3.1 Synchrotron source 42

4.3.2 Laboratory source 44

4.4 Conclusions and summary 44

In this chapter, a method for quantitative measurements in radiography using a grating interferometer is described. In order to ensure fast measurements of electron density on a vast number of various homogeneous materials, a special sample geometry was used. Using the grating interferometer described in the previous chapter, at its design energy of 45 keV, a series of measurements was performed to validate the approach. A batch of various plastic materials was characterized quantitatively and the measured values were compared with theoretical values. The presented results show that the measured electron densities closely match theoretical values. A measurement at a synchrotron beamline with a monochromatic X-ray source was performed as a benchmark and further extended to a polychromatic X-ray tube setup. The technique yields comparable results regardless whether a monochromatic or a polychromatic X-ray source was used. Measured electron densities were further used to design dedicated X-ray phase-contrast phantoms, as explained in Chapter 6, and the additional information on (ultra-)small-angle scattering was taken into account in order to exclude unsuitable materials.

The majority of the results presented in this chapter were published in:
A. Sarapata, M. Chabior, C. Cozzini, J. I. Sperl, D. Bequé, O. Langner, J. Coman, I.

Zanette, M. Ruiz-Yaniz and F. Pfeiffer, "Quantitative electron density characterization of soft tissue substitute plastic materials using grating-based X-ray phase-contrast imaging," Review of Scientific Instruments **98**, 094101 (2011).

4.1 Introduction and motivation

Many scientific research areas rely on accurate electron density characterizations of various materials. For instance, in X-ray optics and radiation therapy, there is a need for a fast and reliable technique to quantitatively characterize samples for electron density. Moreover, whenever X-ray phase-contrast imaging is used in a clinical environment, dedicated phase-contrast phantoms will be necessary for quality assurance and performance evaluation purposes. More specifically, different CT setups have to be compared in their performance and ability to correctly image soft tissues. For that reason, in attenuation-based CT, the physical properties of the human tissue are represented by phantom materials with specific elemental composition (i.e. attenuation coefficients [White *et al.* 1977b]), whereas for phase-contrast CT, the phantom materials should have the exact electron density.

Medical imaging is not the only field in which electron density values are essential. Among others, they are also used for calculating the stopping power of protons in radiotherapy treatment planning [Cheng *et al.* 2013] and for determining the dose distribution in radiotherapy treatment that uses γ-ray or X-ray photons [Kalef-Ezra *et al.* 1998]. In addition, materials employed for X-ray optics have to be characterized for their refractive indices as the optical performance depends on the refractive properties of the materials under investigation.

It is thus important to be able to precisely measure the refractive index decrement δ of various materials and tissues because it ultimately determines the electron density. For simplicity, it is preferable to use electron densities instead of refractive index decrement values as they are independent of the X-ray energy. Since grating interferometry is highly sensitive to refraction of X-rays it is well suited for that purpose.

This chapter explains how a precise measurement of electron density of a homogeneous sample in a controlled geometry can be performed using an X-ray grating interferometer in a radiographic mode. This method is very time-efficient as it does not require a tomography scan where multiple projections have to be acquired at different rotation angles of the sample. However, a limitation of using a grating interferometer in a radiographic mode to measure electron densities, is that the analysis of objects with complex geometries is not possible.

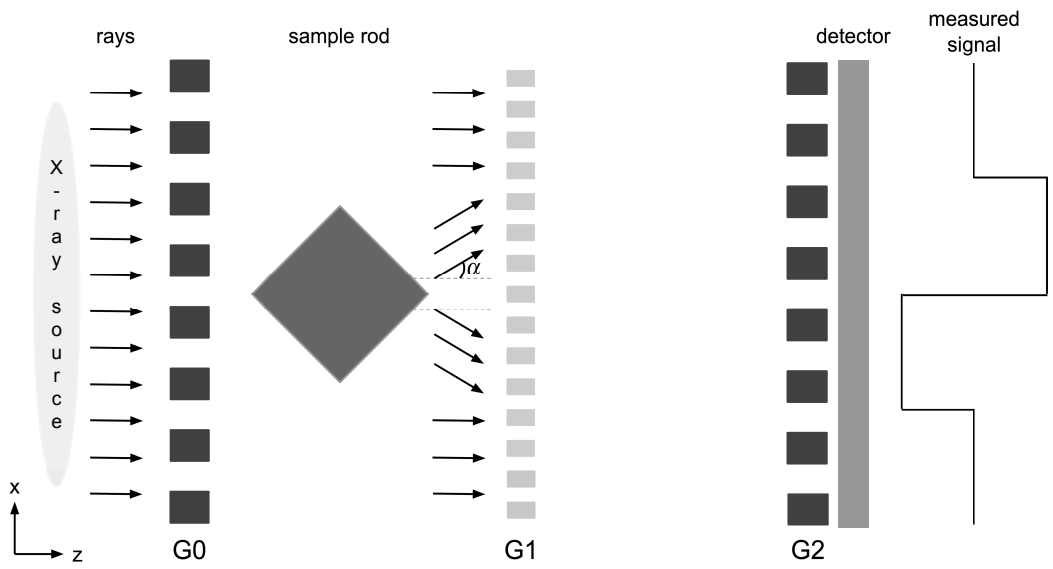

Figure 4.1: Schematic view of a Talbot-Lau interferometer using a polychromatic X-ray source. The sample is placed into the beam such that it yields a constant differential phase shift. Object and distances are not in scale. Figure adapted from [Sarapata *et al.* 2014a].

4.2 Materials and methods

4.2.1 Measurement of the electron density

The refractive index decrement δ depends on the energy E of the X-ray photons and the density of the sample [James 1967]:

$$\delta = \frac{r_0 h^2 c^2}{2\pi E^2} \sum_{i=1}^{n} N_i f_i^1 \,, \tag{4.1}$$

where r_0 is the classical electron radius, h is the Planck's constant, c is the speed of light, N_i is the atomic density of an atom i given per unit volume, and f_i^1 is the real part of their atomic scattering factor in the forward direction. If the X-ray photon energy of the incident beam is higher than the absorption edges of the investigated material, f_i^1 can be replaced by the element's atomic number Z_i such that the sum $\sum_{i=1}^{n} N_i f_i^1$ reflects the electron density ρ_e of the material [Guinier 1994]. At a monochromatic X-ray photon energy of 36 keV as used in the following, this approximation is valid for all elements with Z $<$ 54, corresponding to all of the materials chosen for this study. This approximation holds as well true for measurements performed with a grating interferometer operated at its design energy of 45 keV at a polychromatic source. Therefore, for all the samples investigated in this study, the electron density ρ_e is proportional to the refractive index decrement δ by:

$$\rho_e = \frac{2\pi E^2}{r_0 h^2 c^2} \delta. \tag{4.2}$$

Considering a well-defined homogeneous sample of square-rod shape and placed it into the beam along its diagonal (Fig. 4.1), the expected refraction angle α is constant along the faces of the rod and proportional to the refractive index decrement δ [Donath *et al.* 2009a]:

$$\alpha = \frac{\lambda}{2\pi}\frac{\Delta\Phi}{\Delta x} = \pm 2\delta. \tag{4.3}$$

Furthermore, the refraction angle α is directly proportional to the measured phase shift $\Delta\varphi$ of the intensity oscillation, the period p_2 of the analyzer grating and the distance d between the gratings G1 and G2,

$$\alpha = \frac{p_2}{2\pi d}\Delta\varphi. \tag{4.4}$$

Thus, the refraction index decrement δ can be calculated from the measured phase shift $\Delta\varphi$:

$$\delta = \frac{p_2}{4\pi}\frac{\Delta\varphi}{d}. \tag{4.5}$$

Combining equations (4.2) - (4.4), one finds that for the presented specific sample geometry the electron density is proportional to the measured phase shift $\Delta\varphi$, with the known period p_2 of the analyzer grating, distance d between the gratings G1 and G2 and energy E of the X-ray beam as parameters:

$$\rho_e = \frac{1}{2r_0h^2c^2}\frac{p_2}{d}E^2\Delta\varphi. \tag{4.6}$$

This allows a direct and fast measurement of the electron density ρ_e.

Two sets of experiments were performed with two different X-ray grating interferometers. Firstly, a benchmark measurement was performed at the beamline ID19 of the European Synchrotron Radiation Facility (Grenoble, France). Since the monochromatic energy of the X-ray beam was known, the experiment was performed as a reference measurement of the electron density. Secondly, the same samples were measured using a Talbot-Lau grating interferometer with a polychromatic source presented in Chapter 3. As the electron density is proportional to the square of the X-ray photon energy (Eq. 4.2), in the polychromatic case, a reference material (a well defined PMMA rod of known mass and electron density) allowed to calculate the effective photon energy. The effective energy was determined by matching the measured and the calculated data of refractive index decrement in order to calculate electron density values of unknown materials.

The corresponding results from both experiments were compared with each other and with expected theoretical electron density values.

4.2.1.1 The synchrotron setup

The grating interferometer at ID19 was operated at its design X-ray energy of 36 keV in the 5th fractional Talbot order. The energy was chosen as a good compromise between beam hardening artifacts prominent at low keV and poor image contrast at high keV. As the coherence of the synchrotron radiation generated at this beamline is high enough, the interferometer consists of only two gratings, omitting the source grating (G0). The phase grating (G1) with a period of 4.77 µm and height of 44 µm made of silicon was produced by the Laboratory of Micro and Nanotechnology of the Paul Scherrer Institut (Switzerland). The absorption grating (G2) was produced by the Karlsruhe Institute of Technology (Germany) with a period of 2.4 µm, height of 74 µm and made of gold. The mean fringe visibility during the measurements reached 28%. A more detailed description of the interferometer at the beamline ID19 can be found in [Weitkamp *et al.* 2010].

The X-ray photons were generated by a wiggler and monochromatized by a Si double crystal monochromator in Bragg geometry. The X-rays had a nominal energy of 36 keV. The detector was an indirect conversion system consisting of a 200 µm thick $Lu_3Al_5O_{12}$:Ce scintillator and a lens coupled to a CCD camera with an effective pixel size of 8 µm.

4.2.1.2 The lab-based setup

A high-power COMET MXR-160HP/11 tube with a stationary tungsten anode served as an X-ray source. The tube was operated at 75 kVp and 20 mA. Again, the accelerating voltage was chosen as a good compromise between beam hardening artifacts prominent at low energies and poor image contrast at high energies. The emitted radiation was filtered with 2 mm of aluminum and the beryllium window of the X-ray tube, which resulted in X-ray spectrum with a mean energy of approximately 44 keV. A Varian PaxScan 2520D with a 600 µm thick structured CsI(Tl) scintillation layer and 127 µm physical pixel size served as a detector. The grating parameters are described in section 3.5.

4.2.2 Data acquisition and analysis

In both cases, a phase stepping procedure was used in order to acquire phase-contrast images. The phase grating G1 was scanned laterally by either 4 steps (the synchrotron setup) or 8 steps (the lab-based setup) over one period of the interference pattern created by the grating. The differential phase images were extracted by Fourier analysis [Pfeiffer *et al.* 2008] of the intensity oscillation curves in each detector pixel obtained from phase-stepping scans with and without the sample in the field of view.

Differential phase contrast projection images were obtained separately for all the rods. For every image, two regions of interest (ROIs) on opposite sides of the rod were chosen (see Figure 4.2) for which the mean phase shift value and its standard deviation

were determined. Furthermore, the mean values of these two ROIs were subtracted from each other and divided by two in order to eliminate any signal offsets. That obtained quantitatively exact phase shift value allowed to calculate refractive index decrement (Eq. 4.5) and subsequently electron density by Eq. 4.2. The error in the resulting phase shift was calculated using error propagation of the standard deviation of the values in the ROIs and further to compute the uncertainty of electron densities.

The error bars shown in Figure 4.3 and Figure 4.4 correspond to uncertainties calculated by error propagation for Eq. 4.6. For the calculation, the error of the X-ray photon energy was assumed to be either 100 eV (monochromatic synchrotron X-rays) or 2 keV (polychromatic lab source), the error of the distance between the gratings G1 and G2 was estimated to 2 mm whereas the error in the period of the analyzer grating G2 was considered to be negligible.

4.2.3 Samples

Various homogeneous plastic materials were provided by the Quality Assurance in Radiology and Medicine GmbH (QRM, Möhrendorf, Germany) in the form of square bars with a side length of 10 mm and a height of 50 mm. Most of the materials used to produce the samples were obtained from commercial manufacturers, while a few others were casted by QRM. During the experiment, the samples were placed into the X-ray beam along their diagonals and adjusted such that, in a good approximation in projection, they exhibited a lateral height profile of a triangular shape. Hence a constant differential phase shift of opposite signs was observed. The samples were aligned using a designated sample holder, which ensured the same exact position and a rotation angle of 45° for each of the rods. Table 4.1 presents a list of all materials chosen for the experiment. Many of the chosen plastic materials are commonly used in production of phantoms for conventional, attenuation-based imaging. Typically, these materials are selected based on how their X-ray attenuation properties correspond to a specific tissue type [White 1978]. They were investigated in order to ensure their suitability for phase-contrast imaging and to test their refraction properties.

In addition, the casts of water-, tissue-, and bone-equivalent materials were examined. These particular samples were prepared using epoxy resin as a base material with other components as additives [Yohannes *et al.* 2012]. Calcium carbonate ($CaCO_3$) powder with grain size of up to 10 µm, and various other microspheres available from commercial manufacturers were added to the mixtures. These additives create a highly porous microstructure, which causes (ultra-)small-angle scattering of X-rays. Scattering reduces the spatial coherence of the X-ray beam which is directly related to the measurement of the differential phase. Simply put, as the decoherence gets stronger, the measurement of the phase shift becomes less precise. Hence, for a mixture of epoxy resin with such microspheres the phase signal might no longer be measured with sufficient certainty. The strength of scattering depends on the size of the micro-structures in relation to the grating period [Malecki *et al.* 2012]. For that

reason, a suitability of these materials for X-ray phase-contrast imaging was tested. More detailed explanation and consideration of this topic is presented in Section 6.2.

Theoretical electron density values were determined as a reference for the experiment using Eq. 4.2. Knowing the chemical formula and the density of the samples, the refractive index decrement δ values were calculated based on the adapted version of Mucal written by [Bandyopadhyay & Segre 2009] as described by [Malecki *et al.* 2012]. The calculations were based solely on the chemical composition of the plastic materials. However, commercial manufacturers commonly use additives of unknown composition and weight percentage for easier handling of the plastics. For these materials, a small discrepancy of a few percent between the measured and the theoretical values was expected. In Table 4.1 each of them is marked with an asterisk next to its name.

4.3 Results and discussions

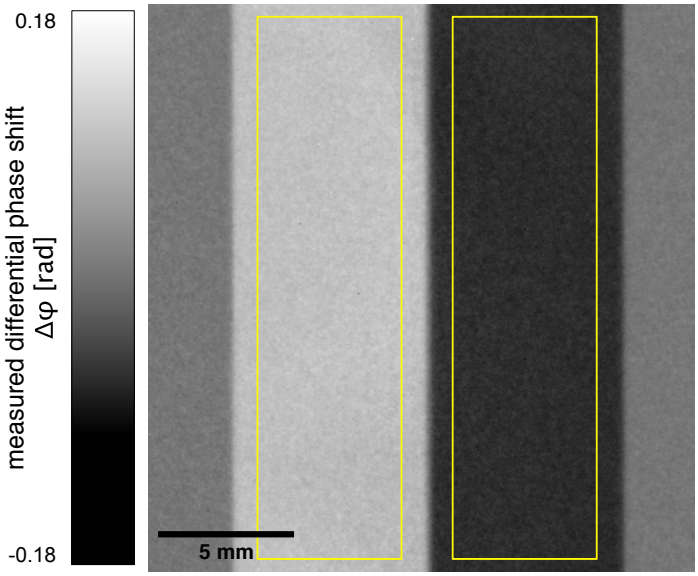

Figure 4.2: Image of the measured differential phase shift $\Delta\varphi$ of a PMMA rod used as a reference material. Two regions of interest, as shown in yellow, were defined for each rod to obtain experimental values shown in Figure 4.3 and 4.4. Figure adapted from [Sarapata *et al.* 2014a].

Figure 4.2 shows a differential phase contrast image of one of the rods obtained using the phase stepping technique. It represents the phase shift $\Delta\varphi$ of the intensity oscillation which can be further related to the refraction index decrement δ and the electron density. It exhibits a symmetry along the diagonal of the rod, with the same phase shift values but opposite signs on both sides of the rod.

The effective energy of the X-ray beam was determined by matching the measured and the calculated data for a PMMA rod. The minimum difference between measured and calculated values was found for 43.7 keV, determined with a resolution of 0.1 keV. Note that the effective energy is close to the interferometer design energy of 45 keV.

Table 4.1: Comparison of theoretical electron density values of all the materials with values measured using a monochromatic and a polychromatic X-ray source. The values are also plotted in Fig. 4.3 and 4.4. Table adapted from [Sarapata *et al.* 2014a].

Material	Density [g/cm^3]	Theoretical ρ_e x10^{26} [e/m^3]	Monochromatic ρ_e x10^{26} [e/m^3]	Polychromatic ρ_e x10^{26} [e/m^3]
Polyurethane PUR 1	1.138	3733	3674 ± 70	3635 ± 138
PUR 2	1.082	3549	3491 ± 72	3566 ± 145
[a]PTFE*	2.164	6259	6150 ± 106	6072 ± 170
Epoxy resin EP 1	1.120	3666	3619 ± 68	3645 ± 136
EP 2	1.131	3700	3622 ± 89	3688 ± 122
EP 3	1.127	3689	3622 ± 78	3632 ± 147
EP 4	1.131	3700	3704 ± 85	3589 ± 163
EP 5	1.126	3685	3594 ± 91	3653 ± 167
[b]PVC 1*	1.364	4210	4103 ± 101	3889 ± 196
PVC 2*	1.371	4230	4098 ± 105	3908 ± 192
Polyethylene PE 1*	0.946	3250	3185 ± 84	3246 ± 132
PE 2*	0.953	3276	3300 ± 57	3280 ± 114
Polypropylene PP*	0.905	3110	3094 ± 98	3111 ± 155
Polyamide/Nylon PA*	0.999	3302	3302 ± 56	3334 ± 112
[c]POM 1*	1.426	4578	4567 ± 76	4577 ± 152
POM 2*	1.421	4562	4558 ± 64	4530 ± 128
[d]PMMA*	1.187	3858	3792 ± 80	-
Polycarbonate PC*	1.196	3851	3779 ± 86	3798 ± 149
Water equiv. material	1.018	3285	-	-
Bone equiv. material	1.180	3839	-	-
Tissue equiv. material	1.075	3505	-	-

[a]Polytetrafluoroethylene
[b]Polyvinyl chloride
[c]Polyoxymethylene
[d]Polymethylmethacrylate

The QRM casts of water-, bone- and tissue-equivalent materials scattered, as expected, too strongly for the electron density to be quantified with reasonably low measurement error at both grating interferometer setups. Therefore, for these samples, no experimental values are given in Table 4.1.

4.3.1 Synchrotron source

Figure 4.3 shows a comparison of electron density values obtained using monochromatic X-rays generated by the synchrotron, with the values calculated theoretically. All of the values match each other within the calculated uncertainties. This proves that the presented method and the chosen sample geometry provide reliable values of electron density for plastic materials with a big range of densities.

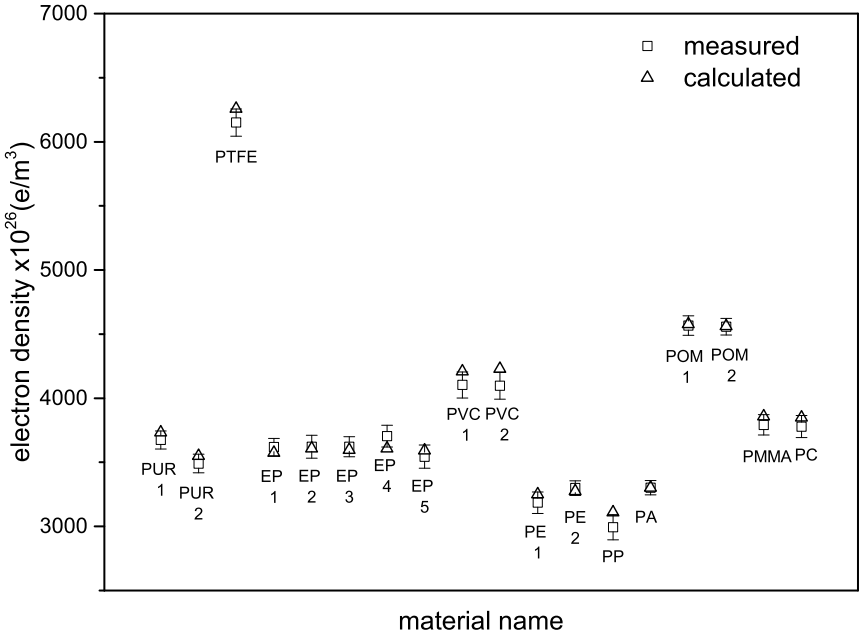

Figure 4.3: Scatter plot of electron density values measured with monochromatic synchrotron X-rays and theoretically calculated values for all the samples with negligible scattering. Figure adapted from [Sarapata *et al.* 2014a].

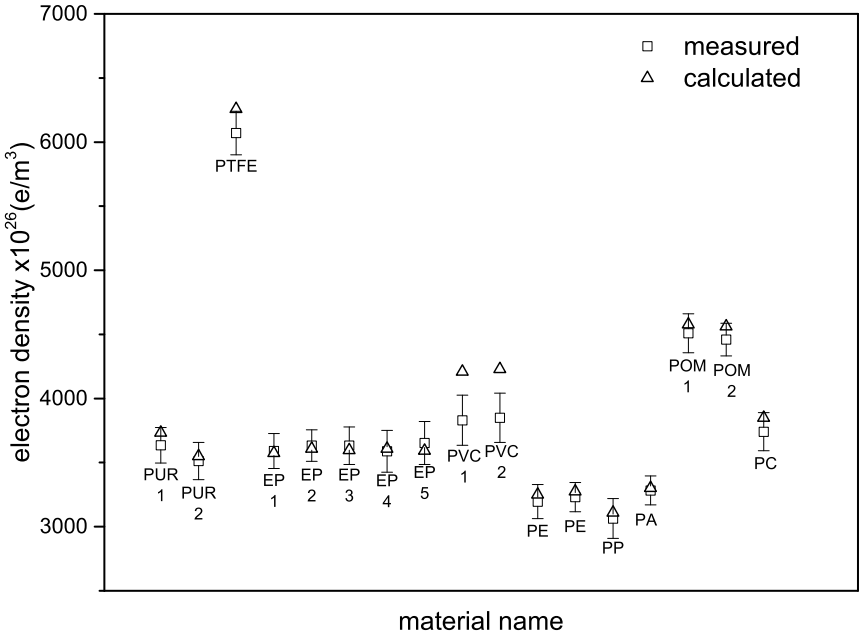

Figure 4.4: Scatter plot of electron density values measured with a polychromatic lab source and theoretically calculated values for all the samples with negligible scattering. Figure adapted from [Sarapata *et al.* 2014a].

4.3.2 Laboratory source

The values measured using a polychromatic source, match the theoretical values within the calculated uncertainties for almost all materials (Fig. 4.4). Overall, the values are slightly underestimated in most cases, which could be a result of a mismatch of effective energy due to the uncertainty of the exact composition, thus electron density, of the PMMA rod used for the calibration. As mentioned previously, the manufacturers use unknown additives which cannot be taken into account when calculating the theoretical values. In addition, the inaccurately measured distance between the gratings G1 and G2 could have caused this slight offset.

Experimental values for highly absorbing PTFE and PVC are significantly lower than the calculated ones. For these samples, we observed a non-flat profile as the absorption increases with the material thickness. This effect is associated with beam hardening [Chabior *et al.* 2011]. As the X-ray beam propagates through a highly absorbing material, most of the low energy part of the spectrum is completely absorbed. As a result, the X-ray spectrum after it exits such a sample has a higher mean energy (we say it is "harder") than the spectrum before it reaches the sample. Since the PMMA rod used to estimate the effective energy of the beam has a low attenuation coefficient, the X-ray spectrum after it traverses through is slightly "softer" than the spectrum after a highly absorbing material such as PTFE. This causes an underestimation of the electron densities and the discrepancy with theoretical values. This effect was not observed for synchrotron data because of the monochromaticity of the beam.

Results obtained with the polychromatic lab-based setup characterize higher measurement error than the ones obtained with the monochromatic synchrotron radiation. It is a result of a lower photon flux thus lower photon statistics and higher uncertainty of the effective X-ray photon energy. The former could be accounted for by increasing the measurement time.

4.4 Conclusions and summary

In summary, this chapter demonstrated the possibility to measure refractive index decrement and electron density of homogeneous materials of a well-defined shape using grating-based X-ray phase-contrast projection imaging. Either a monochromatic or a polychromatic X-ray source can be used to characterize various homogeneous materials. All the obtained values agree well with theoretical calculations within the uncertainty levels, but are slightly underestimated in most cases. In the polychromatic case, the need for a reference material and use of the effective energy limits the quantitativeness of the technique. Samples with relatively low absorption should be of main interest for the presented X-ray energy range. However, the samples being homogeneous objects, beam hardening artifacts could be corrected for high-Z materials by a linearization technique following [Chabior *et al.* 2011]. Defined shape of the sam-

ple and its homogeneity set stringent requirements preventing a similar analysis, for instance, of biological tissues. Nevertheless, with the method, the electron densities of nearly 20 samples made of varying plastic materials were successfully determined. Thereby, dedicated dedicated X-ray phase-contrast phantoms were designed as explained in Chapter 6.

Inhomogeneous water-, bone- and tissue-equivalent materials containing microspheres, could not be characterized for their electron density using the presented method. The strong scattering caused by these samples decreased the coherence of the X-ray beam such that the measurement of the phase shifts were no longer possible. Having that in mind, it is suggested that looking for a suitable tissue-simulating material for X-ray phase-contrast imaging not only the similarity to soft tissues in refractive index decrement values should be a considered parameter, as discussed in [Vedantham & Karellas 2013]. One should also take the (ultra-)small-angle scattering into account.

Avoiding a time-consuming CT scan, makes the presented method preferable for thorough studies of various materials. A big impact of this method can be expected in all fields which require the knowledge of electron density, e.g., the aforementioned soft tissue phantom design dedicated for X-ray phase-contrast imaging, characterization of the materials used in X-ray optics, radiation therapy, and other research areas.

Chapter 5

Quantitative computed tomography

Contents

5.1 Introduction 47

5.2 Materials and methods 48

5.2.1 Grating size as a limiting factor of a large field of view 48

5.2.2 Image contrast dependence / formation 49

5.2.3 Samples 51

5.2.4 Experimental setup, data acquisition and analysis 51

5.3 Results and discussions 53

5.3.1 Low-Z materials phantom 53

5.3.2 High-Z materials phantom 55

5.3.3 Intervertebral discs 58

5.4 Conclusions 59

As shown in the previous chapter, grating interferometry allows for experimental access to electron density values. The radiographic method has certain limitations concerning the sample geometry and the type of materials that can be analyzed. These can be overcome by computed tomography (CT) at the expense of increased measurement time and the radiation dose. This chapter presents quantitative grating-based X-ray phase-contrast CT and investigates the complementarity of both attenuation- and phase-contrast modalities with materials of various atomic numbers (Z). For that purpose, the high-energy grating interferometer presented in Chapter 3.5 was used with a large (10 cm in diameter) analyzer grating and operated at an acceleration tube voltage of 70 kVp. It is confirmed experimentally that for low-Z materials, phase contrast yields no additional information over attenuation images, yet it provides increased contrast-to-noise ratios (CNRs). The complementarity of both signals can be seen again with increasing Z of the materials and a more comprehensive material characterization is thus possible. The benefit of a high-energy X-ray phase-contrast system is showcased by imaging results of a part of a human cervical spine with intervertebral discs surrounded by bones and various soft tissue types. Phase-contrast reconstruction reveals the internal structure of the discs and makes the boundary between the disc annulus and nucleus pulposus visible.

The majority of results presented in this chapter were published in:
A. Sarapata, M. Willner, M. Walter, T. Duttenhofer, K. Kaiser, P. Meyer, C. Braun, A. Fingerle, P. B. Noël, F. Pfeiffer, and J. Herzen, "Quantitative imaging using high-energy X-ray phase-contrast CT with a 70 kVp polychromatic X-ray spectrum," Optics Express **23**, 523-535 (2015).

5.1 Introduction

Imaging of large and dense objects with grating-based X-ray phase-contrast CT (gbPC-CT) requires X-ray photons with high energies and large fields of view (FOVs). However, due to limitations in the grating fabrication process, the technique has so far been restricted to X-ray energies below 40 keV and small FOVs. Mainly relatively small samples (maximum 30 mm in diameter) composed of low-Z materials have been investigated [Hetterich *et al.* 2014, Willner *et al.* 2014, Herzen *et al.* 2014]. When larger samples are of interest, the rotation axis can be positioned asymmetrically in order to increase the effective field of view [Schulz *et al.* 2010]. However, good results can only be achieved with parallel beam reconstruction (synchrotron measurements) and at the expense of increased measurement time.

As grating fabrication processes improve, gbPC-CT becomes feasible with higher X-ray energies. New possible applications are being investigated thanks to the higher penetration depth of photons above 40 keV. For instance, grating interferometry at 82 and 130 keV photon energy using a synchrotron source has been already demonstrated [Willner *et al.* 2013, Ruiz-Yaniz *et al.* 2015]. The phase-contrast images in these examples showed increased CNRs in comparison to the attenuation-contrast images. However, access to synchrotron radiation sources is severely limited because of their high operation costs. Therefore, a high-energy phase-contrast CT system using a conventional X-ray source is desirable.

Even though a proof-of-principle study of gbPC-CT at a laboratory source at 60 keV has been demonstrated earlier in [Donath *et al.* 2009b], due to a very low fringe visibility of 3% the performance of the interferometer was inferior and not sufficient to perform imaging with satisfactory contrast or image quality gain between the phase and the attenuation-contrast reconstructions. Slightly different approaches have been presented to build improved-in-performance laboratory systems [Sarapata *et al.* 2014b, Thuering *et al.* 2014], but the field of view in these cases is to a certain extent limited.

This chapter presents quantitative CT imaging results obtained using the high-energy grating interferometer presented in Chapter 3.5 with a round 10 cm analyzer grating for an increased FOV. The system is characterized for its ability to reliably provide the quantitative electron density (related to the X-ray refractive index decrement) and the X-ray attenuation coefficient values of the chosen samples.

Furthermore, a second study is dedicated to experimentally demonstrate to which

extent the complementarity of phase and attenuation contrast, shown at low X-ray energy for low-Z materials [Herzen *et al.* 2009], is still retained since it is known from a monochromatic case to become less pronounced at higher photon energies for low-Z materials [Willner *et al.* 2013].

Lastly, an intervertebral fibrocartilage surrounded by bones was imaged and tomography reconstructions are presented as an example of a potential application of grating-based PC-CT in this photon energy range. The internal structure of the intervertebral disc shows improved contrast in the phase image and allows to differentiate the fibrous capsule from the gelatinous center as previously achieved only by magnetic resonance imaging.

5.2 Materials and methods

5.2.1 Grating size as a limiting factor of a large field of view

In order to fully take advantage of the elevated X-ray energy and measure relatively large objects, bigger fields of view are necessary. In the cone-beam geometry, the size of the analyzer grating G2 placed in front of the detector is the limiting factor.

The X-ray LIGA process used for manufacturing the analyzer gratings can routinely deliver gratings up to 70 mm in diameter [Reznikova *et al.* 2008, Mohr *et al.* 2012]. The dimension corresponds to the overall size of the grating structures, which are manufactured on a slightly bigger silicon wafer. This limitation in size results from both the technology employed for the X-ray mask membranes and from the patterning of the mask microstructures (i.e. the grating lines). With respect to the first cause, microworks GmbH (Karlsruhe, Germany) has developed new approaches for X-ray mask membranes: a thin polyimide membrane (6 µm) replaces the established titanium membrane [Meyer *et al.* 2010]. This allows the masks to be manufactured with diameters of 100 mm or larger and further used for direct lithographic manufacturing of gratings with thicknesses of up to 100 µm. For thicker structures, a harder X-ray spectrum is required. With such a spectrum, it is possible to use silicon wafers (100 µm in thickens) as mask substrates. These offer an improvement in stiffness, rigidity and thermal conductivity compared to the standard titanium membranes used to date. The most crucial feature of these mask substrates is given by the lithographic window of as much as 100 mm in diameter. In order to obtain high-quality and high-aspect-ratio gratings, in the first step, a polyimide-based intermediate mask is patterned using direct-write-laser lithography (DWL). With this mask, structures of up to 100 µm thickness are patterned or, as in our case, a silicon-based working mask is fabricated via X-ray lithography. The resulting masks allow to manufacture gratings with thicknesses of up to 300 µm.

In the following, phase-contrast CT images obtained with a round analyzer grating of 10 cm in diameter and 150 µm in height gold structures are presented. To the

author's knowledge, it is the grating interferometer with the biggest FOV reported to date. This constitutes a very significant advance towards broadening the applicability of the technique and opening a wide range of possible applications in materials science and biomedical imaging. Moreover, recent studies demonstrate the possibility of even further increased field of views by means of stitching several gratings together [Meiser *et al.* 2014]. However, this method has not yet been tested with gratings of such high structures (∼150 µm).

5.2.2 Image contrast dependence / formation

On the one hand, a phase-contrast image represents the local distribution of the refractive index decrement δ [Wilson 1950]:

$$\delta = \frac{r_0 h^2 c^2}{2\pi E^2} \sum_{i=1}^{n} N_i f_i^1, \tag{5.1}$$

where r_0 is the classical electron radius, h is the Planck's constant, c is the speed of light, E is the X-ray photon energy, N_i is the atomic density of type i atoms given per unit volume, and f_i^1 is the real part of their atomic scattering factor in the forward direction. At X-ray photon energies far away from the absorption edges, the refractive index decrement is related to the electron density ρ_e and the energy of the X-ray photons by [James 1967]:

$$\rho_e = \frac{2\pi E^2}{r_0 h^2 c^2} \delta. \tag{5.2}$$

Thus, the local electron density distribution inside the sample is accessible with phase-contrast imaging.

An attenuation contrast image, on the other hand, is the result of photoelectric absorption, Compton scattering and coherent scattering in the photon energy range of interest in biomedical CT scanning [McCullough 1975]. Therefore, the linear attenuation coefficient μ can be decomposed into contributions from each mode of X-ray photon interaction as

$$\mu = \mu_{pe} + \mu_{coh} + \mu_{incoh}, \tag{5.3}$$

where *pe* is the photoelectric effect, *coh* is the coherent Rayleigh scattering and *incoh* is the incoherent Compton scattering. Furthermore, the linear attenuation coefficient μ is the product of the total electronic cross section σ_{tot}^e (cross section per electron) and the electron density of the material ρ_e with

$$\mu = \rho_e \sigma_{\mathrm{tot}}^e = \rho_e(\sigma_{\mathrm{pe}} + \sigma_{\mathrm{coh}} + \sigma_{\mathrm{incoh}}). \tag{5.4}$$

Both the electronic cross sections for the photoelectric effect and the coherent scattering depend not only on the photon energy E, but also on the material specific

effective atomic number Z_{eff}

$$\sigma_{\text{pe}} = const \cdot \frac{Z_{eff}^{k}}{E^{l}} \tag{5.5}$$

and

$$\sigma_{\text{coh}} = const \cdot \frac{Z_{eff}^{m}}{E^{n}}, \tag{5.6}$$

where values for k and m are typically 3.8 and 2.0, respectively, and values for l and n are 3.2 and 1.9, respectively, but vary slightly depending on the photon energy and on the composition of the material [McCullough 1975].

In contrast to these two effects, the Compton scattering cross section σ_{incoh} depends only on the X-ray energy and is essentially independent of the atomic number Z [Hubbell 1969, McCullough 1975]. Therefore, for low-Z materials at high photon energies, the linear attenuation coefficient is nearly proportional to the electron density. For instance, soft-tissue contrast of human organs in medical CT examinations in based purely on the Compton effect so that it represents distribution of electron densities inside the patients.

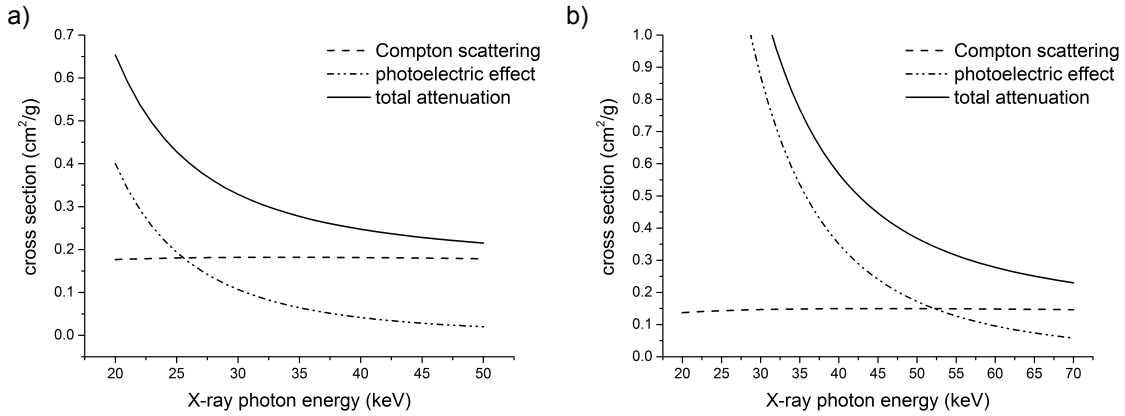

Figure 5.1: Photon cross-sections calculated for ethylene glycol (a) and aluminum (b) based on the data from XCOM database [Berger *et al.* 2010]. Figure adapted from [Sarapata *et al.* 2015b].

As seen in Fig. 5.1(a), the attenuation of ethylene glycol ($C_2H_6O_2$) due to the photoelectric effect decreases with the X-ray energy and becomes less than that of the Compton effect just above 26 keV. Only for X-ray energies below 26 keV is the photoelectric effect the dominant process, and thus the biggest contribution to the attenuation contrast. The more the attenuation process results from the Compton effect, the more the attenuation-based image is proportional to the electron density, as is also the case in the phase contrast. No additional information on the material composition can be gained if attenuation is mostly attributed to Compton scattering [Willner *et al.* 2013]. Thus, for all low-Z materials similar contrast differences are

expected for attenuation and phase contrast images at high X-ray energies. Signal-to-noise ratios and contrast-to-noise ratios will however differ and depend mainly on the performance of the grating interferometer. For instance, the higher the fringe visibility, the higher these values will be in favor of phase contrast [Köhler *et al.* 2011].

The situation changes for higher atomic number materials like aluminum (see Fig. 5.1(b)). At 45 keV mean X-ray energy, the attenuation contrast is a result of both effects. Therefore, attenuation- and phase-contrast images provide complementary information and materials can be more easily distinguished as seen in the monochromatic case [Willner *et al.* 2013].

5.2.3 Samples

In order to experimentally investigate the discussed complementarity of phase and attenuation contrast, two different phantoms were designed. The first phantom, composed of well-defined liquids in different concentrations, was prepared to represent various low-Z materials (for the simplicity in the following called low-Z phantom). Each of the liquids was placed in a cylindrical tube made of polyethylene (PE). All of the tubes were then placed in a bigger cylindrical container filled with deionized water. The diameter of the outer container was 50 mm. Table 5.1 presents a list of all the liquids inside the phantom.

The second self-made phantom was made of higher-Z materials (for the simplicity in the following called high-Z phantom). Five rod-shaped materials were fixed at the top and placed in a 35 mm thick water tank during the measurements. The materials contain heavier elements with Z ranging from 9 (fluorine) to 17 (chlorine). Table 5.3 presents a list of all the materials inside the phantom.

Additionally, to demonstrate the capabilities of X-ray phase contrast imaging at 70 kVp, a part of a human cervical spine with intervertebral discs surrounded by bones and various soft tissue types was placed in a 40 mm diameter plastic container filled with formalin. The specimen was provided by the Institute of Forensic Medicine, Ludwig-Maximilians-Universität (Munich, Germany) in accordance with the Declaration of Helsinki and approved by the local ethics committee.

5.2.4 Experimental setup, data acquisition and analysis

A description of the experimental setup and its parameters can be found in Chapter 3.5. In the following only the varying and the specific components used in the experiments are described.

The X-ray tube was operated at 70 kVp and 27 mA, with an effective source size of 1x1 mm^2. For measurements of the low-Z phantom and the biomedical sample, the emitted radiation was filtered with 60 mm of water, 2 mm of aluminum and the beryllium window of the X-ray tube resulting in an X-ray spectrum with a mean photon energy of about 45 keV, calculated by the *SpekCalc* program [Poludniowski *et al.* 2009].

A mean fringe visibility of 20 % was achieved (calculated in a circular area around the middle covering half of the FOV). In case of the high-Z phantom, 0.6 mm of copper, 2 mm of aluminum and 36 mm of water pre-filtered the beam. The resulting X-ray spectrum had a mean energy of approximately 51 keV. The change of filtering was necessary to prevent beam hardening artifacts and, therefore, inaccuracies in the quantitative analysis. In this case, the mean fringe visibility was 15 %.

The samples were placed downstream of the phase grating G1 and submerged in a rectangular water tank during the experiment to avoid beam hardening and phase wrapping artifacts at the boundary between the air and the plastic containers. The distance between the sample and the phase grating and the tank thickness varied from sample to sample. The low-Z phantom and the biomedical specimen were submerged in a 60 cm thick water tank and were located at a distance of about 7 cm from G1. The high-Z phantom was placed in a 36 mm thick water tank and approximately 5 cm away.

A phase-stepping procedure was applied in order to obtain attenuation- and phase-contrast images. The phase grating G1 was scanned laterally by eight steps over one period of the interference pattern created by the grating. Each frame was obtained with an exposure time of one second. The phase stepping was done separately for every rotation angle of the sample. Further, the two signals were obtained by a pixel-wise Fourier analysis [Pfeiffer *et al.* 2008] of the few frames acquired at different phase grating positions.

During the CT acquisition the sample was rotated in order to acquire multiple projections at different orientation angles. The phase stepping was done separately for every rotation angle of the sample. The whole CT scan consisted of 1,200 rotation angles over 360 degrees and lasted approximately 10 hours. For the CT reconstruction, a GPU-based cone-beam filtered back-projection reconstruction algorithm developed "in-house" by [Fehringer *et al.* 2014] based on a Ram-Lak filter for attenuation and a Hilbert filter for phase reconstruction was used. As a result of the reconstruction, two inherently registered volumes were obtained, i.e. the attenuation, and the phase-contrast volume. Bilateral filtering was applied to the datasets as a post-processing step, which decreased the overall noise in both reconstructions and helped to preserve the edges [Köhler & Roessl 2012].

Both linear attenuation coefficient μ and refractive index decrement δ strongly depend on the X-ray energy. For the comparison of measured and theoretical values and for the calculation of electron densities, the effective energy of the X-ray beam has to be known. It is important to note, that due to the different image formation process, the measurement of μ and δ are performed at slightly different effective energies. The measured effective energy is a result of the X-ray spectrum, the spectral efficiency of the detector, and the spectral efficiency of the grating interferometer. The last one especially differs between attenuation and phase contrast. Therefore, two effective energies were defined by matching the measured and the theoretical data of a reference

material. One of the materials inside each of the phantoms of known mass density and elemental weight fractions was used for this purpose. In the biological sample case, a PMMA and an epoxy resin rod were placed inside to serve as references.

Since the measurements were carried out in a water tank, the measured values of μ and δ are relative to water [Herzen *et al.* 2009]. In order to obtain the absolute values presented in Table 5.1 and 5.3, μ_{H2O} and δ_{H2O} of water for the corresponding effective energies were added to all experimental values.

For the quantitative analysis of the phantoms, 60 axial slices were averaged to increase the signal-to-noise ratio. Over each of the materials inside the phantoms, a "circular" region of interest (ROI) of 125 by 125 pixels was selected from which the mean values and standard deviations were obtained. Further, in order to quantify image quality differences, contrast-to-noise ratios were determined as

$$CNR = \frac{|S_a - S_b|}{\sqrt{(\sigma_a)^2 + (\sigma_b)^2}} , \tag{5.7}$$

where S_a and S_b represent the measured signals, i.e., mean values in circular regions chosen for each of the materials and σ_a, σ_b represent standard deviations of the mean for the respective regions.

As a reference for the measured values, knowing the chemical formula and the mass density of the materials, the theoretical refractive index decrement δ and linear attenuation coefficient μ values were calculated based on the adapted version of Mucal written by Bandyopadhyay and Segre [Bandyopadhyay & Segre 2009] as described by [Malecki *et al.* 2012]. Subsequently, theoretical electron density values were calculated using Equation (5.2).

5.3 Results and discussions

5.3.1 Low-Z materials phantom

Figure 5.2 shows attenuation- (a), and phase-contrast (b) axial slices reconstructed from the same CT data set obtained with the Talbot-Lau interferometer. The highest signal corresponds to the H_2O/glycerol mixture, the lowest to isopropyl alcohol. The contrast between various liquids is very similar for both images. This is due to the fact that both contrast modalities for these low-Z materials depend mainly on electron density. The dependence of attenuation contrast on material composition, namely on its effective atomic number, is greatly reduced at this X-ray energy.

The effective energy of the X-ray beam was determined by matching the measured and the calculated data for ethylene glycol. The minimum difference between measured and calculated values was found for 44.2 keV for phase contrast and 43.7 keV for attenuation, determined with 0.1 keV resolution.

The mean values and associated standard deviations of the linear attenuation

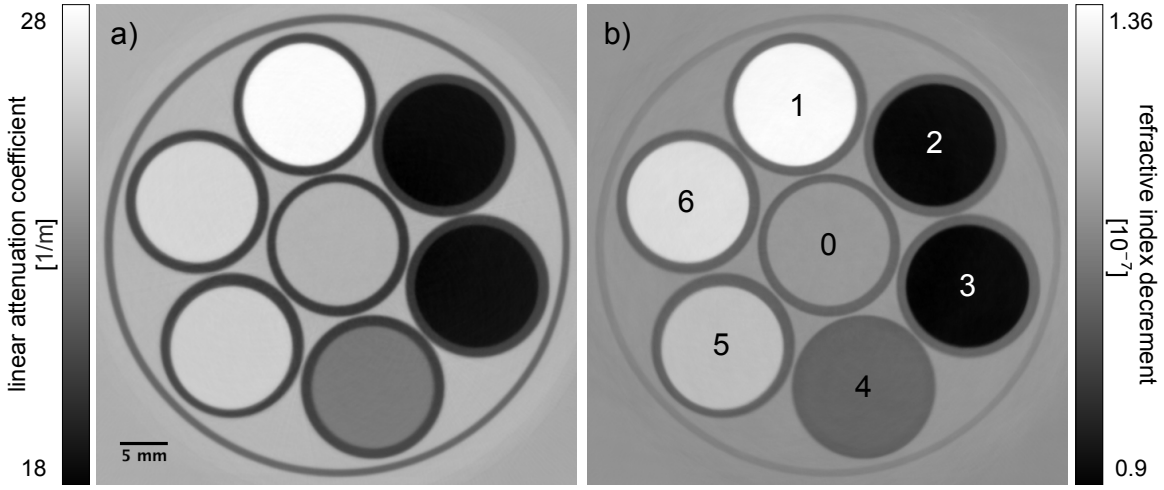

Figure 5.2: Comparison of axial slices from a tomographic reconstruction of the linear attenuation coefficient μ (a) and the refraction index decrement δ (b) distributions inside the low-Z phantom. The following liquids are represented in the images: 0 - water, 1 - H_2O/glycerol, 2 - isopropyl, 3 - ethanol, 4 - H_2O/ethanol, 5 - H_2O/ethylene glycol, 6 - ethylene glycol. Both images show a very similar contrast because of the dependence of image formation on electron density for both channels. Figure adapted from [Sarapata *et al.* 2015b].

coefficient μ, refraction index decrement δ and electron density ρ_e together with the theoretical values are presented in Table 5.1. The experimental values associated with the phase-contrast reconstruction, i.e. δ and ρ_e, match the theoretical values within one standard deviation. In attenuation contrast, the measured values of μ show a good agreement as well, but with stronger deviations from the theoretical values. The analysis is not affected by beam hardening artifacts thanks to the used beam filtering and because all the materials are relatively low absorbing at the applied high X-ray energy range.

In order to quantify image quality difference, contrast-to-noise analysis was performed. As seen in Table 5.2, phase contrast provides a contrast gain over attenuation in all the cases but one. Even though both of the contrast modalities depend on the

Table 5.1: Measured and theoretical (subscript th) attenuation coefficients μ, refraction index decrements δ and electron densities ρ_e for all fluids inside the low-Z phantom. This table was previously published in [Sarapata *et al.* 2015b].

Material	μ $[1/m]$	μ_{th} $[1/m]$	δ $[10^{-7}]$	δ_{th} $[10^{-7}]$	ρ_e $[10^{29}/m^3]$	ρ_e^{th} $[10^{29}/m^3]$
water	25.20 ± 0.04	25.25	1.18 ± 0.02	1.18	3.35 ± 0.03	3.339
H_2O/glycerol	27.54 ± 0.05	27.51	1.35 ± 0.02	1.33	3.79 ± 0.06	3.739
ethylene glycol	26.10 ± 0.04	26.13	1.30 ± 0.02	1.30	3.66 ± 0.05	3.664
H_2O/ethylene glycol	25.94 ±0.04	25.86	1.29 ± 0.02	1.27	3.53 ± 0.03	3.517
H_2O/ethanol	23.08 ± 0.05	22.98	1.03 ± 0.02	1.05	3.14 ± 0.05	3.094
ethanol	18.42 ±0.09	18.46	0.955 ± 0.02	0.951	2.72 ± 0.09	2.684
isopropyl	18.31 ± 0.10	18.21	0.953 ± 0.02	0.950	2.71 ± 0.04	2.680

Table 5.2: Contrast-to-noise ratios for phase contrast CNR_{phase} and attenuation contrast CNR_{abs} for selected sets of two materials inside the low-Z phantom. This table was previously published in [Sarapata *et al.* 2015b].

Material pair	CNR_{abs}	CNR_{phase}
water - H_2O/glycerol	39.3	64.8
water - H_2O/ethylene glycol	13.3	36.8
water - isopropyl	55.0	53.8
ethylene glycol - H_2O/ethylene glycol	4.8	21.2
ethylene glycol - H_2O/ethanol	45.9	74.5
ethylene glycol - ethanol	69.3	91.3
ethanol - water	60.5	65.5
ethanol - H_2O/glycerol	82.4	99.8
ethanol - H_2O/ethanol	35.9	41.2

materials' electron density, phase contrast provides higher quality images because of a different image formation process and higher sensitivity of the presented technique to changes in the phase of an X-ray beam passing through an object.

5.3.2 High-Z materials phantom

The previously discussed dependence of the attenuation contrast on photoelectric absorption and Compton scattering changes with increasing Z of the material. For materials with Z ranging from 9 to 17, both effects contribute to the image formation (see Fig. 5.1(b)) [Berger *et al.* 2010].

Figure 5.3 shows attenuation (a) and phase (b) contrast axial slices reconstructed simultaneously from the same CT data set. The highest signal corresponds to aluminum, the lowest to PMMA. The quantitative values can be found in Table 5.3, and CNRs for selected material pairs are presented in Table 5.4.

The effective energy of the X-ray beam was determined by matching the measured and the calculated data for aluminum, which gives a strong signal in both contrast reconstructions. The minimum difference between measured and calculated values was found for 52.4 keV for phase contrast and 51.8 keV for attenuation, determined with 0.1 keV resolution. The higher effective energy is an effect of stronger filtering of the beam used to prevent beam hardening artifacts and resulting inaccuracies in the quantitative analysis. Because of the slightly different spectrum, which affects the system's fringe visibility and sensitivity, CNRs calculated for this phantom are not directly comparable to the CNRs of the low-Z phantom.

The mean values and associated standard deviations of the linear attenuation coefficient μ, refractive index decrement δ and electron density ρ_e are presented together with theoretical values in Table 5.3. Again, the experimental values of δ and ρ_e match the theoretical values within one standard deviation. The measured values of μ show a good agreement with the theoretical values with maximum discrepancy of 3%. The

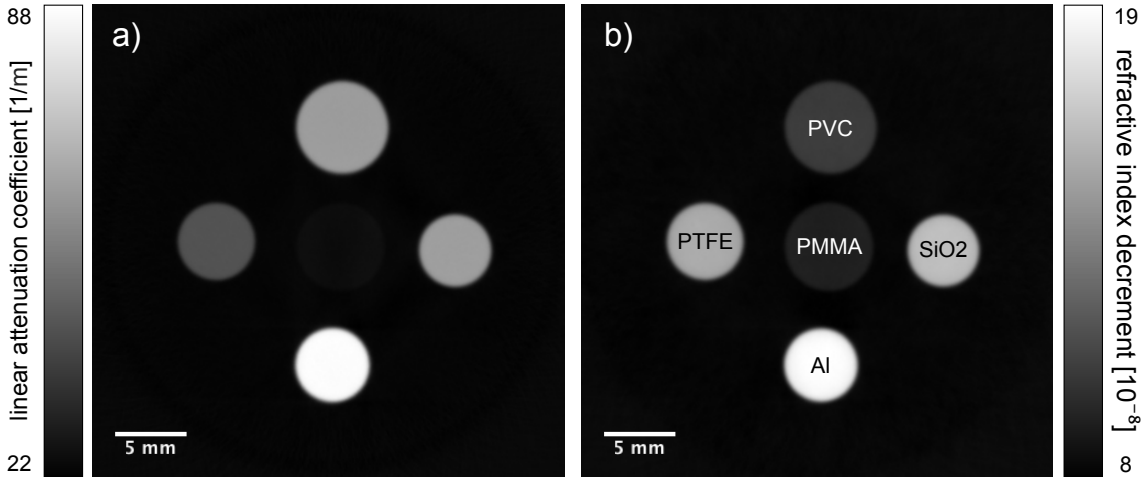

Figure 5.3: Comparison of axial slices from a tomographic reconstruction of the linear attenuation coefficient μ (a) and the refraction index decrement δ (b) distributions inside the high-Z phantom. At 51 keV mean energy, high-Z materials show again the complementarity of both signals. Figure adapted from [Sarapata *et al.* 2015b].

Table 5.3: Measured and theoretical (subscript th) attenuation coefficients μ, refraction index decrements δ and electron densities ρ_e for all the materials inside the high-Z phantom. This table was previously published in [Sarapata *et al.* 2015b].

Material	μ $[1/m]$	μ_{th} $[1/m]$	δ $[10^{-7}]$	δ_{th} $[10^{-7}]$	ρ_e $[10^{29}/m^3]$	ρ_e^{th} $[10^{29}/m^3]$
water	23.16 ± 0.18	22.72	0.839 ± 0.005	0.838	3.334 ± 0.02	3.339
PVC	60.82 ± 0.19	59.14	1.08 ± 0.03	1.08	4.304 ± 0.01	4.320
PTFE	45.49 ± 0.11	46.51	1.59 ± 0.06	1.60	6.350 ± 0.02	6.363
aluminum	89.29 ± 0.22	89.29	1.97 ± 0.04	1.97	7.848 ± 0.05	7.843
SiO_2	64.15 ± 0.14	65.83	1.69 ± 0.04	1.66	6.728 ± 0.04	6.620
PMMA	25.07 ± 0.43	24.68	0.969 ± 0.003	0.971	3.860 ± 0.01	3.868

analysis is not affected by the beam hardening because of the stronger beam filtering used.

The CNR changes depending on the respective pair of materials. For instance, between PVC and quartz a higher value of 64.8 in phase contrast compared to 14.0 in attenuation contrast could be found. The situation changes between aluminum and polytetrafluoroethylene (PTFE) for which attenuation contrast brings the ratio of 178.1 versus 28.8 in phase contrast. Contrast between PTFE and polyvinyl chloride (PVC) as well as water and PTFE is similar for both images. Clearly, complementary information looking at the phase- and attenuation-contrast images is accessible in the case of these materials with higher atomic numbers.

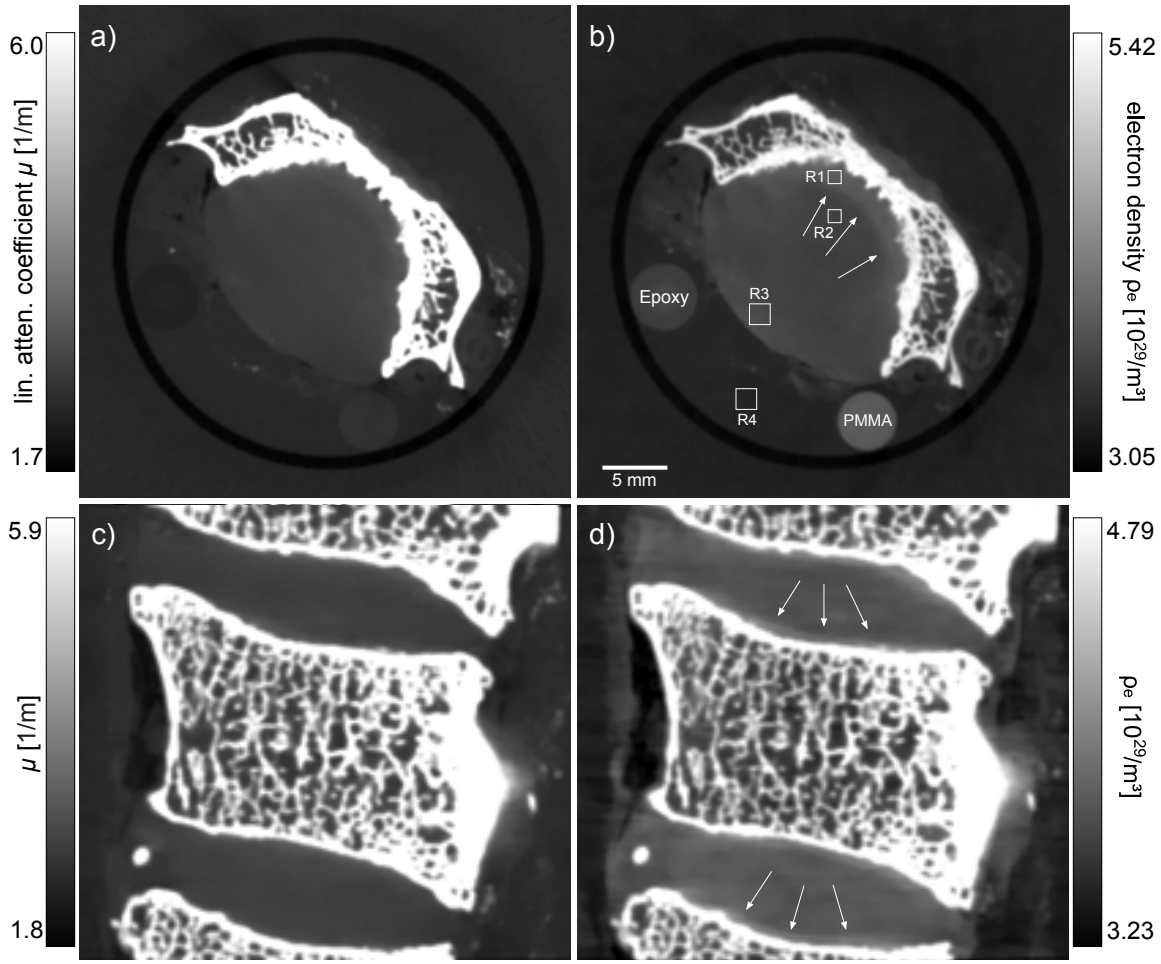

Figure 5.4: Tomographic reconstruction slices of the human cervical spine. Phase-contrast axial (b) and sagittal slices (d) show better visibility of the intervertebral discs than attenuation-contrast axial (a) and sagittal slices (c). Internal structure of the discs is visible and the clear boundary between the disc annulus and the nucleus pulposus can only be seen in the phase-contrast image (indicated by the arrows). Figure adapted from [Sarapata *et al.* 2015b].

Table 5.4: Contrast-to-noise ratios for phase contrast CNR_{phase} and attenuation contrast CNR_{abs} for selected sets of two materials inside the high-Z phantom. This table was previously published in [Sarapata *et al.* 2015b].

Material pair	CNR_{abs}	CNR_{phase}
water - PMMA	4.1	22.0
water - PTFE	102.4	96.1
water - PVC	144.3	41.8
PVC - SiO_2	14.0	64.8
PVC - aluminum	97.9	73.7
PTFE - aluminum	178.1	28.8
PTFE - PMMA	46.5	91.4
PTFE - PVC	69.5	76.9

5.3.3 Intervertebral discs

An intervertebral disc consists of two regions, i.e., the nucleus pulposus and the surrounding annulus fibrosus. The inner nucleus pulposus is a visco-elastic gel composed of a disordered network of type-II collagen fibrils. The outer annulus fibrosus is made of highly organized and densely packed type-I collagen whose fibers run parallel to each other [Matcher *et al.* 2004].

Figure 5.4 shows reconstruction slices of an intervertebral disc surrounded by vertebral bodies and various adjacent soft tissue types. Because of the high X-ray energy used, the bone does not obstruct the surrounding soft tissue with strong artifacts and its internal structure can be well reconstructed. Most significantly, a greatly increased visibility of the boundary between the disc annulus and nucleus pulposus inside the intervertebral disc (indicated by the arrows) is observed in the phase-contrast reconstruction (Fig. 5.4 (b) and (d)) compared to the conventional attenuation reconstruction (Fig. 5.4 (a) and (c)). This is a very interesting finding, as in general, this is a feature expected to be seen only in magnetic resonance imaging, not in X-ray CT.

Collagen is a low-Z material such that only small differences in its visibility between the two imaging contrasts at this photon energy can be assumed. However, as previously mentioned, it is very dense and exhibits a position-dependent degree of organization. Additionally, refraction-based imaging is sensitive to gradients of the line-integrated density, which are the largest near the boundaries. Thus, in most cases refraction has a contrast enhancing effect on edges between various tissues. The author believes that these are the reasons for the increased visibility of the boundaries inside the intervertebral disc in the phase-contrast reconstruction. In addition, the phase-contrast image contains more anatomical information than the attenuation image because of slightly increased contrast between the formalin and the soft tissue surrounding the bones.

The effective energy of the X-ray beam was determined by matching the measured and the calculated data for PMMA. The minimum difference between measured and

calculated values was found for 43.5 keV for phase contrast and 42.9 keV for attenuation.

In order to quantify the contrast enhancement between the phase and the attenuation reconstructions, four regions of interest (ROIs) were selected and the corresponding CNRs calculated. The ROI selection is indicated by squares in Fig. 5.4 (b). Between ROI1 and ROI2 (15x15 pixels) a higher value of 16.9 in phase contrast compared to 6.9 in attenuation contrast was found. Similarly, when comparing ROI3 and ROI4 (25x25 pixels), phase contrast yields a higher CNR than attenuation contrast (7.6 vs 3.4, respectively).

5.4 Conclusions

In conclusion, this chapter demonstrated the feasibility of quantitative high-energy X-ray phase-contrast CT using a Talbot-Lau interferometer with a polychromatic X-ray source and a 10 cm round analyzer grating. In particular, it was shown that such a system simultaneously provides quantitative information about the local 3D distribution of the linear attenuation coefficient μ, the refraction index decrement δ, and the electron density. As a result of the increased area of the analyzer grating, the first grating-based X-ray phase-contrast CT setup for samples up to 50 mm in width was build. The presented results show a big potential of the presented method for biomedical imaging, in particular for imaging of cartilage surrounded by bones.

Tomography scans of two phantoms were performed in order to quantitatively assess information on material properties and to investigate contrast dependence of phase and attenuation images for materials of various atomic numbers. In both cases, the refraction index decrements δ and electron densities ρ_e agree very well with the theoretical values within one standard deviation. The measured linear attenuation coefficients μ correspond well to theoretical values with a maximum discrepancy of 3%. The higher deviations may be associated with higher noise in the attenuation contrast due to the scattering and need further investigation. Since the μ values deviate stronger, it is harder to distinguish the materials in the attenuation-contrast image than in the phase-contrast image.

For low-Z materials, both attenuation- and phase-contrast images deliver the same information about various materials. Due to the domination of X-ray attenuation by Compton scattering, the same physical information (i.e. the electron density) is represented in both contrast modalities. However, the presented experimental setup has been successfully designed to provide enhanced phase-contrast images, with higher contrast-to-noise ratios than the attenuation-contrast results, which confirms the experimental findings from the monochromatic case by [Willner *et al.* 2013]. This contrast gain depends strongly on the specific grating interferometer and its optical parameters. Therefore, as the presented setup is in a research phase, it could be further improved by optimizing its parameters. The fringe visibility, which strongly dictates

the system's performance [Köhler *et al.* 2011, Raupach & Flohr 2011], could be more than doubled by increasing the height of the absorption grating structures or by inclining the gratings with respect to the axis of the X-ray beam [Stutman & Finkenthal 2012]. Moreover, filtering the parts of the spectrum which reduce the overall fringe visibility would increase the system capabilities. Only when optimized for the best optical performance, i.e. achieving both, high fringe visibility and high angular sensitivity, clinically dose-compatible measurements can be performed as it is shown in Chapter 7.

It might be challenging for the presented system at its design energy to compete with gbPC-CT systems operating with lower X-ray energies, because of their higher sensitivity and thus very high soft-tissue contrast. However, the very high sensitivity of such systems can sometimes prevent them from being able to measure biomedical samples containing calcifications, bones, etc. Tomography reconstructions of such samples result in strong strike artifacts obstructing the view. In such cases, high-energy gbPC-CT can fill the gap by providing satisfactory soft-tissue contrast and localization of calcifications and other high-Z materials embedded in the tissue, which oftentimes are first indications of an evolving disease.

Despite the fact that it still remains challenging to develop a high-energy grating interferometer with a broad polychromatic source yielding satisfactory optical performance, the presented results prove that improved image quality for phase contrast as compared to attenuation contrast can be obtained at high photon energy. Finally, the demonstration of quantitative high-energy grating-based X-ray phase-contrast CT implemented at a conventional X-ray source, thus without a need for a limited and often expensive access to synchrotron-radiation facilities, opens the technique to a broad range of laboratory-based applications in materials science, fabrication of x-ray optics, and biomedical imaging.

The most promising, but not yet fully explored, field for the presented effective X-ray energy around 45 keV are materials science applications. High penetration depth of such photons allows investigation of dense and large objects. As seen from the results of the high-Z phantom, the possibility to simultaneously access various information on material composition provides added value over attenuation-only-based images. The author took advantage of that fact to provide multi-contrast microtomography of concrete, which is presented in Chapter 8.

Chapter 6

Design of dedicated phase-contrast phantoms

Contents

6.1 Introduction 61

6.2 Breast tissue-substitute materials 63

6.2.1 Electron density of breast tissue in literature 63

6.2.2 Results and discussions 66

6.2.3 Summary 66

6.3 CT phantoms for image quality assesment 67

6.3.1 Quantitative phantom 68

6.3.2 Low-contrast phantom 68

6.3.3 Results and discussions 70

6.4 Conclusions 73

This chapter presents designs and experimental evaluation of proof-of-concept, dedicated X-ray phase-contrast phantoms. A short description of conventional phantoms for attenuation-based X-ray imaging is given and the need for phantoms designed specifically for phase-contrast imaging is explained. Thanks to the results of quantitative measurements presented in Chapter 4, polymer plastic materials equivalent in their refraction properties to breast tissues were found. In collaboration with Quality Assurance in Radiology and Medicine GmbH (QRM, Möhrendorf, Germany), an image-quality and a low-contrast phantoms dedicated for use in tomography were designed and manufactured. Imaging results of both phantom are presented, and their benefits for characterization of PC-CT systems are reported. The presented phase-contrast phantoms are the first of many more to be developed as valuable tools for quality-control testing of phase-sensitive X-ray imaging systems.

6.1 Introduction

Imaging phantoms are specifically designed objects that are used in the field of medical imaging to analyze, compare and optimize the performance of various imaging

systems. Because of harmful effects of ionizing radiation on human body, phantoms are oftentimes used in X-ray imaging since its beginnings. Their easy availability and better consistency of the results than exploiting a living tissue are the reasons for their extensive use in the field of medical imaging.

Phantom's design and its composition depends strongly on the aspect of the imaging system that needs to be evaluated. For instance, phantoms designed to test the spatial resolution capabilities are not necessarily composed of materials similar in composition to a human tissue. On the other hand, dosimetric phantoms for evaluation of the dose delivered to a person during radiation therapy treatments are made of tissue-substitute materials.

There exist a plethora of phantoms designed for X-ray imaging, both radiography and tomography mode. Depending on the task various designs are available, ranging from line-pair phantoms for resolution testing to tissue-equivalent phantoms used to test the imaging system's ability to correctly image soft tissues.

All the commercially available phantoms so far have been designed for attenuation-based imaging. In conventional CT the measured value is the attenuation caused by the object, represented by its Hounsfield (HU) value. Each voxel (equivalent of a pixel in 3D) of a CT image represents a measure of the respective attenuation caused by the scanned object. That is why phantom materials are chosen based on their X-ray attenuation properties, that is their attenuation coefficient values. However, in phase-contrast CT voxels represent phase-shifting / refracting properties of the object. As these two contrast modalities operate on different physical principles, a phantom designed for use in an attenuation-contrast mode may not be suitable for phase-contrast imaging.

The materials within phantoms are often intended to simulate human tissue. Thus, an important part of a phantom creation is tissue equivalence of the used materials. There exist various properties that can be used to measure the tissue equivalence of a phantom. For example to assess that, one could use the physical density and effective atomic number. These parameters accurately describe the physical properties of the material in question, but do little to describe how the material is going to influence the X-ray beam. The most extensively used and generally accepted parameters for evaluation of radiation properties of a tissue-equivalent material are the linear attenuation coefficient μ and the mass energy-absorption coefficient μ_e/ρ. The former describes the fraction of a beam of X-rays that is attenuated (absorbed or scattered), while the latter is a measure of how much energy is locally deposited in the specific tissue. As X-ray photons interact with the electron cloud, a fundamental parameter that provides more insight into how a material affects an X-ray beam is the electron density. Unfortunately, only selected tissue-equivalent materials are formulated with consideration for electron density. The ones which do are expected to be well suited for phase-contrast imaging.

Ideally, a phantom material will accurately mimic as many of the aforementioned

properties of the tissue that is being simulated. However, this can be very difficult to achieve, thus simulating the radiological properties of the tissue of interest should be of a primary aim. Keeping in mind that radiological properties will change depending on the contrast modality being investigated.

6.2 Breast tissue-substitute materials

Phantoms used in quality assurance and calibration procedures of X-ray imaging system should respond in a similar manner to how human tissues would act in that specific imaging modality. With the introduction of phase contrast to the X-ray world, new materials have to be designed or existing ones tested for their suitability. Having the possibility to experimentally access the electron densities of soft tissues and plastic materials as described in Chapter 3 and 5, tissue-substitute materials that have similar "phase-shifting" properties as various human tissue types can be found.

One of the most promising clinical applications of X-ray phase-contrast imaging is mammography. There has been several publications trying to assess the possible advantages of phase contrast imaging for breast tumor detection. Adipose, fibroglandular, and tumor tissues were also characterized for their electron density by [Willner *et al.* 2014]. In this chapter, materials that could be used in phase-contrast phantoms as tissue substitutes are suggested based on the similarity of electron density values.

The majority of existing tissue-substitute materials are made of hardened epoxy-based resins. Because the density of the hardened resins exceed these found in biological tissues, manufacturers use low density microspheres as additives. These powders are made up of hollow, gas-filled spheres in a size range of a few to tens of micrometers and are added to the basic resin systems [White *et al.* 1977a]. They can potentially create (ultra)small-angle scattering (USAXS) when used in dedicated phase-contrast phantoms. Since strong USAXS reduces the fringe visibility of the "phase-stepping" curve these materials can possibly have a negative effect on the overall quality of a phantom. To evaluate if the epoxy resin-based fabrication technique could be employed for creation of breast tissue-substitute materials, three water-equivalent, two bone- and two tissue-equivalent materials were measured in the special geometry presented in Chapter 4.

6.2.1 Electron density of breast tissue in literature

In order to manufacture / find materials with electron densities matching these of human tissues, the latter has to be known. Table 6.1 presents a comparison of experimental electron density values for breast tissues found in the literature. Compton scattering is the most popular technique used for electron density characterization of biological tissues. However, it produces results which vary quite strongly from one

publication to another. These discrepancies can be explained by different preparation methods that were used to fix the tissue before the measurements. Compton scattering does not provide images with spatial resolution, it requires various correction factors to be applied and the results reflect the average of volumes with side lengths of a few millimeters. On the other hand, gbPC-CT provides high spatial resolution images, which enable a clear distinction between certain tissue types, e.g. fibroglandular and adipose tissue. Thus, the author strongly believes that results obtained with gbPC-CT should be of the main interest when looking for a tissue substitute material of breast tissue.

Table 6.1: Comparison of experimental electron density values of breast tissue types found in the literature.

		Al-Bahri (1998)	**Ryan et al. (2005)**	**Antoniassi et al. (2010)**	**Antoniassi et al. (2012)**	**ICRU 44 report**	**Willner et al. (2014)**
	Method	Compton scattering				theoretial	PC-CT
	Preparation	freeze-drying	frosted	fresh	formalin		formalin
Tissue type	Adipose	3.46 (0.013)	3.24 (0.14)	3.24 (0.16)	3.21 (0.14)	3.18	3.11 (0.12)
	Fibroglandular	3.48 (0.013)	-	3.53 (0.29)	-	3.39	3.56 (0.33)
	Fibroadenoma (benign)	-	3.31 (0.14)	3.47 (0.12)	3.39 (0.17)	-	-
	Carcinoma (malignant)	3.56 (0.013)	3.53 (0.15)	3.60 (0.17)	3.48 (0.15)	-	3.50 (0.21)
	Fibrocystic change	-	3.65 (0.15)	-	-	-	-

6.2.2 Results and discussions

Measured electron density values of plastic materials provided by the QRM were compared with results from [Willner *et al.* 2014] to find the closest match. The materials with the smallest difference in electron densities are suggested as a good approximation of the specific tissue (see Table 6.2).

Table 6.2: Plastic materials suggested as the most fitting breast-tissue substitutes.

tissue type	electron denisty		material of similar	$\rho_e(material)/$
	Willner et al.	ICRU 44	el. density	$\rho_e(tissue)$
adipose	3.12 (0.12)	3.18	PP or PE	0.99 or 1.05
fibroglandular	3.56 (0.33)	-	EP 5	1.01
tumor	3.50 (0.21)	-	PUR 2	1.02
mammary gland	-	3.39	Polyamide/Nylon	0.97

Thanks to the feasibility of an accurate measurement of electron densities with gbPC-CT, further tissue-equivalent materials for other organs and tissue types can be found. Moreover, more materials have to be quantitatively characterized to find the closest match. Possibly, new casting techniques need to be developed and tested to find a reliable method providing plastics with a wide range and easily variable electron densities.

Figure 6.1 shows differential phase-contrast images of two rods. One was made out of a hardened epoxy resin (a), while the other out of an epoxy resin mixed with calcium carbonate powder (b). One can see that the added microstructures, which are too small to be spatially resolved in the images, produce however strong USAXS visible as a strong dark-field signal. Strong scattering causes a decoherence of the wavefront, which makes the measurement of the refraction angles less precise. It is seen as an increased uncertainty in the mean phase shift extracted from the images and a non-flat horizontal line profile.

Mixing microspheres and micrometer-size powders with epoxy resins is a common technique to produce materials for X-ray phantoms. Thus, when looking for a material suitable for phantoms dedicated for phase-contrast imaging, one should find an alternative.

6.2.3 Summary

The ICRU 44 report suggests the use of a breast-tissue equivalent BR-12 material originally developed by [White *et al.* 1977b] to simulate a tissue composition of 50 % fibroglandular tissue and 50 % adipose tissue (i.e., 50 % glandularity). Because it is an epoxy based with phenolic microspheres and calcium carbonate powder it is not suggested for use in phase-contrast imaging as it will degrade image quality of the phase-contrast channel due to existence of USAXS. For that reason, materials commonly used in attenuation-based imaging such as BR10 or BR12 [Goldstone 1990]

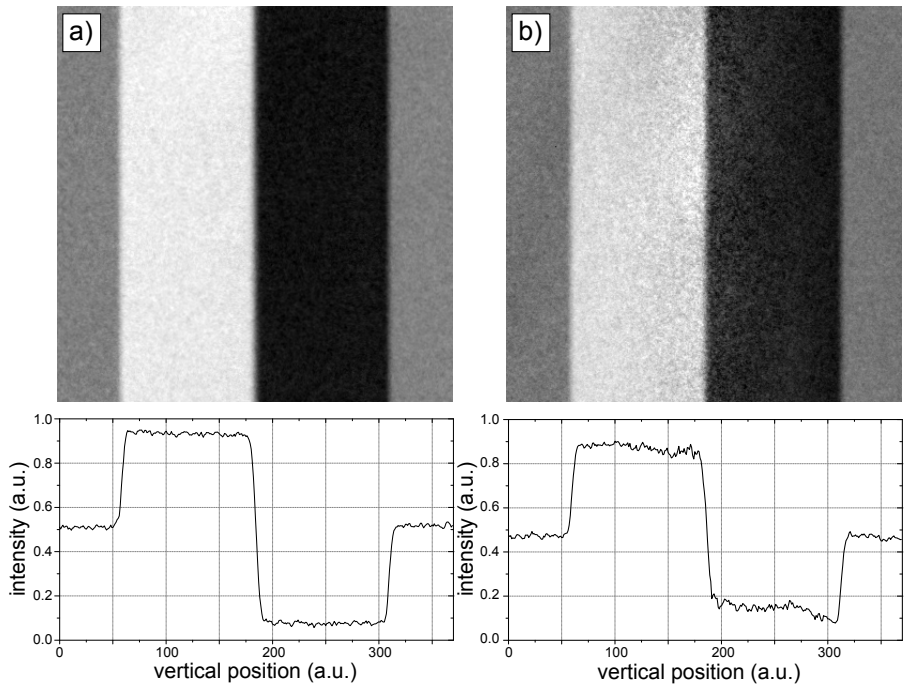

Figure 6.1: Differential phase-contrast projections and line profiles of two different rods: (a) homogenous epoxy resin, (b) epoxy resin mixed with a calcium carbonate powder.

containing microspheres or powders should not be used. Another reason that BR-12 is not an ideal material is that the "50-50" breast is not a representative model of the breast composition. The mean composition of the breast, expressed as percent fibroglandular tissue (including the skin) is lower than 50% and approximately 19 % [Yaffe *et al.* 2009].

Finally, when looking for proper tissue-equivalent substitutes for phase-contrast imaging, only existing materials, which are formulated with consideration for electron density, should be chosen, or new ones produced. Phantoms used for dosimetry and dose distribution calculations satisfy this requirement as they must have the same effective atomic number and the same electron density as those of soft tissue.

6.3 CT phantoms for image quality assesment

There are various phantoms specifically designed for testing image quality of X-ray imaging systems, both in radiography and tomography mode. For that purpose, tissue equivalence described above is not a crucial parameter. Most phantoms provide an assessment of image quality by testing system's resolution, dose efficiency, low-contrast detectability, etc.

Here, two phantoms to access image quality of the gbPC-CT system are presented: a first phantom to test the accuracy of quantitativeness, and a second to test the minimum detectable contrast and its dependance on the radiation dose.

6.3.1 Quantitative phantom

A phantom is a very useful tool to characterize the experimental imaging system and investigate if all the steps of the processing chain work properly. It is a task usually hard to achieve with a "real" sample with complicated geometry and most of the time unknown exact composition. Because of a phantom's stable design, it can be scanned multiple times at different radiation dose levels / total exposure times and even different setups to compare their imaging capabilities. Correctness of the CT reconstruction processing chain, detector response, noise propagation, etc. can be easily tested using a phantom as the object being imaged.

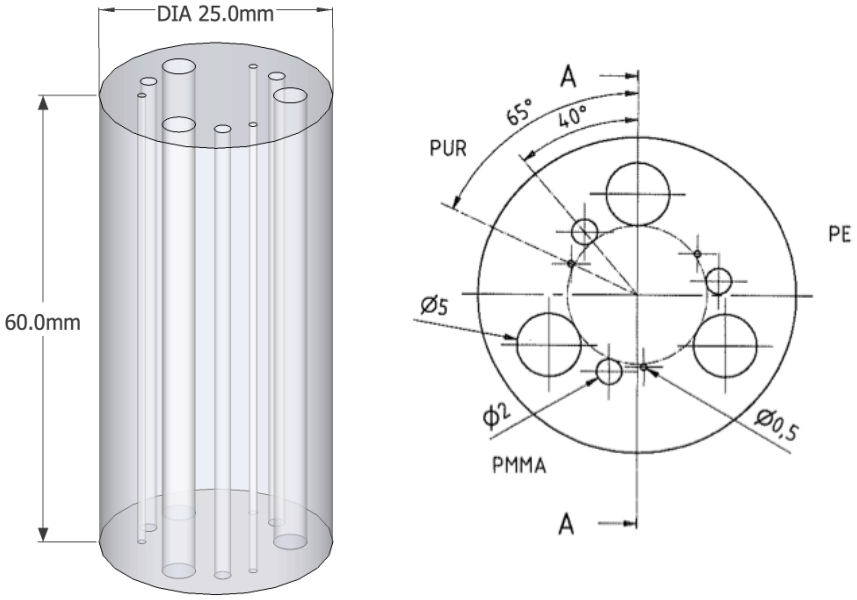

Figure 6.2: Schematic drawing of a phantom designed to test characterize experimental setups. Image courtesy of QRM GmbH.

A phantom for tomography mode was designed by the author and manufactured by QRM GmbH. It is composed of three inserts of various sizes and made of materials of various electron densities to mimic objects creating different image contrast levels. The inserts are placed perpendicular to the tomography axis in a cylindrical base made of epoxy resin. The phantom's schematic can be seen in Figure 6.2.

6.3.2 Low-contrast phantom

An important attribute of an imaging system is its capability to discern object with very similar attenuation or refraction properties. In attenuation-based imaging, so-called low-contrast phantoms exist to test the limits of the imaging systems in their ability to distinguish soft tissues with small differences in densities.

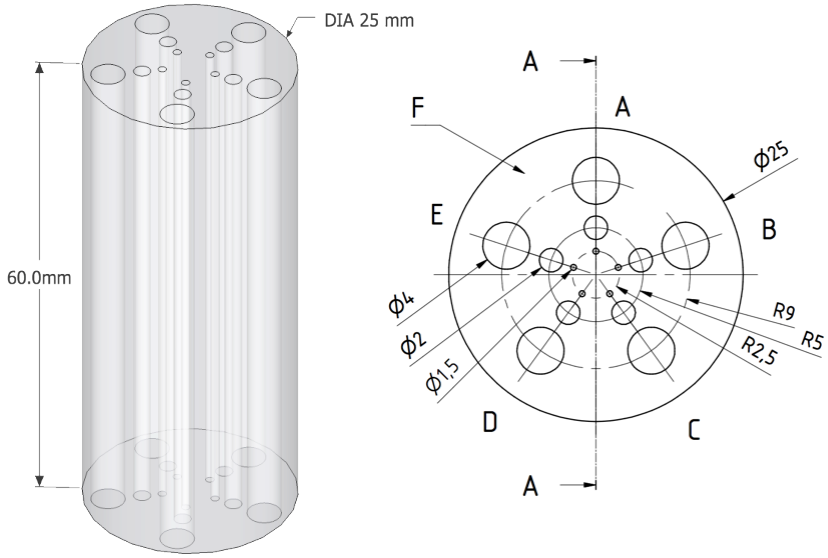

Figure 6.3: Schematic drawing of a low-contrast phantom designed to test the smallest electron density differences. Image courtesy of QRM GmbH.

In grating-based phase-contrast imaging, detectability of low-contrast features is not only limited by the total number of photons, but also by the geometrical parameters of the interferometer. The lowest detectable angle is defined as:

$$\alpha_{min} = \frac{p_2}{2\pi d}\sigma_{\Delta\varphi} \ , \tag{6.1}$$

where p_2 is the period of the analyzer grating, d is the distance between the gratings G1 and G2, and $\sigma_{\Delta\varphi}$ is a standard deviation of the measured differential phase-contrast signal, which is further related to the fringe visibility V and the total number of counts N_{tot} by

$$\sigma_{\Delta\varphi} = \frac{\sqrt{2}}{V\sqrt{N_{tot}}} \ . \tag{6.2}$$

The uncertainty in the measurement of $\Delta\varphi$ is further related to the detector quantum noise and the influence of the sample as [Revol *et al.* 2010]:

$$\sigma^2_{\Delta\varphi,det} = \frac{2}{V^2} \cdot \frac{f_1}{N_{ps} \cdot a_0} \cdot \left(1 + \frac{1}{\overline{T} \cdot \overline{D}^2}\right), \tag{6.3}$$

where V is the mean fringe visibility, N_{ps} is the number of phase steps, a_0 is the mean detector counts in a sample-free area, f_1 is the system-dependent conversion factor related to the detector gain, $\overline{T}$ is the loss of photons caused by the transmission through the sample, and $\overline{D}$ is the reduction of the fringe visibility caused by the scattering (dark-field signal) of the sample.

Other possible sources of noise exist; one of them being the system noise caused for instance by the so-called dark current of the detector or spatial non-uniformities of the gratings. They all can additionally contribute to the degradation of the image quality. A more in-depth analysis of that matter can be found in [Revol *et al.* 2010].

The lowest detectable angle corresponds to the lowest detectability of electron density in the tomography mode. It depends on many parameters, such as the spatial resolution, the number of tomography projections, the distance between the sample and the phase grating G1, and many more. A figure of merit commonly used to estimate the sensitivity of electron density measurements is the standard deviation of the values in a homogenous region of the reconstructed volume.

A low-contrast phantom dedicated for PC-CT systems was designed by the author and manufactured by QRM GmbH. By precisely controlling materials' parameters, a phantom with inserts of electron densities varying by only a few percent was made. The phantom's schematic can be seen in Figure 6.3 and its exact composition in Table 6.3.

Table 6.3: Composition of the low-contrast phantom.

#	material	density [g/cm^3]	ρ_e^{th} [10^{29}/m^3]	% diff to the base
A	epoxy	1.139	3.726	0.89
B	epoxy	1.125	3.681	-0.35
C	epoxy	1.116	3.651	-1.15
D	polyurethane	1.139	3.737	1.16
E	polyurethane	1.082	3.550	-3.90
F	epoxy	1.129	3.694	-

6.3.3 Results and discussions

The experimental results of the phantoms were obtained with the high-energy setup presented in Chapter 3.5. Data acquisition and analysis were the same as in Section 5.2.4. Parameters that varied during the measurements are specified in Table 6.4.

Table 6.4: Experimental setup parameters

	quantitative phantom	low-contrast phantom
number of phase steps	8	
number of projections	1200	
exposure time [s]	1	
tube peak voltage [kVp]	65	
tube current [mA]	27.5	1.5
beam filtering	2 mm of Al	
measured in	water	air

Image-quality phantom: Figure 6.4 shows phase-contrast tomography reconstructions of electron density distribution inside the phantom. The reconstruction quality with regards to axial slice thickness is examined for a selection of three averaging parameters of 1 (a), 5 (b), 40 (c). One can see suppression of image noise with increasing number of averaged slices. Please note that averaging of the adjacent slices does not result in as good image quality gain as the corresponding increase in total exposure time. Influence of quantum noise on image quality in phase-contrast tomography is intrinsically different than in attenuation-based tomography [Köhler *et al.* 2011]. It is actually expected that increasing slice thickness improves the image quality (suppresses the noise) more effectively in attenuation-contrast imaging than in phase-contrast imaging.

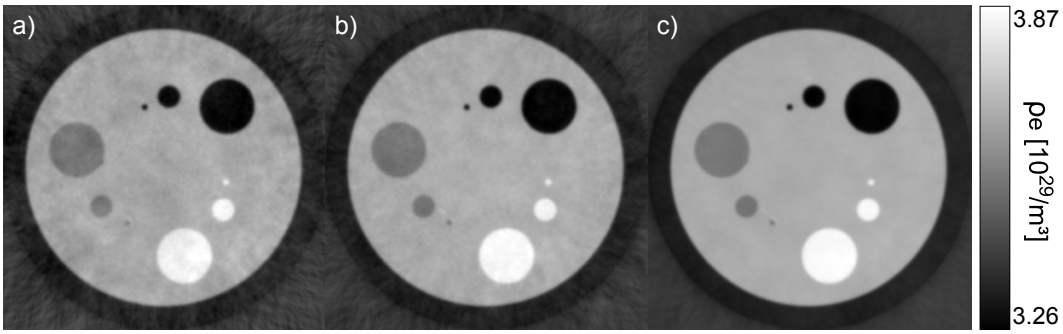

Figure 6.4: Phase-contrast tomography reconstructions of the quantitative phantom with varying slice thickness. One (a), five (b), and 40 (c) adjacent axial slices were averaged in order to reduce image noise.

Table 6.5: Measured and theoretical (superscript th) electron densities ρ_e of all the quantitative phantom's inserts. Differences between the measured and theoretical values are given and they are all bellow 1% proving the quantitative correctness of the experimental setup.

Material	density [g/cm^3]	ρ_e [10^{29}/m^3]	ρ_e^{th} [10^{29}/m^3]	difference [%]
PE	0.953	3.296 ± 0.18	3.276	0.62
PMMA	1.186	3.856 ± 0.19	3.855	0.02
PUR	1.080	3.559 ± 0.11	3.543	0.45
base (EP)	1.130	3.695 ± 0.22	3.697	0.05

Solid plastic phantoms should be used if possible over mixed-liquid phantoms because of their exact and permanent composition. A phantom made of various liquids (like the one used in Section 5.3.1) is more prone to inadequate composition because of the mixing process and because concentration of the liquids within could change with time for instance due to evaporation. Additionally, geometry of liquid phantoms is restricted such that complex or very small shapes are unfeasible.

Low-contrast phantom: The experimental results of this phantom, in contrast to the previous one, were not obtained using the high-power tube described in Section 3.5 due to its malfunction. The phantom was measured at a significantly lower photon count using a micro-focus low-power X-ray tube running with the current of 1.5 mA. Therefore, results of this phantom are not comparable with results of the image-quality phantom, or with the results presented in Chapter 5. However, they show a rough estimate of a low-dose performance of the setup and the low-frequency noise behavior in phase-contrast CT reconstructions, which was in details explained for example in [Köhler *et al.* 2011].

Figure 6.5 shows phase-contrast reconstruction slices of the low-contrast phantom. In a single-slice reconstruction, only one of the inserts is visible, i.e. polyurethane with almost 4 % difference in electron density to the base material. Averaging of the adjacent slices reveals more inserts. Please note that effect of averaging of the adjacent slices on the image noise is not equal to the corresponding increase of total number of photons by means of increasing the radiation dose.

One can see that the presented high-energy setup used to obtain this data set can reveal objects with difference in electron density of not less than 3 % at reasonable exposure times with the X-ray tube running at the peak voltage of 65 kVp and the current of 1.5 mA.

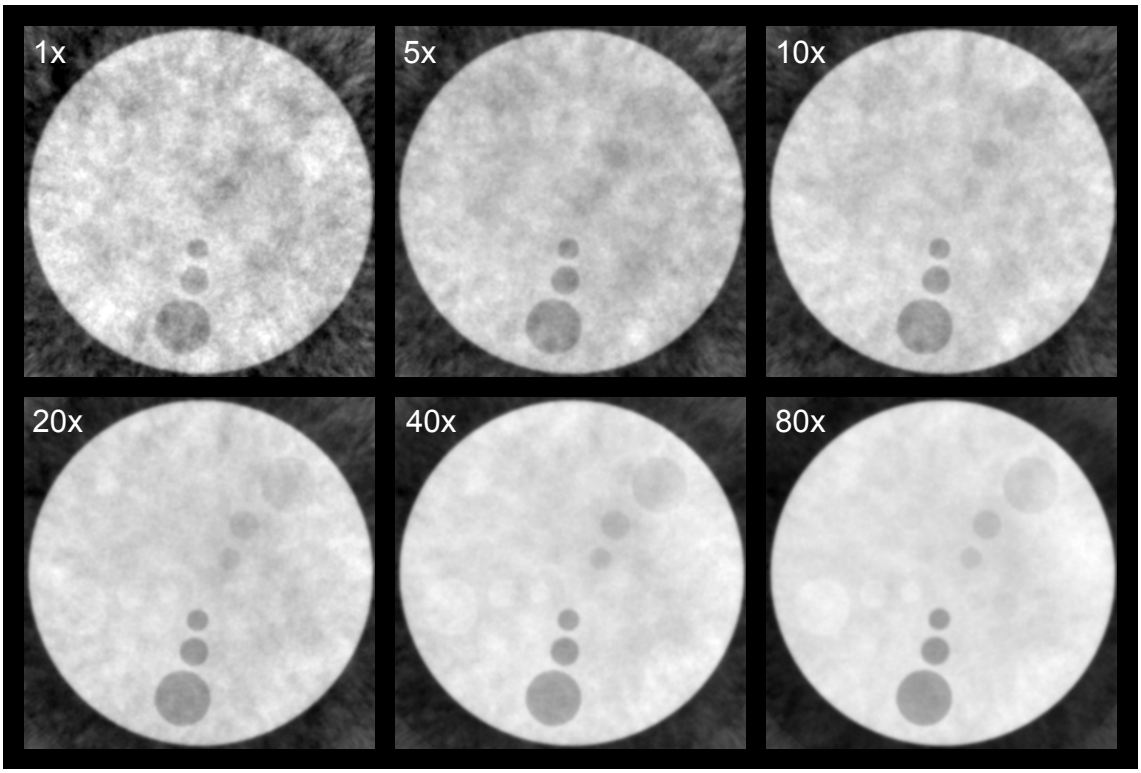

Figure 6.5: Phase-contrast tomography reconstructions of the low-contrast phantom. Various numbers of adjacent axial slices (indicated by the digits in the upper left corners) were averaged in order to reduce image noise.

6.4 Conclusions

In summary, this chapter presented first steps and considerations towards the creation of dedicated phase-contrast phantoms.

Plastic materials that could be well suited to mimic electron density distribution of a breast tissue were chosen based on the experimental results obtained with the grating interferometer setup in a projection mode described in Chapter 4. An important finding was made regarding the commonly used BR10 or BR12 materials for breast tissue equivalence. They should be avoided when choosing materials for mammography phase-contrast phantoms as they contain scattering particles and can potentially cause signal degradation in the phase-contrast mode. More tissue-equivalent materials can be chosen if the electron density of the corresponding tissue type is known.

Two dedicated PC-CT phantoms made of durable plastics were designed, manufactured and experimentally tested. Using the quantitative phantom, the high-energy experimental setup was characterized for its accuracy and precision of the quantitative values. The setup proved to provide very accurate measurements of the electron density for the materials of choice, with differences between the measured and theoretical values below 1 %.

The low-contrast phantom was employed to experimentally access the setup detectability of object with difference in electron density of a few percent. At commonly used scanning parameters used with an X-ray tube running at a peak voltage of 65 kVp and current of 1.5 mA, the setup is able to distinguish objects with an electron density difference of not less than 3 %.

Epoxy-based resins are a good choice for phase-contrast phantom materials as their mass density, thus electron density, can be controlled precisely over a small range of densities. However, they cannot be used for tissue-equivalence as in general their density is higher, with few exceptions, than various soft tissues within the human body. In attenuation-based imaging this discrepancy is accommodated for by addition of low density powders, microspheres, or micro-bubbles. These additives, however, should not be used in phase-contrast phantoms for reasons discussed above.

With the use of the presented phantoms, imaging protocols and standard scan parameters can be optimized to ensure optimum utilization of various experimental setups.

Chapter 7
Towards dose-relevant CT

Contents

7.1 Introduction 75
7.2 Materials and methods 76
7.2.1 Experimental setup 76
7.2.2 Image acquisition and processing 77
7.2.3 Samples 80
7.2.4 Experiments 80
7.2.5 Monte Carlo estimation of dose 81
7.3 Results and discussions 81
7.3.1 Fringe visibility 81
7.3.2 Dose estimation by computer simulation 84
7.3.3 Comparison between the two phase-stepping methods 84
7.3.4 High- versus low-visibility system comparison 85
7.3.5 Soft tissue phantom at different exposure times 86
7.3.6 Soft tissue phantom filled with water 88
7.4 Conclusions 90

This chapter describes initial progress towards a clinically compatible X-ray phase-contrast CT system, using glancing-angle X-ray grating interferometry to provide high-contrast soft-tissue images at, estimated by computer simulation, dose levels comparable to conventional attenuation-based CT. High-fringe-visibility interferometer was realized by a simple design change, which increased the opacity of the absorption grating and successively provided superior in the image quality, phase-contrast reconstructions.

Phase-contrast CT scans of a joint phantom and of soft tissues were performed in order to answer several important questions from a clinical setup point of view. A comparison between high and low fringe visibility systems is presented. The standard phase-stepping method is compared with sliding-window interlaced scanning. Using estimated dose values obtained with a Monte-Carlo simulation code the dependence of the phase-image contrast on exposure time and dose is studied.

Using a glancing-angle interferometer at high X-ray energy (approximately 45 keV mean value) in combination with a conventional X-ray tube, a fringe visibility value of ∼50 % was achieved. The high fringe visibility is shown to be an indispensable parameter for a potential clinical scanner. Sliding window interlaced scanning proved to have higher SNRs and CNRs in a region of interest and to also be a crucial part of a low dose CT system. Phase-contrast images of a soft tissue phantom at exposures in the range typical for absorption-based CT of musculoskeletal extremities were obtained. Assuming a human knee as the CT target, good soft tissue phase contrast could be obtained at an estimated absorbed dose level around 8 mGy, similar to conventional CT.

Phase-contrast CT with glancing-angle interferometers provides improved soft tissue contrast over absorption-CT even at clinically compatible dose levels (estimated by a Monte-Carlo computer simulation). Further steps in image processing, data reconstruction and spectral matching could make the technique fully clinically compatible. Nevertheless, due to its increased scan time and complexity the technique should be thought of not as replacing, but as complimentary to conventional CT, to be used in specific applications.

The majority of results presented in this chapter were published in:
A. Sarapata, JW. Stayman, M. Finkenthal, JH. Siewerdsen, F. Pfeiffer, D. Stutman, "High energy X-ray phase contrast CT using glancing-angle grating interferometers," Medical Physics **41**, 021904 (2014).

7.1 Introduction

Grating-based X-ray phase-contrast CT (gbPC-CT) has the potential to combine the high soft tissue contrast comparable to MRI with the high spatial resolution and penetration depth of X-rays. However, if clinical applications are of interest, the radiation dose used to obtain the images has to be kept equal or lower than the accepted limits [Kalra *et al.* 2004].

In the recent years there has been a lot of interest in the gbPC-CT technique from the medical community in the hope for improved cancer detectability in, for instance, the breast [Grandl *et al.* 2014], liver [Noël *et al.* 2013], brain [Pfeiffer *et al.* 2007a] or pancreas [Tapfer *et al.* 2013], and for improved imaging of cartilage [Stutman *et al.* 2011], or of plaque [Hetterich *et al.* 2013]. While the experiments, both using conventional tubes and synchrotron X-rays, demonstrated improved soft tissue contrast, the dose delivered to the sample (and eventually to a patient) that is necessary to obtain this additional information still remains a big concern [Raupach & Flohr 2012]. Published experiments have so far routinely exceeded the dose limits acceptable in conventional CT by up to a few orders of magnitude [Grandl *et al.* 2013, Pfeiffer *et al.* 2013, Bravin *et al.* 2012]. The question yet to be answered is thus whether X-ray phase con-

trast imaging using grating interferometer will still outshine absorption based imaging when used with a considerably lower dose, closer to clinical acceptable values.

The optical performance of the Talbot-Lau interferometer is described by two main parameters: the interferometric fringe visibility (V), also known simply as visibility, and the angular sensitivity (S). The visibility characterizes the amplitude or contrast of the intensity modulation in the interference pattern, and is defined as in Eq. 3.21. The angular sensitivity defines the smallest refraction angle detectable by the system. Theoretical analysis predicts that the ratio between the NEQ (noise equivalent quanta) in DPC to that in absorption-CT increases proportionally to the product $S^2 * V^2$ [Tang *et al.* 2011]. The angular sensitivity is determined by the ratio between the distance between G1-G2 and the G1 period, divided by the magnification of the setup. Thus, it is practically limited by the feasible grating period ($\geq$ few µm) and by the clinically compatible scanner length ($\leq$ 1.5 m approximately). Thus, one of the most promising ways to improve image quality at a given dose is therefore to increase the fringe visibility of the system.

In addition, most clinical CT applications require the use of photon energies above 40 keV to be able to penetrate thick human body parts and a reasonable scan time. While the latter could be solved easily by using a high-power source like a rotating anode X-ray tube, working with a grating interferometer at high X-ray energies is not trivial. The constraining factor preventing "conventional" gbPC-CT systems from operating at high energies is limitations in the absorption grating fabrication process; the gold grating bars cannot easily be made thick enough to be opaque to X-rays, especially for small period gratings. This causes radiation to "leak" through the gratings and drastically reduces the visibility of the interferometer. Because of this limitation gbPC-CT could not be yet made to work under optimum conditions at energies of clinical interest. To overcome this limitation [Stutman & Finkenthal 2012] suggested a simple design change in the interferometer, in which the gratings are tilted along the direction of the source-detector axis, thereby presenting an effectively increased grating thickness and making it possible to operate at energies $>$ 40 keV with high visibility. By exploiting this idea, this chapter discusses the first steps towards clinically compatible X-ray phase contrast CT, consisting in achieving high fringe visibility at a diagnostic relevant energy (approximately 45 keV mean spectral value) and lowering the dose (estimated by a Monte-Carlo computer simulation) to levels approaching or similar to conventional attenuation-CT.

7.2 Materials and methods

7.2.1 Experimental setup

The experiments presented in this chapter were carried out at the Henry A. Rowland Department of Physics & Astronomy of Johns Hopkins University (Baltimore, USA)

under the co-supervision of Dr. Dan Stutman.

The gratings were produced by microworks GmbH, Germany, had 5.4 μm pitch and were used in the 3rd fractional Talbot order. The nominal thickness of gold for the source grating (G0) and the analyzer grating (G2) was 100 μm. The phase grating (G1) varied depending on the configuration used (more details to follow). The whole setup length was kept at approximately 1.7 m.

To compare high-energy PC-CT with low and with high fringe visibility, the setup was used in two different configurations: at a normal incidence angle (see Fig. 7.1(a)) and inclined at an angle $\alpha = 23.5°$ (see Fig. 7.1(b)), creating a so-called glancing angle interferometer (GAI). Inclination of the gratings increases their effective thickness by a factor of $1/sin(\alpha)$, thus increasing their X-ray absorption and the fringe visibility. Due to the same effect of grating thickness variation with tilting, the nominal height of nickel structures in the phase grating is smaller for the GAI than the normal incidence interferometer [Donath *et al.* 2009b]. In the experiment, two different phase gratings were used, producing the same π-phase shift at roughly 45 keV X-ray energy. For the GAI a Ni phase grating with bars of 7 μm was used, while the normal incidence interferometer used an Au phase grating with 8.5 μm thick bars. The distances between the gratings were kept the same in both setups in order not to change the angular sensitivity.

A micro-focus tungsten target X-ray tube with 60 μm spot size was used, with a current of 1 mA and voltage of 65 kVp. To produce an X-ray spectrum with a mean energy of 45 keV the tube emission was filtered by 40 mm of water, 1.5 mm of Al and 0.125 mm of Cu. As shown in Ref. 17, high fringe visibility can be achieved at even higher X-ray energy by increasing the inclination angle of the gratings. However, the author limited the glancing angle to 23.5° because the current setup suffers from beam vignetting due to narrowing of the grating openings away from the center of the grating. In a practical scanner the vignetting can be eliminated using a slightly different grating design, as discussed in [Stutman *et al.* 2013]. For the experiments, the author chose an inclination angle, which gave a reasonable balance between visibility and vignetting. The detector consisted of a lens coupled cooled CCD detector with pixel size of 9 μm, used in a 10x10 binning mode, and placed directly behind the analyzer grating (G2). Using a high efficiency CsI scintillator screen and f/1 relay lens resulted in a quantum gain of more than 10 CCD electrons per X-ray, corresponding to a high DQE of ~ 0.8 [Wu *et al.* 2003]. The effective spatial resolution at the sample position was ∼78μm (taking both magnification and source size factors into account).

7.2.2 Image acquisition and processing

In order to separate the attenuation, refraction (phase) and ultra-small scattering components in the raw CT projection images, a phase stepping method has to be used. The three components are obtained by Fourier analysis of a few interferograms acquired at slightly different analyzer grating positions. Commonly in the gbPC-CT

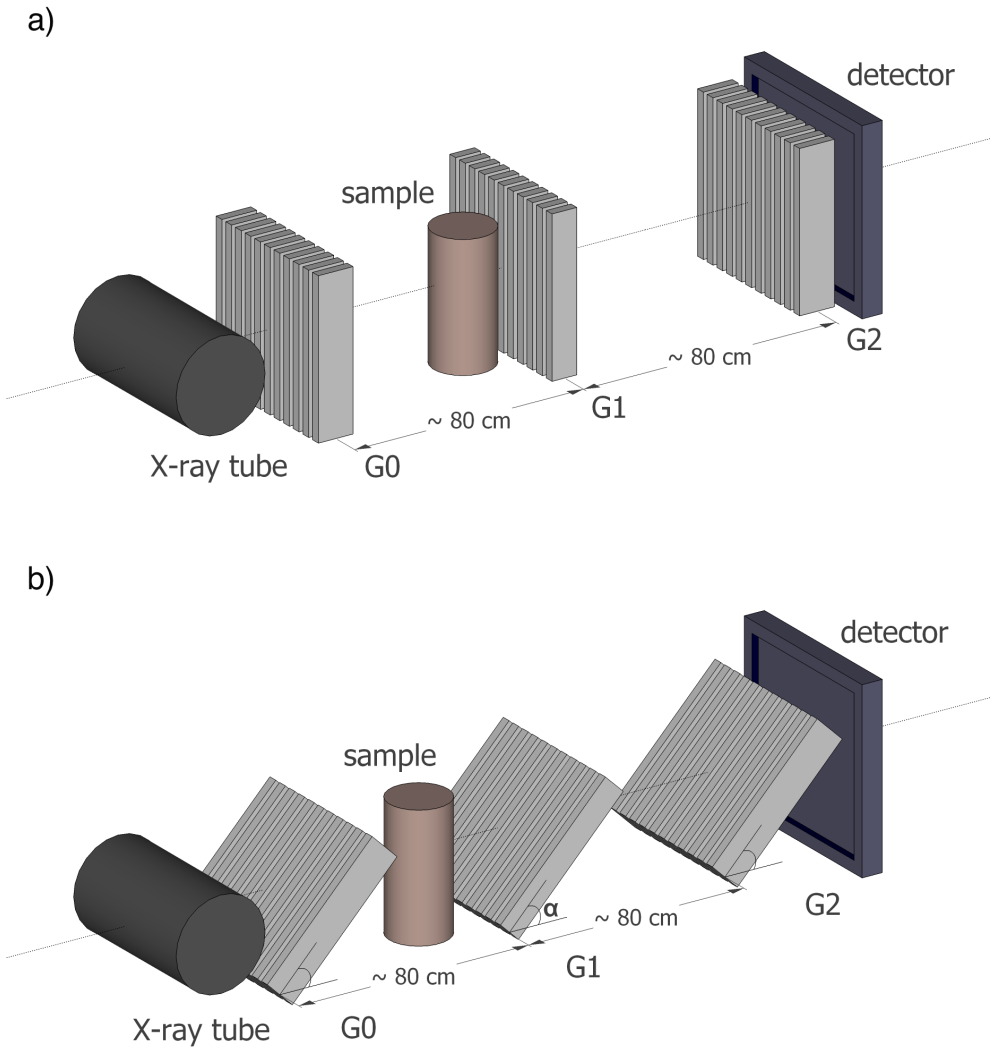

Figure 7.1: Schematic view of the experimental setup at a standard (a) and at a glancing angle configuration (b). The whole setup length was kept the same for both configurations. For the glancing angle configuration, the gratings were inclined at an angle $\alpha = 23.5°$. It increased the effective thickness of the gratings, thus increasing their X-ray absorption and the fringe visibility. Objects and distances are not in scale. Figure adapted from [Sarapata *et al.* 2014b].

scan, the phase stepping is done separately for every rotation angle of the sample. This is inconvenient as it is time-consuming from a clinical setup point of view. Instead, the author used a sliding window interlaced (SWI) stepping method firstly demonstrated by [Zanette *et al.* 2012] with synchrotron radiation (see Figure 7.2). In SWI the grating stepping is done simultaneously with rotation of the sample and the interferometric images obtained in a small angular range (∼1-2°) are used to obtain the attenuation, phase, and scatter (dark-field contrast) information.

This procedure thus makes the gbPC-CT compatible with a continuous rotation

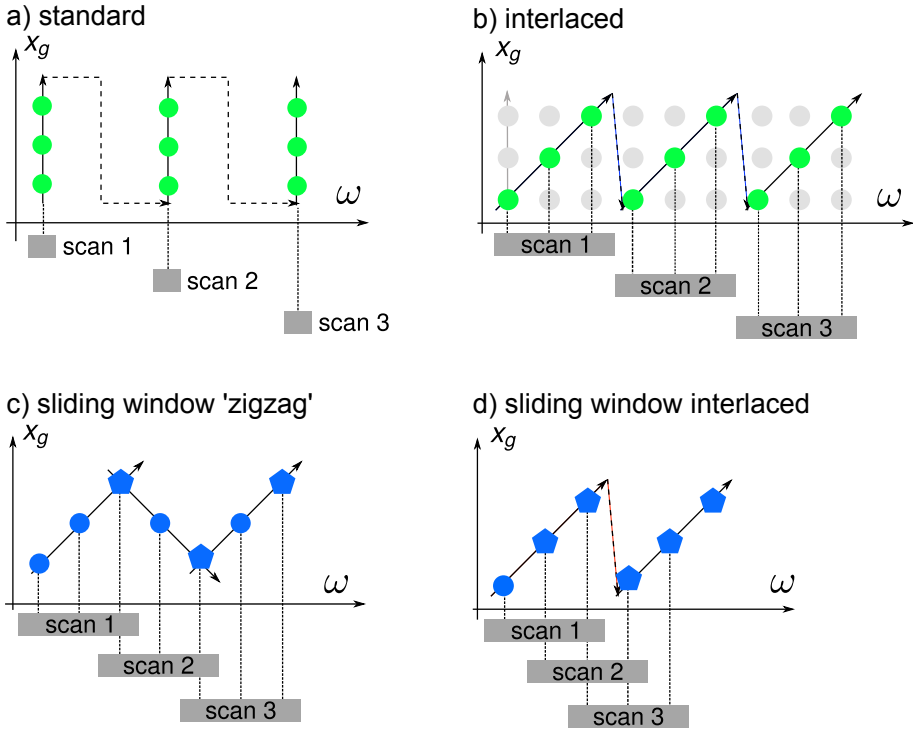

Figure 7.2: Phase-stepping methods represented by the position of the stepped grating x_g as a function of a rotation angle of the sample around the tomography axis ω. Each projection acquired by the detector is represented by a dot or pentagon. Projections represented by pentagons are used for Fourier processing of more than one phase-stepping scan. In the sliding window interlaced method all but one projections are reused. Figure adapted with permission from [Zanette *et al.* 2012].

of the CT gantry. All of the images shown in this chapter were obtained in this way and it is the first time this approach is being presented using a conventional X-ray source, instead of a synchrotron. There were no special modifications made into the processing chain of interferograms in order to account for the rotating object. The SWI data is processed the same way as the standard acquisition, using the Fourier method (with eight grating steps or positions), and resulting in the usual three types of contrast images at each angular position. The only difference is that instead of using eight grating steps at a given CT angle, the SWI processing uses eight grating steps at successive angles to obtain one set of attenuation, phase, and dark-field images. This enables doing gbDPC-CT with only one exposure per CT angle, with the only price paid being an effective angular averaging of the attenuation, phase, and dark-field image over a small angular range (2° in the presented case). The whole CT scan with an angular step of 0.25° over a 200° angle resulted thus in 800 raw images and took about 2 hours. For the CT reconstruction, a cone beam reconstruction code developed at the Johns Hopkins University, and based on a Ram-Lak filter for attenuation, and a Hilbert filter for phase reconstruction was used.

7.2.3 Samples

To compare the image quality of a normal-incidence and a glancing-incidence setup, a well-defined phantom, which mimics material composition of the structures in a human joint was used. The phantom follows the joint CT phantom design by [Anderson *et al.* 2008] and consists of nylon, aluminum, PMMA, and water cylindrical layers placed off center, which simulate trabecular bone, cortical bone, cartilage, and joint fluid, respectively. Further on, to verify the capability of the GAI to discriminate various soft tissues and to study the influence of the exposure time/dose on soft tissue image quality, the author used a second phantom made of different types of fresh pig soft tissues and of a PMMA rod, placed in a plastic vial containing water or a ∼50%–50% alcohol/water mixture. Both samples were immersed in a 40 mm thick water bath during the scan to prevent strong phase jumps ('phase wrapping') at the air-plastic vial boundary. The phantom diameters were limited to ≤25 mm due to the limited field of view of the presented interferometer (∼40x40 mm with ∼1.6 object magnification).

7.2.4 Experiments

A series of various measurements was conducted to address different aspects of GAI and compare it to a standard interferometric system. Firstly, in order to compare the standard phase stepping method with the SWI method, two scans of a joint phantom were performed. The standard method used 200 angular steps of 1° each and 8 phase steps per each angle, which resulted in 1600 projections in total, with 4 mAs exposure per projection. The SWI method used only 800 projections in total, with 0.25° angular step and 8 mAs exposure per projection. Each of the scans lasted approximately 2h.

Secondly, to prove the strong dependence of gbPC-CT image quality on fringe visibility and the importance of having a high visibility interferometer, measurements of the same phantom using the 5.4 μm grating system at normal incidence and at 23.5° glancing incidence were performed. Different thicknesses of phase-grating bars were used to provide the same π-shift at the design X-ray energy of 45 keV. This allowed obtaining very different visibility values while keeping the rest of the important interferometer parameters almost unchanged. In addition, when tilting the gratings not only the effective thickness of the grating bars increases, but also the thickness of the silicon substrates. In order to keep the beam filtration the same, an additional 500 μm of silicon was placed into the beam. Lastly, the exposure times and photon statistics were kept at a comparable but relatively low level in both cases (several mAs per image). As before, both CT scans were performed with SWI method with total of 800 projections.

To quantify the image quality differences, the signal-to-noise ratios and the contrast-to-noise ratios were calculated as:

$$SNR = \frac{|S_a|}{\sigma_a} \qquad and \qquad CNR = \frac{|S_a - S_b|}{\sqrt{(\sigma_a)^2 + (\sigma_b)^2}}\,, \tag{7.1}$$

where S_a and S_b represent the measured signals for different materials, and σ_a, σ_b are standard deviations of the respective signals. The CT reconstruction used 50 µm voxels, and 10 adjacent CT slices were averaged to reduce image noise. To obtain the experimental SNR and CNR values, region-of-interests (ROIs) of 10x10pixels over each of the various materials were chosen.

Finally, a series of soft tissue phantom measurements at different exposure times was performed.

7.2.5 Monte Carlo estimation of dose

As discussed in [Stutman *et al.* 2013] imaging of soft tissues in extremity joints is one of the possible applications for the DPC-CT technique. It is because for extremities the effective dose coefficients are small and because they can be more easily immobilized to allow the longer scan times expected in DPC-CT. As such, the author assumed a human knee to estimate the delivered dose for the measurements with the presented system. The PCXMC 2.0 Monte-Carlo software package [Tapiovaara & Siiskonen] was used, which calculates the mean values of absorbed doses, averaged over the organ volume, using a mathematical phantom or model to simulate different parts of the human body. The calculation is based on the incident air kerma and the geometry of the X-ray beam: focus-to-skin distance FSD, degrees of rotation about the body longitudinal axis and the craniocaudal direction, entry point of the beam axis, and beam height and width at this position.

To estimate the dose that would be delivered to a human knee in the conditions of the above-described experiment, the author assumed exposure of an adult knee at a FSD equal to the source-sample experimental distance of 110 cm, with a 16 cm wide by 5 cm high beam. The air kerma was computed with PCXMC assuming a 65 kVp tube voltage and 2 mm Al/0.125 mm Cu filtering, as in the experiment. The PCXMC kerma calculation is expected to be within about 30 % of the correct value [Tapiovaara & Siiskonen]. The dose reported in this chapter was finally obtained by multiplying the total experimental X-ray tube current-time product (mAs) value, by the dose per mAs computed by PCXMC with the above assumptions.

7.3 Results and discussions

7.3.1 Fringe visibility

Having additional optical elements in the beam, one can adjust the performance of an interferometer by optimizing its components and their parameters. As mentioned, one of the biggest influences on image quality is the fringe visibility.

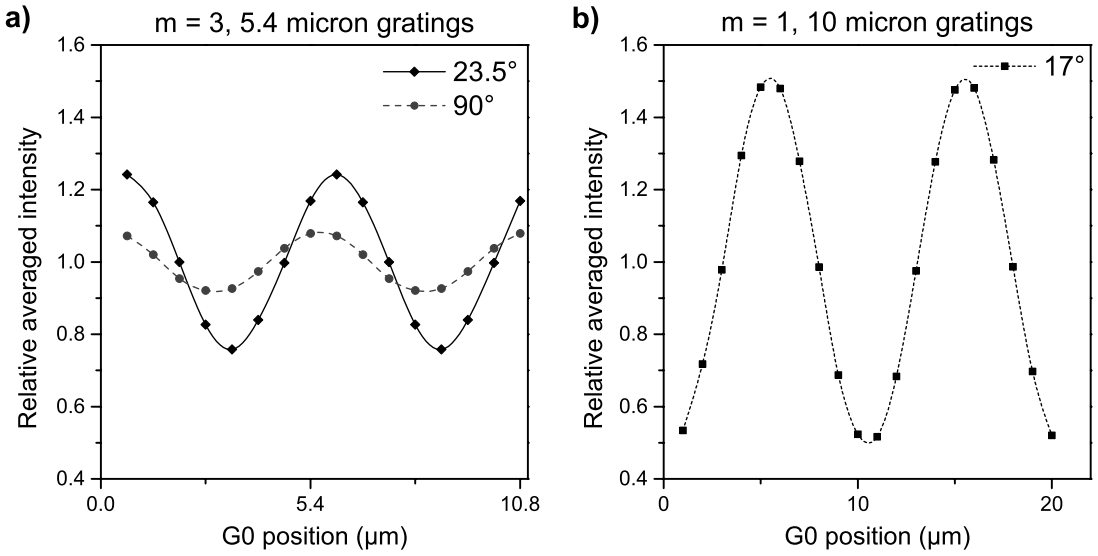

Figure 7.3: Intensity profiles averaged over an area of 10x10 pixels obtained through phase stepping scan. One can see a big increase of the fringe visibility (deeper modulation) caused by the inclination of the gratings. Figure adapted from [Sarapata *et al.* 2014b].

Figure 7.3 shows the normalized intensity variation (averaged over several adjacent pixels) during the phase stepping scan for different setup configurations, from which the fringe visibility is calculated. Figure 7.3(a) shows the intensity profiles obtained with the interferometer in the m=3 Talbot order, with the gratings at a normal incidence angle (90°), and inclined at 23.5°. With the analyzer grating structures' thickness of 100 μm, and at mean X-ray energy of 45 keV, a mean fringe visibility of 7 % and of 23 % was achieved, respectively. Having the interferometer in the m=1 Talbot order, using 10 μm period gratings inclined at 17°, and the X-ray tube running at 55 kVp a remarkably high mean visibility of 50 % was reached (see Fig. 7.3b). To the author's knowledge, it is the highest fringe visibility reported using a conventional X-ray source. Thus, using the GAI design it was possible to get a substantially higher fringe visibility than with the normal-incidence system, making the gbPC-CT technique perform close to its best.

The author also observed an interesting phenomenon of visibility increasing away from the center of the grating, to nearly 60 % (see Fig. 7.4). One possible reason is, that the decreasing width of the grating openings as seen by the X-ray source increases the beam coherence. This effect was not taken into account in the simulations in [Raupach & Flohr 2012], so the experimental visibility can be actually higher than the theoretical prediction, approaching performance comparable to that achieved with partially coherent synchrotron X-rays. This effect did not occur however for the smaller period gratings in a higher Talbot order. In addition, when using inclined gratings the transmitted intensity decreases away from the grating center because of absorption of the X-rays not going perfectly parallel to the tall and narrow grating

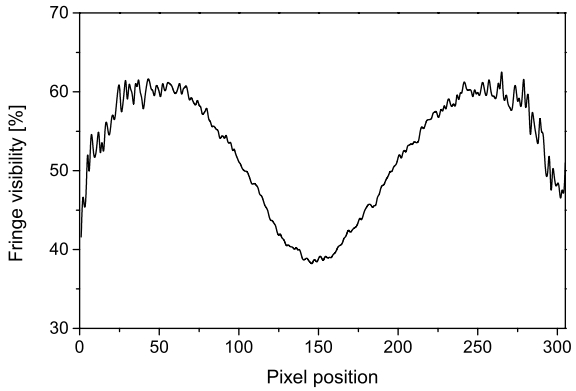

Figure 7.4: Horizontal line profile through a visibility map (fringe visibility values calculated for every pixel). Changing duty cycle of the grating as seen by the X-ray source is a probable cause of increase of the fringe visibility away from the center of the grating. Figure adapted from [Sarapata *et al.* 2014b].

openings but being absorbed in gold, causing lateral field of view vignetting at the grating edges. This can be however dealt with by making on a single substrate an array of narrow sub-gratings having lines tiled along the fan-beam direction (Fig. 7.5). Large FOV in height is obtained by vertically stacking several tiled GAIs.

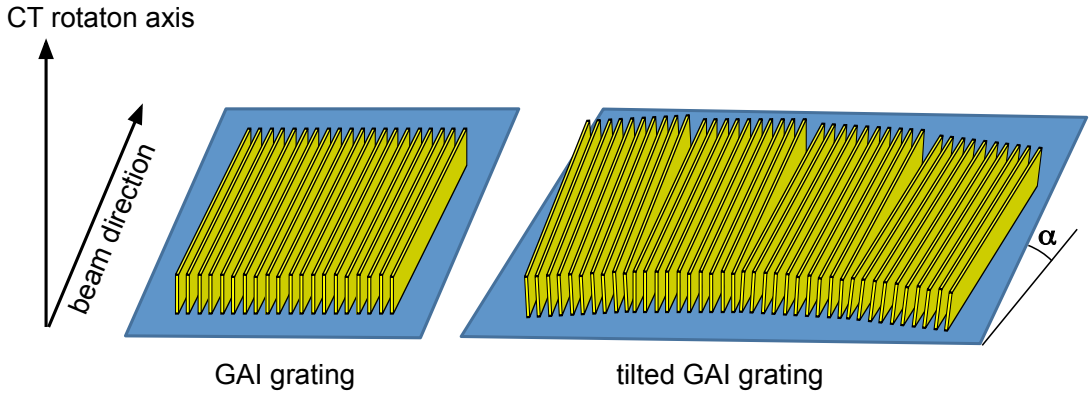

Figure 7.5: Sketches of a standard grating inclined at an angle α for an use in a glancing-angle interferometer (GAI) and an array of tilted gratings following the fan-beam direction for wide FOV glancing-angle GI. Figure adapted with permission from [Stutman & Finkenthal 2014].

Additionally, at shallow inclination angles ($\alpha \leq 20°$) of the gratings a significant change in sensitivity depending on the height position in the sample is expected. The reason is that the sensitivity depends linearly on the distance between the sample and the phase grating G1, being the maximum next to the G1 and decreasing when farther away [Donath *et al.* 2009a]. However, it should be easily possible to numerically correct for such an effect.

7.3.2 Dose estimation by computer simulation

The PCXMC dose calculation shows that the absorbed dose for a human knee would be 1.3 μGy per mAs in the presented setup. Thus for instance, a gbPC-CT scan with 800 frames of 8 mAs each would deliver ∼8.3 mGy dose to the knee. This calculation is based on a numerical model of the knee, which includes skin, muscle, bone and lymph nodes. The largest contribution to the dose comes from the radiation absorbed in the bone. For comparison the delivered dose in an absorption-based cone-beam CT system for musculoskeletal extremities is ∼6.4 mGy for low-dose protocols and ∼15 mGy for high-quality protocols [Zbijewski *et al.* 2011].

The reason that the GAI system is different from conventional absorption-based CT scanners in terms of dose delivered per mAs is that the gratings absorb approximately 50 % of the radiation exiting the tube and that the FSD distance is considerably larger (110 cm versus ∼40 cm in [Stutman *et al.* 2013] for instance). Thus, the GAI experiments were performed with total CT exposures in the range of 1,600 mAs - 12,800 mAs, corresponding to a few times higher than in conventional extremity cone-beam CT, to comparable or lower than in conventional CT.

7.3.3 Comparison between the two phase-stepping methods

Using the GAI with the gratings inclined at 23.5° and operated in the m=3 Talbot order, measurements using the standard and the SWI acquisition schemes were performed, at equal total exposure, as measured by the mA · s product. In terms of equivalent dose delivered to the knee this would correspond to ∼8.3 mGy. Both of the images were obtained with the same inclined grating interferometer. The only difference was the use of the sliding window interlaced phase scanning method versus the standard one.

As shown in Fig. 7.6 and Table 7.1, the SWI method shows higher SNR and CNR for structures close to the center of the sample. As one moves to the periphery the interlaced scan starts losing its advantage over the standard scanning procedure, because of its intrinsic tangential averaging. This can be however improved by further reducing the angular rotation step of the sample (not possible in the presented case due to limited angular resolution of the used rotation stage). The dark spot in the center of the sample is an imperfection which occurred during extrusion of the material.

It is thus interesting to note that the strength of the SWI method does not come primarily from a dose lowering factor. Indeed, as shown in [Raupach & Flohr 2011] there is a minimum number of photons which are needed to obtain the phase information from a periodic function. Having this in mind, SWI is preferable over the standard scanning method as it is possible to obtain fewer images with longer exposures and to gain improved image quality in a region of interest around the center of the sample. Further on, the SWI is advantageous because, for a given total dose, it enables acquiring more photons per projection; having higher photon statistics will

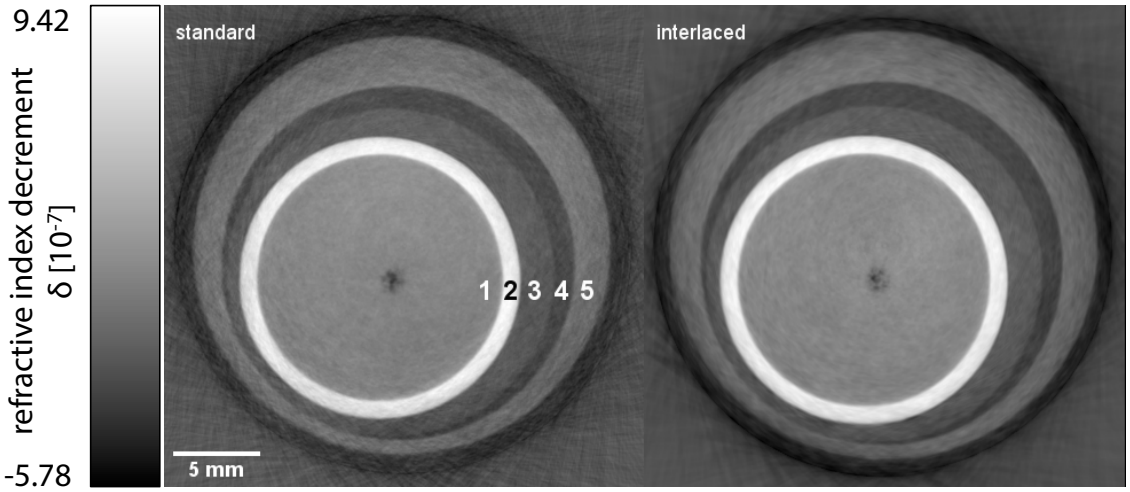

Figure 7.6: Phase contrast CT axial reconstruction slices of a joint phantom, consisting of nylon (1 & 5), aluminum (2), PMMA (3) and water (4), obtained using standard (left) and SWI phase-stepping method (right). Figure adapted from [Sarapata *et al.* 2014b].

Table 7.1: Signal-to-noise and contrast-to-noise ratios comparison for selected materials inside the joint phantom. This table was previously published in [Sarapata *et al.* 2015b].

	SNR	
Material	standard	SWI
Aluminum	19.61	35.43
PMMA	0.02	3.70
Water	6.14	5.73
Nylon	11.34	7.78
	CNR	
PMMA - aluminum	18.32	31.02
PMMA - water	4.27	6.73
Water - nylon	12.77	9.62

make in turn all the algorithms incorporated in the gbPC-CT processing chain to perform better.

7.3.4 High- versus low-visibility system comparison

Figure 7.7 shows a comparison of phase-contrast images obtained using the normal-incidence interferometer (Fig. 7.7b) and using the 23.5° GAI (Fig. 7.7a). The mean fringe visibilities were 7 % and 23 %, respectively. The images were obtained by averaging 15 adjacent CT slices in order to decrease image noise. While in the higher visibility case the phantom is clearly visible in the phase-contrast CT, and all its layers including the PMMA, are distinguishable, the contrast between the PMMA and water layers starts diminishing in the low visibility case. Furthermore, in the lower visibility case image noise is substantially increased.

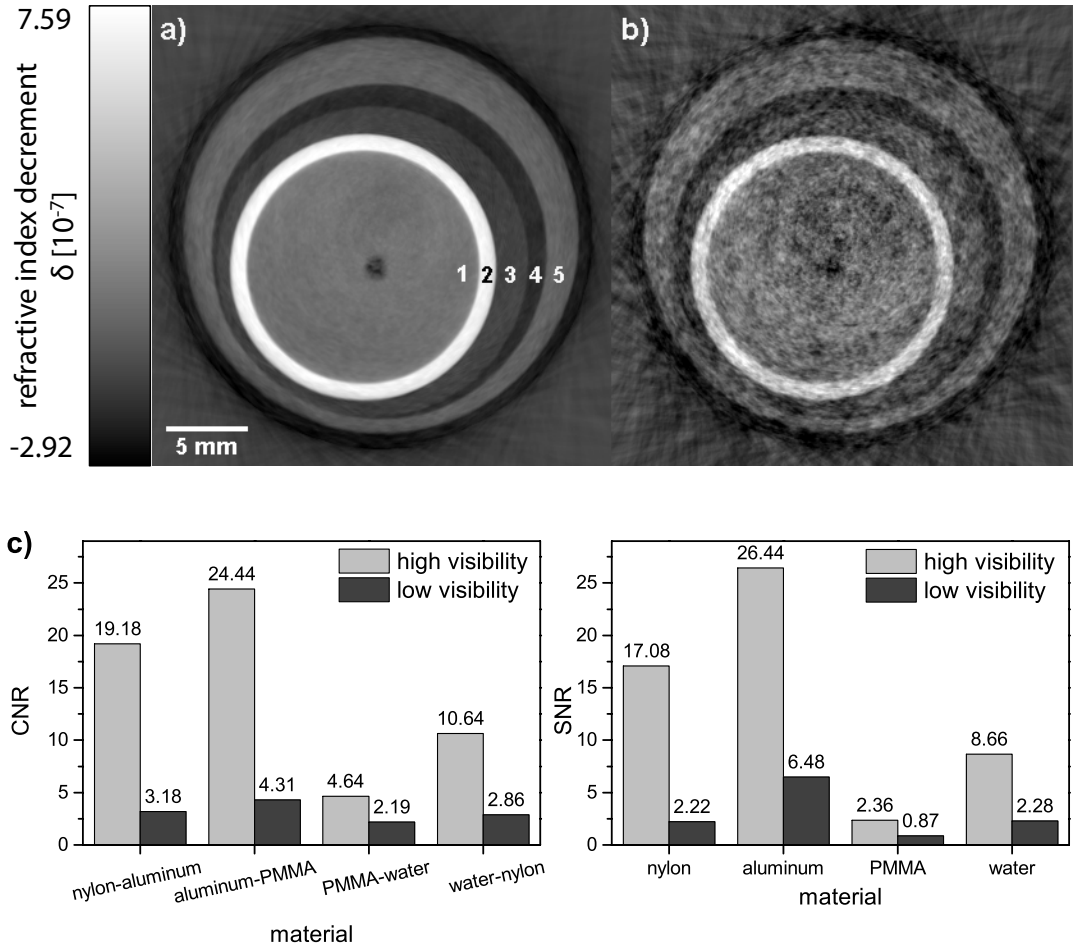

Figure 7.7: Phase-contrast CT axial reconstruction slices of a joint phantom obtained with a high (a) and low visibility system (b) and image quality comparison (c). Figure adapted from [Sarapata *et al.* 2014b].

As before, to quantify the difference, the signal to noise ratios and the contrast to noise ratios were calculated (Fig. 7.7c). Both, CNRs and SNRs are a few times higher for the high visibility system. While contrast between different materials is present in both images, the one obtained with the high visibility system has much improved quality. Since the image formation for the phase-contrast system is different than for the conventional CT and the image quality does not only depend on the amount of radiation illuminating the sample but also on the optical performance (aforementioned fringe visibility) of the interferometer, the presented comparison shows that only by using a high visibility interferometer one can fully take advantage of phase-contrast imaging.

7.3.5 Soft tissue phantom at different exposure times

To investigate the noise behavior of the phase-contrast CT reconstruction at different exposure times and radiation doses, the soft tissue phantom described above was used.

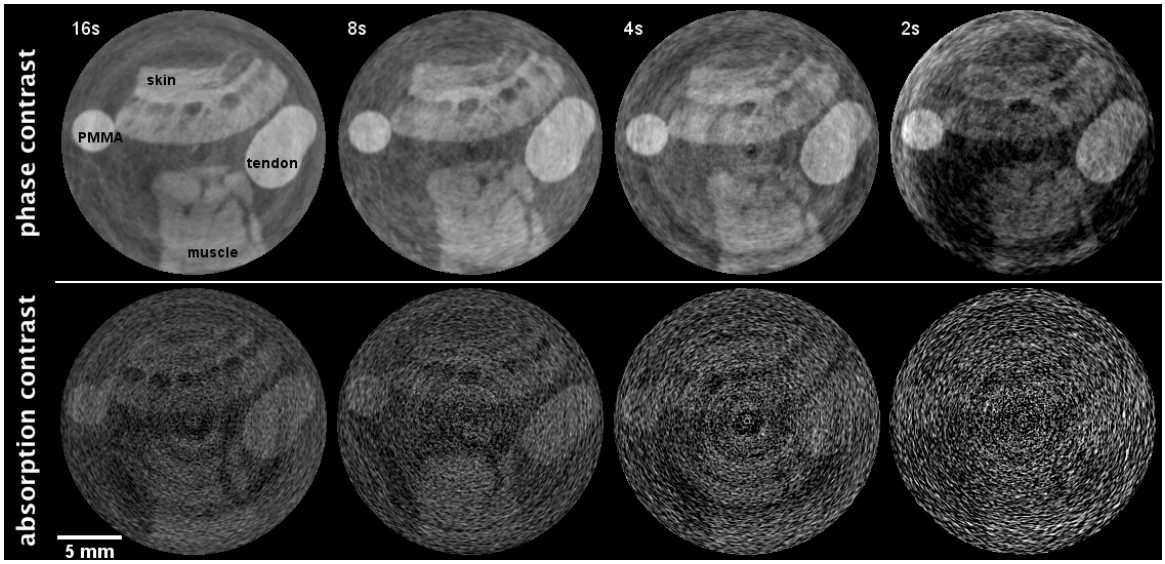

Figure 7.8: Axial slices of PC-CT (top row) and attenuation-CT (bottom row) reconstruction on the soft tissue phantom in 50% ethanol - 50% water mixture, at different exposure times per frame resulting in different estimated dose delivered to the sample (16 s corresponds to ∼16.64 mGy and 2 s to ∼2.08 mGy to a human knee). Figure adapted from [Sarapata *et al.* 2014b].

Contrast-to-noise ratio values and standard deviations of the signals are presented in Fig. 7.9. CNRs between more structures in the phantom were hard to obtain because of the low frequency noise caused by ring reconstruction artifacts (visible for example in the PMMA rod). Figure 7.8 compares the reconstructions of a soft tissue phantom immersed in a 50%-50% water alcohol mixture and obtained at different exposure times per frame ranging from 2 mAs to 16 mAs. The corresponding estimated dose delivered to the knee would range from ∼2.08 mGy to ∼16.64 mGy.

As seen in Fig. 7.8, as the exposure time per frame decreases, the noise increases. For lower exposures, fine structures such as the fat filaments embedded in muscle tissue, start disappearing; however a more detailed study using observer-dependent based image quality assessment [Pflederer *et al.* 2009] is necessary to determine the lowest dose at which the images would still be usable for the clinical evaluation. The image obtained at 2 second exposure time not only has increased noise but also exhibits a phase ramp artifact which is a spatially dependent offset in the shape of an inclined plane. This is because, while in the higher exposure case the peripheral areas outside the object are used to correct for any phase offsets or ramps within the frame, in the lower dose example the algorithms do not perform as well because of substantially decreased photon statistics. The photon statistics at the periphery of the phantom is further decreased by the grating vignetting. Nonetheless, the soft-tissue contrast is much higher in the phase-contrast CT images than in the attenuation-based CT images even at very low (estimated by Monte-Carlo simulation) dose (∼2.08 mGy), while for example the dose during a screening mammogram is usually around 3 mGy

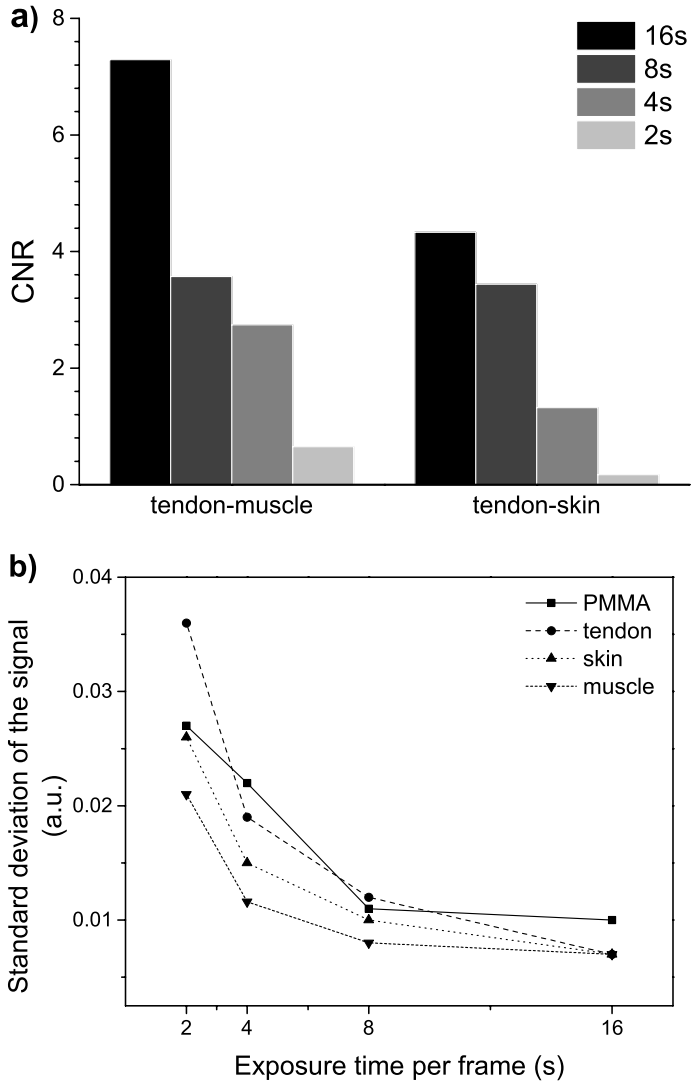

Figure 7.9: CNRs and standard deviations of the signal of the phantom's structures for different exposure times. Figure adapted from [Sarapata *et al.* 2014b].

[Hall & Brenner 2008].

7.3.6 Soft tissue phantom filled with water

Figure 7.10 presents CT reconstruction slices of yet another soft tissue phantom of similar composition, but this time filled with water instead of an alcohol-water mixture. Having various soft tissue types in water, the phantom has refractive indices range very close to what could be expected in a CT scan of a human body (excluding the bones).

The images were again obtained with a SWI scan with 8 mAs per frame and a total of 800 frames, taken in a 0.25° step CT scan over 200°. The phase-contrast CT image in Fig. 7.10a is compared to absorption CT images processed in two different ways. In

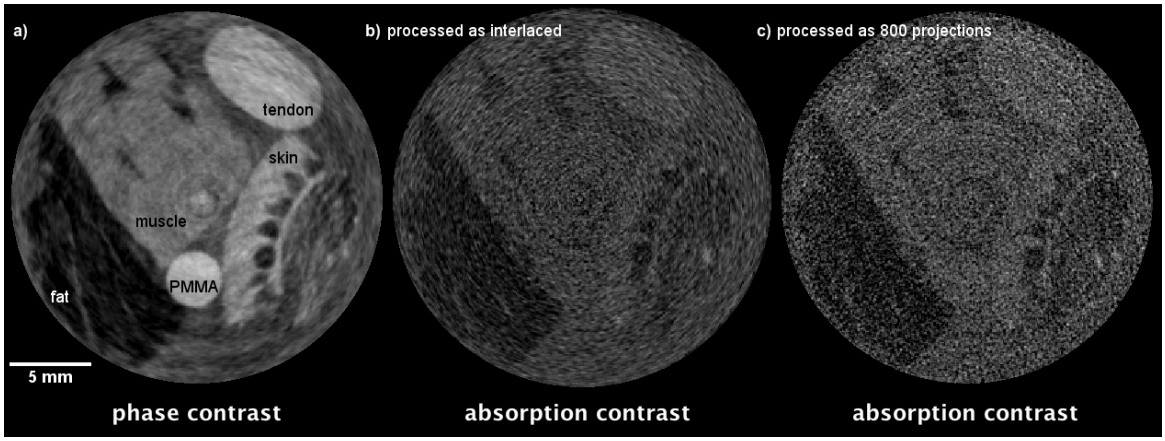

Figure 7.10: Axial slices of phase (a) and attenuation (b and c) CT reconstruction of the soft tissue phantom filled with water at 8 mAs per frame (∼8.32 mGy to a human knee). Figure adapted from [Sarapata *et al.* 2014b].

Fig. 7.10(b) the absorption CT image is obtained using angular averaging over eight angular CT steps, similar to the phase image in Fig. 7.10(a). In Fig. 7.10(c), however, the absorption-based image is obtained from a SWI scan as in a regular CT scan, i.e. without any angular averaging of the projections which makes for tangential blurring in the phase image. The first conclusion from Fig. 7.10(a) is that having a system with high fringe visibility (23 % mean) we were able to decrease the estimated dose to almost clinically compatible levels for extremities, without a significant loss of phase information or of spatial resolution. There is an observable increase of noise compared for instance to the image in Fig. 7.8 (the 16 mAs one) but the phase information is not lost and there is still an evident superiority of the phase-contrast CT image over the absorption CT image. One can easily distinguish between various tissue types and while the tendon and the PMMA rod are almost invisible in the absorption CT image, they show up nicely in the phase-contrast CT image. It is important to note that the spatial resolution in these images (50 µm voxels) is much higher than that used in conventional CT scans of human tissue nowadays. This, together with the inherently low absorption contrast for soft tissues, explains the low contrast in the absorption-based image.

In addition, there is a clear difference in the noise characteristics between the phase-contrast and the absorption CT images, with the phase-contrast image exhibiting predominant lower spatial frequency noise. As discussed in [Singh *et al.* 2012], this difference arises both from the use of different back-projection filters in the CT reconstructions (linear ramp filter for absorption data and Hilbert filter for phase data), and from the different noise transfer properties of PC-CT compared to absorption-CT. It is also important to note that there is much room for improvement in the CT reconstruction code: to further reduce the noise in the gbPC-CT images novel back-projection and noise filtering methods could be applied and recent improvements in data processing and reconstruction such as iterative or model-based reconstruc-

tion could be implemented [Thibault *et al.* 2007, Singh *et al.* 2012, Yoon *et al.* 2012, Vogel & Oman 1996].

Nonetheless, taking into account that gbPC-CT provides much improved soft tissue contrast while exhibiting spatial resolution considerably better than conventional CT, the results obtained in our studies at a dose almost half of that used in high-quality conventional CT [Zbijewski *et al.* 2011] show the big potential of phase-contrast computed tomography.

7.4 Conclusions

X-ray phase-contrast CT has an obvious advantage over conventional attenuation-based CT in the form of increased soft tissue contrast. However, translating this asset into a clinical environment is not a trivial thing to achieve. One has to think about dose limits, practicability of the system and so forth. It appears as an indisputable prerequisite, however, that for clinical applications the grating-based PC-CT system must be optimized for best optical performance possible, i.e. having both high fringe visibility and high angular sensitivity, at high X-ray energy. As discussed in [Raupach & Flohr 2012], performing measurements with a system having low visibility and compensating for this by using a high X-ray dose will not be clinically compatible.

The results presented in this chapter show the importance of fringe visibility for image quality and demonstrate essential first steps towards a clinical gbPC-CT system. Due to photon attenuation in the gratings and the use of a low current X-ray tube (max 1 mA) the scan time of the system was way beyond clinical requirements. However, assuming a high performance X-ray tube capable of continuous operation at 30 mA current, such as the Comet MXR-160HP/11 for instance, the time would be shortened to approximately 3.5 minutes. This value could be further decreased by using rotating anode X-ray tubes, which typically deliver from several tens to over 100 mA current. This could however have a negative influence on the fringe visibility due to significantly increased spot size and thus blurring of the interference pattern. The extremity joints are a good place to start clinical implementation of gbPC-CT because the expected longer scan times in gbPC-CT can be more easily accommodated.

Further optimization of the reconstruction, processing techniques and artifact corrections could enable gbPC-CT scans for applications having more stringent dose limitations, such as breast gbPC-CT. Moreover, the dose in gbPC-CT could be further lowered using spectral filtering or shaping, because phase-contrast imaging uses strictly only the transmitted part of the spectrum [Stutman *et al.* 2013]; the low energy radiation, which contributes strongly to the dose without contributing to the phase image, can be filtered out before entering the patient. In order to make the technique fully clinically compatible such that it is possible to use with very low photon counts or with effective pixel sizes similar to what is standardly used in the clinical

environment (200 μm and more) the noise characteristics of the phase-contrast images have to be changed by a different than the phase-stepping phase retrieval process, such as that presented in [Zhu *et al.* 2010, Marschner *et al.* 2015].

As major technical improvements in the grating fabrication are not expected in the near future, the glancing-angle interferometer offers a simple solution for gbPC-CT at X-ray energies in the clinical diagnostic range (50 - 120 kVp approximately), in optimal conditions of high fringe visibility and with clinically acceptable dose. A remarkable inference from the presented results is that, with further refinements in reconstruction and de-noising techniques, it appears possible to obtain enhanced soft tissue contrast simultaneously with increased spatial resolution (comparable to micro-CT scanners), while still using clinically compatible dose levels. This is much more encouraging for clinical implementation of gbPC-CT than the conclusions in [Raupach & Flohr 2012], which assessed that high resolution clinical gbPC-CT will not be possible. This assessment did not consider however the possibility of much improved optical interferometer performance. The author believes that gbPC-CT could indeed become a powerful complementary technique to conventional CT, to be used for specific applications which will take advantage of high resolution soft tissue imaging, such as mammography, joint cartilage imaging, and many others.

Chapter 8

Multi-contrast imaging for materials science applications

Contents

8.1 Introduction 93

8.2 Materials and methods 94

8.2.1 Experimental setup 94

8.2.2 Sample 95

8.2.3 Image acquisition and processing 95

8.2.4 Analysis of spatial resolution 95

8.3 Results 96

8.4 Discussions and conclusions 99

Multi-contrast capabilities of grating interferometry combined with a high spatial resolution of a few micrometers make it a suitable tool for assessing multiple phases inside porous and composite materials. Making use of these advantages, this chapters presents quantitative results of a proof-of-principle experiment performed using grating-based microtomography on a type of porous building material, i.e. concrete. Thanks to the complementarity of the contrast channels, more concrete phases could be distinguished than in conventional attenuation-based imaging. The phase-contrast reconstruction shows uncommonly high contrast between the hardened cement paste and the aggregates and thus allows easy 3D segmentation. Thanks to the dark-field image, micro-cracks inside the coarse aggregates are visible. The presented results demonstrate that is it possible to obtain high-contrast phase and dark-field 3D images of concrete that bring unique information to conventional attenuation-based imaging. The fact that grating-based X-ray microtomography can be, as presented in this chapter, successfully applied at high photon energies should open up new non-destructive 3D imaging opportunities for a wide range of applications in the R&D communities related with characterization of porous building materials and composite geomaterials in general.

The majority of the results presented in this chapter were published in:
A. Sarapata, M. Ruiz-Yaniz, I. Zanette, A. Rack, F. Pfeiffer, and Julia Herzen, "Multi-

contrast 3D X-ray imaging of porous and composite materials," Applied Physics Letters **106**, 16 (2015).

8.1 Introduction

Concrete is the most widely used man-made material in construction. Extensive knowledge about its microstructure is essential for understanding its mechanical strength, or permeability. Efforts at this employ various imaging techniques, among which are scanning or transmission electron microscopy [Diamond 2004, Zingg *et al.* 2008], and optical microscopy [Campbell 1986, Leemann *et al.* 2006]. Methods highly sensitive to variations in chemical composition, such as powder X-ray diffraction (XRD) [Handoo *et al.* 2002], or nuclear magnetic resonance (NMR) [Colombet & Grimmer 1994, Le Saout *et al.* 2006], are also commonly used. However, powder XRD in its basic form provides no spatial resolution as the sample has to be crushed into a fine powder, while the spatial resolution of NMR is inferior to what is achievable nowadays by electron microscopy or X-ray imaging methods [Shemesh *et al.* 2012, Mitchell *et al.* 2013]. X-ray diffraction can be extended to a 2D mode but it provides information only on thin samples. In order to access information in 3D, X-ray diffraction computed tomography (XRD-CT) can be used. It might be a great tool to follow distribution of the hydration products but suffers from very long acquisition times because of its point-by-point scanning character [Artioli *et al.* 2010]. The existing microscopy techniques are mostly destructive when the three-dimensional information is of interest. The transmission methods require the sample to be cut into micrometer-thick slices. Further, in scanning electron microscopy or reflection optical microscopy the sample has to be destroyed by polishing off the successive surfaces to access the depth information. In addition, the sample preparation in electron microscopy can be a complex and time consuming process.

Three dimensional X-ray imaging, on the other hand, is non-destructive thus enabling measurements of the samples in their native state. Attenuation-based X-ray microtomography has been previously used for investigation of concrete's microstructure and porosity [Bentz *et al.* 1994, Bentz *et al.* 2000, Chotard *et al.* 2003, Gallucci *et al.* 2007] or evolution of the material phases during the hydration process [Helfen *et al.* 2005, Gastaldi *et al.* 2012, Parisatto *et al.* 2014]. However, high-contrast images are produced only when the differences in the attenuation cross sections are substantial. For example, good contrast between air and high-Z materials (e.g. aluminum, steel) is relatively easy to accomplish due to a high mass density difference. In case of materials with similar attenuation properties (e.g. PMMA and water or cement paste and certain types of aggregates), the contrast is not sufficient, especially at high X-ray energy above 50 keV, where the attenuation cross sections are decreased, which strongly limits discrimination between different material phases [Artioli *et al.* 2012].

Grating-based microtomography has the potential to overcome the aforementioned limitations of conventional attenuation-based imaging thanks to its high density resolution, quantitativeness, and complementarity of information. It allows for simultaneous and nondestructive determination of the complex X-ray index of refraction and the scattering coefficient distribution inside an object in three dimensions. Additionally, it can be seen as supplementary to the above-mentioned techniques because of its ability to deliver complementary information, especially due to the dark-field contrast which is related to the small-angle scattering power of the sample [Wang *et al.* 2009, Bech *et al.* 2010] at structures typically below the spatial resolution of the imaging setup. This multi-contrast information improves differentiation of various constituents inside multiple-phase composites such as concrete, which is an important aspect of understanding the macroscopic properties of the material such as strength and durability [Ingham 2011, Artioli *et al.* 2012]. As an example, one emphasized by [Trtik *et al.* 2013], the electron density distribution of concrete phases is of significant interest for understanding real cementitious systems.

This chapter exploits the multi-contrast capabilities of X-ray grating interferometry for enhanced imaging of complex systems, with a proof-of-concept demonstration on concrete. The experimental implementation is based upon a very well developed method, but its application to a porous building material is very relevant from a technological point of view, as concrete, represents a novelty and an important step forwards the characterization of porous and composite materials in general.

8.2 Materials and methods

8.2.1 Experimental setup

The experiment was carried out at the ID19 beamline of the European Synchrotron Radiation Facility (Grenoble, France). A detailed description of the interferometer at the beamline ID19 can be found in [Weitkamp *et al.* 2010]. The interferometer was operated at the design X-ray energy of 53 keV in the 1st fractional Talbot order. The inter-grating distance was 135 mm. Both gratings were produced by the Karlsruhe Institute of Technology (KIT) and had the same period, 2.4 µm. The phase grating G1 was made of nickel and had a height of 9.3 µm. The absorption grating G2 was made of gold and had a height of 105 µm. The X-ray photons were generated by a wiggler and monochromatized by a silicon double crystal monochromator in Bragg geometry. X-rays had a nominal energy of 53 keV. The detector was an indirect conversion system consisting of a 200 µm thick $Lu_3Al_5O_{12}$:Ce scintillator lens coupled to a CCD camera with an effective pixel size of 8 µm.

8.2.2 Sample

The chosen object of interest was a concrete piece. Typically, concrete is considered a three-phases material and consists of coarse granular material (aggregate or filler), hardened cement paste and a transition zone [Nilsen & Monteiro 1993]. Each of the phases can be further divided into multiple phases of different chemical composition and porosity. Further information and in-depth description of concrete's structure can be found for example in [Nilsen & Monteiro 1993].

The concrete sample was supplied by Sika Deutschland GmbH (Germany). The sample was prepared with the following mix design parameters: 33.9 % of Portland CEM I 52.5 R-NA cement (initial water-to-cement ratio of 0.39), 33.7 % of sand 0/2 (particle size ranging from 0 to 2 mm), 20.8 % of grit 2/8 (particle size 2 - 8 mm) and 11.5 % of grit 8/16; the volume fractions being expressed in respect to one cubic meter of compacted concrete. The aggregates were obtained from Hacon Betonwerke (Germany). The final density of the fresh cement was 2.33 kg/dm^3. After demoulding it was cured in water for 6 days and stored at 20°C and 65 % relative humidity until being shipped. Upon receipt it was cut so as to obtain a cylindrical sample about 10 mm in diameter and 50 mm in length. Hereafter, the sample did not undergo any preconditioning, and after several weeks it was measured in air without controlling humidity or temperature.

8.2.3 Image acquisition and processing

In order to obtain the three contrast modes, a phase-stepping procedure using four steps over one period of the interference pattern was used. Each frame was obtained with an exposure time of one second. The CT acquisition consisted of 1,200 rotation angles over 360 degrees. The phase stepping was done separately for every rotation angle of the sample. CT reconstruction was again performed with a GPU-based filtered backprojection (FBP) reconstruction code developed "in-house" [Fehringer *et al.* 2014] based on a Ram-Lak filter for the attenuation and the dark-field reconstruction and a Hilbert filter for the phase reconstruction. A different filter in the phase-contrast reconstruction was used because the projection images represent line integrals of partial derivatives of the object's refractive index decrement.

8.2.4 Analysis of spatial resolution

The spatial resolution of the used imaging system is limited in our case by the pixel size and the point spread function of the detector. Resolution limits related to the interferometer such as the separation of the beams diffracted by the phase grating or the fact that the resolution cannot be better than twice the period of the analyzer grating are negligible because they are lower than the used pixel size.

The image resolution of the projections of the three contrast channels is theoretically the same. This fact was confirmed for attenuation and phase-contrast (excluding

dark-field) projections by MTF measurements by [Herzen 2010]. What differs is a sub-pixel sensitivity of each of the modes resulting in visibility of different features in the resulting images.

Further, the use of a different filtering kernel for the phase-contrast reconstruction than for the attenuation and the dark-field data set results in different spatial resolutions. Attenuation-contrast and dark-field reconstructions can yield a slightly higher spatial resolution than a phase-contrast reconstruction, which is observable in the respective MTFs for Ram-Lak and Hilbert FBP. Moreover, in our case the attenuation image contains edge enhancement effect which "artificially" increases the spatial resolution when measured on the image.

An estimate of the spatial resolution of the experimental data was obtained by means of Fourier analysis of the reconstructed tomograms. For that purpose, the radial spectral power (RSP) of a region of interest inside the sample (200 x 200 pixels) was calculated and divided by the RSP of a background region of the same size [Modregger *et al.* 2007]. The ratio was plotted against the spatial frequency (line pair/mm). The spatial resolution was estimated as the first observed frequency greater than twice the mean value of the baseline associated with the noise. This frequency value in LP/mm corresponds to a peak to peak distance, so the effective spatial resolution was taken as half of it.

8.3 Results

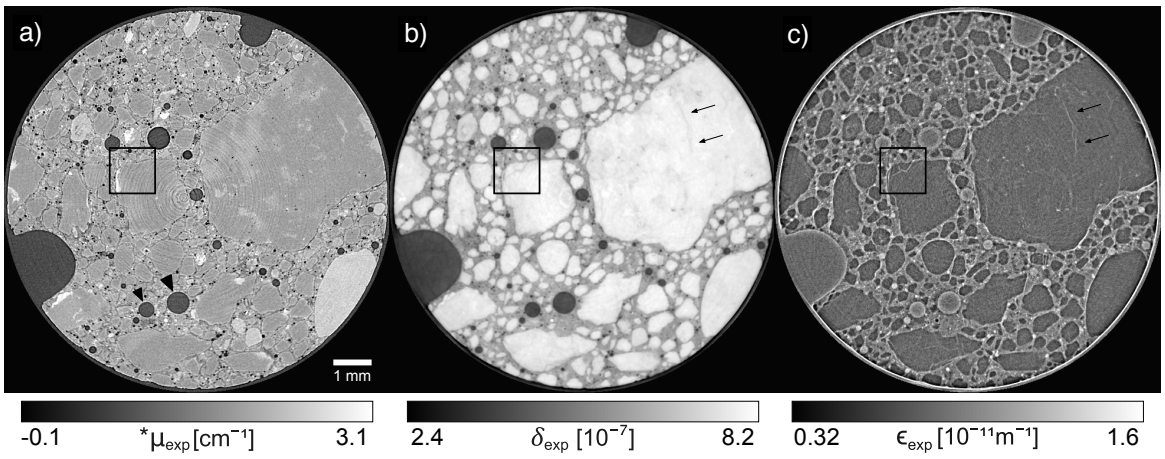

Figure 8.1: Attenuation- (a), phase- (b), and dark-field (c) contrast axial slices from a tomographic reconstruction of the concrete sample. The phase-contrast slice (b) shows increased contrast over the attenuation-contrast slice (a). Aggregates can be more easily distinguished from the cement paste looking at either phase or dark-field reconstructions. Figure adapted from [Sarapata *et al.* 2015a].

Figure 8.1 shows attenuation- (a), phase- (b), and dark-field (c) contrast axial reconstruction slices of the concrete sample described above. The phase-contrast

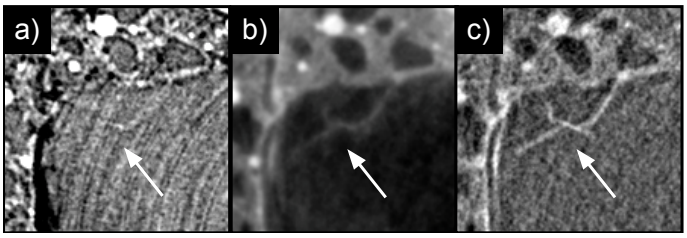

Figure 8.2: Regions of interest of the attenuation- (a), phase- (b), and dark-field (c) tomograms. Note that for better visibility, the gray scale for attenuation- and phase-contrast image was inverted with respect to the Figure 1, so the micro-crack appears as a white line on a dark background. Figure adapted from [Sarapata *et al.* 2015a].

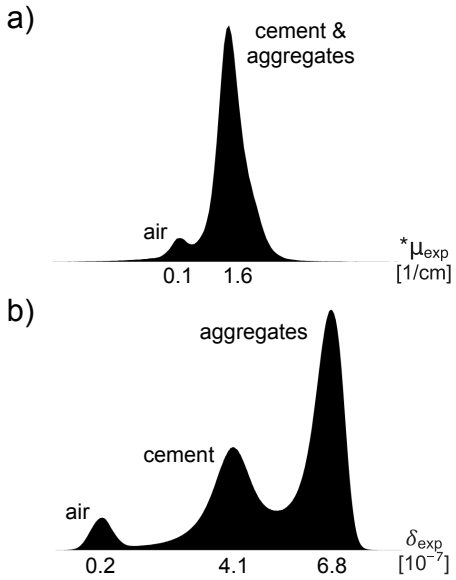

Figure 8.3: Histograms of the whole 3D volume datasets of the attenuation- (a), and the phase-contrast CT (b). In (a), only two distinct peaks for air and the concrete sample as a whole can be seen. In (b), there are three distinct peaks corresponding to air, hardened cement paste and aggregates. Figure adapted from [Sarapata *et al.* 2015a].

image shows strong contrast between the aggregates and the hardened cement paste, much higher than what achieved in the attenuation-based image. In the attenuation image, only the boundary is visible due to the edge-enhancement effect, which helps to identify interfaces but does not give quantitative information on inhomogeneous objects. It has its origin in the propagation of the X-ray beam from the sample to the detector and can be detected with small pixel sizes when the sample is illuminated by a partially spatially coherent beam [Paganin & Nugent 1998]. When calculating quantitative values of the linear attenuation coefficient μ this propagation-based effect was not taken into account and not corrected for; therefore, these values are only an approximation (indicated by the asterisk in Fig. 8.1).

When looking at all three images, not only is the differentiation between the aggregates and the cement paste simple, but also subtle variations within the coarse

aggregates are visible. This is because of the different chemical compounds that make up the aggregates.

Furthermore, the phase-contrast and the dark-field reconstructions produce superior visibility of the micro-cracks inside the aggregates (indicated by the arrows), which are completely invisible in the attenuation-based reconstruction. The cracks are not visible because of insufficient contrast and sensitivity to sub-pixel structures of the attenuation-contrast image. Even removal of the ring artifacts, which are visible in Figure 8.1 (a) and Figure 8.2 (a), by the post-processing method based on combined wavelet and Fourier filtering [Münch *et al.* 2009] does not improve visibility of the micro-cracks. Especially useful for their visibility is the dark-field image. It provides the highest visibility and localization of micro-cracks of the three contrast modalities, which could be seen in Figure 8.2. It is because the dark-field image contrast is produced based on small-angle scattering on structures at micrometer and sub-micrometer length scale. Therefore, information on changes in microstructure of the object below the detector resolution is revealed.

Lastly, similarly to the phase-contrast image, the dark-field image makes the difference between the aggregates and the cement paste easier to see than the attenuation image does. The cement paste scatters X-rays much more strongly than the aggregates because of its high microstructural heterogeneity on the length scale, to which the interferometer is the most sensitive.

The spatial resolution (SR) was estimated using the radial spectral power (RSP) separately for each of the contrast channels. The determined effective SR was respectively 25 µm for the phase-contrast reconstruction, 26 µm for the dark-field contrast, and 17 µm for the attenuation-based reconstruction. The higher spatial resolution of the attenuation-contrast image is a result of the above-mentioned edge-enhancement effect.

Table 8.1: Contrast-to-noise ratios calculated for phase- and attenuation-contrast reconstructions.

	CNR	
	attenuation	phase
air - cement	1.7	4.6
air - agregate	3.6	25.8
cement - agregate	0.3	6.9

In order to quantify the contrast difference between the attenuation and the phase-contrast reconstructions, we calculated the contrast-to-noise ratios (CNRs) as $|S_a - S_b|/\sqrt{(\sigma_a)^2 + (\sigma_b)^2}$, where S represents the measured signal, i.e., average pixel value in a region of interest, and σ represents its standard deviation. Subscripts a and b refer to two different regions of interest chosen for different material phases. The results can be found in Table 8.1. Higher contrast-to-noise ratios between all the constituents were found in the phase-contrast reconstruction, which confirms the high

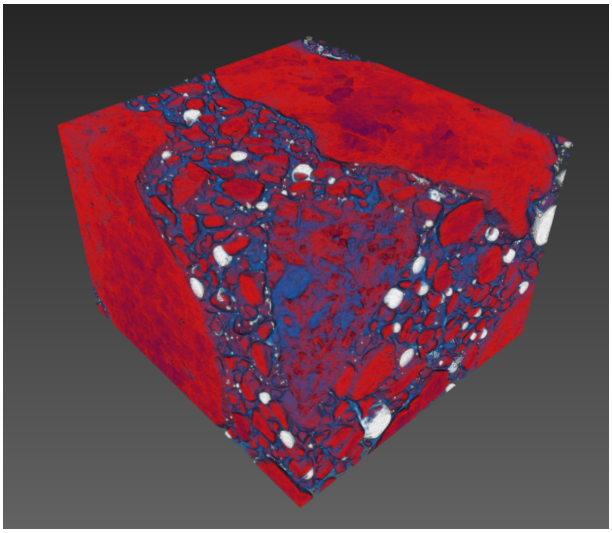

Figure 8.4: Volume rendering of the phase-contrast CT data set. Three distinct phases can be visualized, i.e. aggregates (red), hardened cement paste (blue), and air bubbles (white).

sensitivity of phase imaging to electron density variations. Moreover, a histogram analysis (see Figure 8.3) of both 3D data sets shows an additional peak in the distribution of gray values in the phase-contrast reconstruction. The high contrast between the aggregates and the cement paste around them makes the image segmentation process easier and made it possible to render the imaged volume shown in Figure 8.4. As currently a lot of effort is invested in the image processing and analysis side of segmenting aggregates from standard attenuation-based X-ray microtomography results, we expect a big impact of the presented method on research communities investigating not only concrete, but porous and composite building materials in general.

8.4 Discussions and conclusions

The big advantage of GI to conventional attenuation-based imaging is that it provides three different physical properties of an object using a single measurement. The complementarity of information is very important for improving understanding of the object being investigated. This is especially true for complex multiple-phase systems like concrete in which the microscopic structure and composition is associated with many important material properties such as strength, permeability and durability. Conventionally, concrete has to be studied with different techniques, making it difficult to correlate the findings - especially when 3D imaging techniques are combined with 2D sectioning or when the spatial resolutions of the techniques differ.

X-ray grating interferometry provides nondestructive access to the full complex index of refraction, in turn improving material segmentation [Nielsen *et al.* 2012] and giving us access to an effective atomic number [Qi *et al.* 2010]. In addition, it provides local small-angle scattering power of the sample, increasing detectability of

certain features [Yaroshenko *et al.* 2014], and imaging unsaturated water transport in porous materials in radiography [Yang *et al.* 2014]. It is important to note that the three different contrast channels are inherently registered, which opens possibilities for combining the distinct information via image fusion [Wang *et al.* 2013, Scholkmann *et al.* 2014] or for advanced signal extraction and denoising [Köhler & Roessl 2012]. The spatial resolution of each of the contrast channels might differ because of a different filtering kernel used for the phase-contrast reconstruction than for the attenuation and the dark-field data sets. Attenuation-contrast and dark-field reconstructions can yield a slightly higher spatial resolution than a phase-contrast reconstruction, which is observable in the respective Modulation Transfer Functions for Ram-Lak and Hilbert FBPs [Li *et al.* 2013]. In the presented case, the attenuation image contains edge-enhancement effect which artificially increases the spatial resolution when measured on the image.

Altogether, no need of sample preparation, non-destructiveness and fast acquisition of the full 3D volumetric information make X-ray GI a unique and helpful technique for the characterization of porous and composite materials such as concrete. Many applications may profit from this technique since its characteristics are well suited for verification procedures in which samples should not be destroyed. Because a very long measurement time of XRD-CT makes it useful only for limited studies and attenuation-based microtomography is generally not sensitive enough, the presented technique could be considered as bridging the gap between these two by delivering complementary information, especially thanks to the dark-field contrast.

Because of the strong dependence of sensitivity and resolution on grating periodicity and the sample position in respect to the phase grating, GI is currently limited by the grating fabrication process. For the moment, high-energy and high-resolution (effective pixel size of a few micrometers) grating interferometry is only possible with synchrotron-radiation sources. However, the spatial resolution of laboratory-based X-ray grating interferometers is bound to increase in the near future thanks to the constant progress of such systems. In fact, a high-resolution GI system using a magnifying projection geometry was already presented in [Engelhardt *et al.* 2007], but it was operated at the design energy of 17.5 keV and has not been yet realized with shorter X-ray wavelengths.

In order to fully benefit from the potential of 3D imaging with X-ray grating interferometry for porous and composite materials, further investigations and developments are needed. A relation between refractive index decrement/electron density and the chemical composition of various cement phases has to be found, similar to what has been done by [Trtik *et al.* 2013] for ptychography. To do this, a test concrete sample with various aggregates of known chemical composition and size distribution should be manufactured and placed into the beam in order to provide a direct comparison between the expected and the measured quantitative values. Sensitivity to various phases has to be analyzed to determine the number of phases that could be

differentiated. In addition, a high-energy, high-resolution grating interferometer with a laboratory-based X-ray tube is needed to enable greater accessibility to the technique. Nonetheless, the presented results already show the method's great capabilities and its big potential.

To summarize, the results presented in this chapter demonstrate the suitability of X-ray grating interferometry as a non-destructive quantitative technique for three-dimensional investigations of complex porous and composite materials, with a proof-of-concept demonstration on concrete. Simultaneous reconstruction of the X-ray linear attenuation coefficient and the refractive index decrement, which further relates to the electron density, greatly improves differentiation of various constituents in bulk concrete. Superior visibility and localization of micro-cracks in 3D, thanks to the additional dark-field channel, could be a useful tool for concrete sustainability studies. The presented results prove that grating interferometry has a potential to open up new non-destructive multi-contrast 3D X-ray imaging opportunities for a wide range of applications in the geo- and materials science community.

Chapter 9
Summary and outlook

In this thesis, a high-energy X-ray grating interferometer with a conventional, polychromatic X-ray source was implemented, characterized, and its applicability to biomedical imaging and materials science was investigated. Imaging experiments using synchrotron radiation were also performed, either as a benchmark for the technique or a proof-of-concept demonstration of a possible application.

Summary of the contributions to the field made in this work follows the order of the experimental results chapters.

Development of a high-energy Talbot-Lau interferometer: Throughout this thesis, both hardware and software improvements to the experimental setup operated at its 45 keV design energy were made. Various components were added to an existing system to ensure fully functional operation and uncomplicated measurements of various samples later on. The data processing chain was extended by quantitative analysis algorithms and various plug-ins for artifact-free attenuation, phase-contrast, and dark-field tomograms.

Quantitative characterization of materials: The ability to relate the gray values of an image to the physical properties of the measured sample, such as its mass and electron density, is advantageous and therefore desirable in many research fields. In this work, a special projection-only sample geometry for the high-energy grating interferometer was presented and used to yield accurate electron density values for various homogeneous materials. The method can be successfully used in all fields in which electron density is essential, e.g., characterization of the materials used in X-ray optics, radiation therapy planning, or soft tissue phantom design dedicated for X-ray phase-contrast imaging.

With regards to the tomography mode, the high-energy setup was proven to provide accurate reconstructions of the linear attenuation coefficient μ and the refraction index decrement δ, the latter being further related to the electron density distribution inside a sample. Despite the polychromatic spectrum and high photon energies, in comparison with absorption tomograms, phase-contrast tomograms showed higher contrast-to-noise ratios between all the low-Z material pairs. Both reconstructions of high-Z materials provided complementary information and improved the differentiation between various material pairs when compared to attenuation-only-based tomography. The system's design energy, higher than ones typically used in biomedical

imaging of dissected tissue samples, enabled the investigation of objects made of various dense and high-Z materials. Because such samples generally absorb stronger than soft tissues, their investigation would have been practically impossible with commonly-used GI setups designed for photon energies below 30 keV. As an example, tomograms of a part of human cervical spine were presented. Only the phase-contrast reconstruction revealed the internal structure of the intervertebral discs, which proves the big potential of high-energy GI for biomedical imaging, in particular for imaging of cartilage surrounded by bones.

Complementarity of contrast channels: Varying complementarity of phase and attenuation contrast channels with changing atomic number of the material being imaged was assessed experimentally at photon energies of 40 keV and above. Using two phantoms, it was shown that attenuation and phase contrast images of low-Z materials are no longer complementary. The only advantage of phase contrast over attenuation contrast was the increased image quality, strongly dependent on the fringe visibility. The complementarity of both signals was still obtained for high-Z materials and therefore a more sophisticated material characterization was possible.

Dedicated phase-contrast phantoms: A short overview of existing phantoms for X-ray imaging explained a necessity for phantoms dedicated specifically for the additional image contrasts, i.e. phase and dark-field channels. As a result of the quantitative measurements enabled by grating interferometry, materials equivalent to breast tissue in their refraction properties were found. In order to match more tissue types with their equivalent plastic materials, more extensive analysis and comparison should be conducted. Additionally, by precise control over materials' parameters, a low-contrast phantom with inserts of electron densities varying by only a few percent was manufactured. The presented phantoms are proofs of concept for quality-control phantoms, which in general are valuable tools for stability testing of many imaging systems.

Dose-relevant phase-contrast CT: An importance of the optimum optical performance for a clinically-compatible gbPC-CT system was discussed. The necessary first steps towards a dose-compatible system were presented. Namely, the fringe visibility was increased by inclining the gratings and an acquisition scheme compatible with a continuos rotation of a gantry was used. It was demonstrated, that with these two improvements, it is feasible to perform gbPC-CT at diagnostic X-ray energy high enough to penetrate thick human body parts. As for the radiation dose, the levels comparable to conventional absorption-based CT were reached and did not exceed the clinically-compatible ones by a few orders of magnitude, like many other gbPC-CT results do. The presented results proved that grating interferometry could be someday used for specific applications which will take advantage of high-resolution soft-tissue

imaging, such as mammography, joint cartilage imaging, and many others. Further work on a different scheme for a phase signal extraction and possibly an alternative lab-based X-ray source with better coherence parameters are necessary to make the technique fully clinically possible.

Proof-of-principle implementation of GI for concrete studies: The proof-of-concept grating-based microtomography conducted on a piece of concrete showed a tremendous potential of the technique for characterization of porous building materials, and in general composites made out of elements up to the 4^{th} row of the periodic table. A systematic study is needed to evaluate sensitivity of the method to various concrete phases. Further porous and composite materials should be investigated in order to find a correlation between the gray values in the images with chemical composition of the object's constituents. Moreover, future work should focus on developments of the lab-based GI systems to advance their spatial resolution towards what is achievable with synchrotron-based interferometers.

The fact that grating interferometry can be, as presented in this thesis, successfully implemented with a polychromatic spectrum with photon energies higher than typically used in biomedical imaging is very promising and should open the technique to a broad range of laboratory-based applications in medical and biomedical imaging, materials science, fabrication of X-ray optics, and many others. As the performance of X-ray grating interferometry depends heavily on gratings quality and coherence properties of the X-ray source used, further increase in image quality of the resulting multi-contrast images is expected in the near future.

References

[Anderson *et al.* 2008] Andrew E. Anderson, Benjamin J. Ellis, Christopher L. Peters and Jeffrey A. Weiss. *Cartilage Thickness: Factors Influencing Multidetector CT Measurements in a Phantom Study.* Radiology, vol. 246, issue no. 1, pages 133–141, Jan 2008. (Cited on page 80.)

[Artioli *et al.* 2010] G. Artioli, T. Cerulli, G. Cruciani, M. C. Dalconi, G. Ferrari, M. Parisatto, A. Rack and R. Tucoulou. *X-ray diffraction microtomography (XRD-CT), a novel tool for non-invasive mapping of phase development in cement materials.* Anal. Bioanal. Chem., vol. 397, issue no. 6, art. no. 2131–2136, Apr 2010. (Cited on page 93.)

[Artioli *et al.* 2012] Gilberto Artioli, Maria Chiara Dalconi, Matteo Parisatto, Luca Valentini, Marco Voltolini and Giorgio Ferrari. *3D imaging of complex materials: the case of cement.* Int. J. Mater. Res., vol. 103, issue no. 2, art. no. 145–150, 2012. (Cited on pages 93 and 94.)

[Attwood 2007] D. Attwood. Soft x-rays and extreme ultraviolet radiation: Principles and applications. Cambridge University Press, 2007. (Cited on page 9.)

[Bandyopadhyay & Segre 2009] P. Bandyopadhyay and C. Segre. *Mucal 1.3.* http://www.csrri.iit.edu/mucal.html, issue no. 16, April 2009. (Cited on pages 41 and 53.)

[Barrett & Swindell 1996] H.H. Barrett and W. Swindell. Radiological imaging: The theory of image formation, detection, and processing. Numeéro v. 2. Academic Press, 1996. (Cited on pages 10 and 12.)

[Baur 2013] R. Baur. *Development And Application Of A Grating Interferometer At The Cornell High Energy Synchrotron Source.* PhD thesis, Cornell University, 2013. (Cited on page 26.)

[Bech *et al.* 2010] M Bech, O Bunk, T Donath, R Feidenhans'l, C David and F Pfeiffer. *Quantitative x-ray dark-field computed tomography.* Phys. Med. Biol., vol. 55, issue no. 18, pages 5529–5539, Aug 2010. (Cited on pages 18, 20 and 94.)

[Bech 2008] M. Bech. *X-ray imaging with a grating interferometer.* PhD thesis, University of Copenhagen, 2008. (Cited on pages 24, 28 and 31.)

[Bentz *et al.* 1994] D.P. Bentz, Nicos. S. Martys, P. Stutzman, M. S. Levenson, E.J. Garboczi, J. Dunsmuir and L. M. Schwartz. *X-Ray Microtomography of an Astm C109 Mortar Exposed to Sulfate Attack.* MRS Proceedings, vol. 370, art. no. 77, Jan 1994. (Cited on page 93.)

[Bentz *et al.* 2000] D. P. Bentz, D. A. Quenard, H. M. Kunzel, J. Baruchel, F. Peyrin, N. S. Martys and E. J. Garboczi. *Microstructure and transport properties of porous building materials. II: Three-dimensional X-ray tomographic studies*. Mater. Struct., vol. 33, issue no. 3, art. no. 147–153, Apr 2000. (Cited on page 93.)

[Berger *et al.* 2010] MM. J. Berger, J. H. Hubbell, S. M. Seltzer, J. Chang, J. S. Coursey, R. Sukumar, D. S. Zucker and K. Olsen. *XCOM: Photon Cross Section Database*. 2010. (Cited on pages 12, 50 and 55.)

[Bonse & Hart 1965] U. Bonse and M. Hart. *An X-Ray Interferometer*. Appl. Phys. Lett., vol. 6, issue no. 8, art. no. 155, 1965. (Cited on pages 1 and 15.)

[Bravin *et al.* 2012] Alberto Bravin, Paola Coan and Pekka Suortti. *X-ray phase-contrast imaging: from pre-clinical applications towards clinics*. Phys. Med. Biol., vol. 58, issue no. 1, pages R1–R35, Dec 2012. (Cited on page 75.)

[Campbell 1986] Donald H Campbell. Microscopical examination and interpretation of portland cement and clinker. Portland Cement Assn, 1986. (Cited on page 93.)

[Chabior *et al.* 2011] Michael Chabior, Tilman Donath, Christian David, Oliver Bunk, Manfred Schuster, Christian Schroer and Franz Pfeiffer. *Beam hardening effects in grating-based x-ray phase-contrast imaging*. Medical Physics, vol. 38, issue no. 3, pages 1189–1195, 2011. (Cited on page 44.)

[Chapman *et al.* 1997] D Chapman, W Thomlinson, R E Johnston, D Washburn, E Pisano, N Gmuer, Z Zhong, R Menk, F Arfelli and D Sayers. *Diffraction enhanced x-ray imaging*. Phys. Med. Biol., vol. 42, issue no. 11, pages 2015–2025, Nov 1997. (Cited on page 16.)

[Cheng *et al.* 2013] Chee-Wai Cheng, Li Zhao, Mark Wolanski, Qingya Zhao, Josuha James, Kate Dikeman, Michael Mills, Mei Li, Shiv P. Srivastava, Xing Qi Lu and Indra J. Das. *Comparison of tissue characterization curves for different CT scanners: implication in proton therapy treatment planning*. Translational Cancer Research, vol. 1, issue no. 4, 2013. (Cited on page 36.)

[Chotard *et al.* 2003] T. J Chotard, M. P Boncoeur-Martel, A Smith, J. P Dupuy and C Gault. *Application of X-ray computed tomography to characterise the early hydration of calcium aluminate cement*. Cem. Concr. Compos., vol. 25, issue no. 1, art. no. 145 –152, 2003. (Cited on page 93.)

[Cloetens *et al.* 1996] Peter Cloetens, Raymond Barrett, Jose Baruchel, Jean-Pierre Guigay and Michel Schlenker. *Phase objects in synchrotron radiation hard x-ray imaging*. J. Phys. D: Appl. Phys., vol. 29, issue no. 1, pages 133–146, Jan 1996. (Cited on page 16.)

[Cloetens *et al.* 1999] P. Cloetens, W. Ludwig, J. Baruchel, D. Van Dyck, J. Van Landuyt, J. P. Guigay and M. Schlenker. *Holotomography: Quantitative phase tomography with micrometer resolution using hard synchrotron radiation x rays*. Appl. Phys. Lett., vol. 75, issue no. 19, art. no. 2912, 1999. (Cited on page 17.)

[Colombet & Grimmer 1994] Pierre Colombet and Arnd-Rüdiger Grimmer. Application of nmr spectroscopy to cement science, guerville, 1992: Proceedings. Gordon and Breach Science, 1994. (Cited on page 93.)

[David *et al.* 2002] C. David, B. Noehammer, H. H. Solak and E. Ziegler. *Differential x-ray phase contrast imaging using a shearing interferometer*. Appl. Phys. Lett., vol. 81, issue no. 17, art. no. 3287, 2002. (Cited on pages 17 and 20.)

[Davis *et al.* 1995] T. J. Davis, D. Gao, T. E. Gureyev, A. W. Stevenson and S. W. Wilkins. *Phase-contrast imaging of weakly absorbing materials using hard X-rays*. Nature, vol. 373, issue no. 6515, pages 595–598, Feb 1995. (Cited on page 16.)

[Diamond 2004] Sidney Diamond. *The microstructure of cement paste and concrete–a visual primer*. Cem. Concr. Compos., vol. 26, issue no. 8, pages 919–933, Nov 2004. (Cited on page 93.)

[Donath *et al.* 2009a] Tilman Donath, Michael Chabior, Franz Pfeiffer, Oliver Bunk, Elena Reznikova, Juergen Mohr, Eckhard Hempel, Stefan Popescu, Martin Hoheisel, Manfred Schuster, Joachim Baumann and Christian David. *Inverse geometry for grating-based x-ray phase-contrast imaging*. Journal of Applied Physics, vol. 106, issue no. 5, 2009. (Cited on pages 32, 38 and 83.)

[Donath *et al.* 2009b] Tilman Donath, Franz Pfeiffer, Oliver Bunk, Waldemar Groot, Martin Bednarzik, Christian Grünzweig, Eckhard Hempel, Stefan Popescu, Martin Hoheisel and Christian David. *Phase-contrast imaging and tomography at 60 keV using a conventional x-ray tube source*. Rev. Sci. Instrum., vol. 80, issue no. 5, art. no. 053701, 2009. (Cited on pages 3, 47 and 77.)

[Donath *et al.* 2010] Tilman Donath, Franz Pfeiffer, Oliver Bunk, Christian Grünzweig, Eckhard Hempel, Stefan Popescu, Peter Vock and Christian David. *Toward Clinical X-ray Phase-Contrast CT*. Investigative Radiology, art. no. 1, 2010. (Cited on page 2.)

[Engelhardt *et al.* 2007] Martin Engelhardt, Joachim Baumann, Manfred Schuster, Christian Kottler, Franz Pfeiffer, Oliver Bunk and Christian David. *High-resolution differential phase contrast imaging using a magnifying projection geometry with a microfocus x-ray source*. Appl. Phys. Lett., vol. 90, issue no. 22, art. no. 224101, 2007. (Cited on page 100.)

[Fehringer *et al.* 2014] Andreas Fehringer, Tobias Lasser, Irene Zanette, Peter B. NoÃ«l and Franz Pfeiffer. *A versatile tomographic forward- and back-projection approach on multi-GPUs*. Medical Imaging 2014: Image Processing, Mar 2014. (Cited on pages 52 and 95.)

[Fitzgerald 2000] Richard Fitzgerald. *Phase-Sensitive X-Ray Imaging*. Phys. Today, vol. 53, issue no. 7, art. no. 23, 2000. (Cited on pages 1, 14 and 20.)

[Gallucci *et al.* 2007] E. Gallucci, K. Scrivener, A. Groso, M. Stampanoni and G. Margaritondo. *3D experimental investigation of the microstructure of cement pastes using synchrotron X-ray microtomography*. Cem. Concr. Res., vol. 37, issue no. 3, art. no. 360–368, Mar 2007. (Cited on page 93.)

[Gastaldi *et al.* 2012] D. Gastaldi, F. Canonico, L. Capelli, E. Boccaleri, M. Milanesio, L. Palin, G. Croce, F. Marone, K. Mader and M. Stampanoni. *In situ tomographic investigation on the early hydration behaviors of cementing systems*. Constr. Build. Mater., vol. 29, art. no. 284–290, Apr 2012. (Cited on page 93.)

[Goldstone 1990] K.E. Goldstone. *Tissue Substitutes in Radiation Dosimetry and Measurement*. Clinical Radiology, vol. 41, issue no. 3, art. no. 220, March 1990. (Cited on page 66.)

[Grandl *et al.* 2013] Susanne Grandl, Marian Willner, Julia Herzen, Doris Mayr, Sigrid D. Auweter, Alexander Hipp, Franz Pfeiffer, Maximilian Reiser and Karin Hellerhoff. *Evaluation of phase-contrast CT of breast tissue at conventional X-ray sources - presentation of selected findings*. Zeitschrift für Medizinische Physik, vol. 23, issue no. 3, pages 212–221, Sep 2013. (Cited on page 75.)

[Grandl *et al.* 2014] Susanne Grandl, Marian Willner, Julia Herzen, Aniko Sztrokay-Gaul, Doris Mayr, Sigrid D. Auweter, Alexander Hipp, Lorenz Birnbacher, Mathias Marschner, Michael Chabior and et al. *Visualizing Typical Features of Breast Fibroadenomas Using Phase-Contrast CT: An Ex-Vivo Study*. PLoS ONE, vol. 9, issue no. 5, art. no. e97101, May 2014. (Cited on page 75.)

[Guinier 1994] A. Guinier. X-ray diffraction in crystals, imperfect crystals, and amorphous bodies. Dover Books on Physics Series. Dover, 1994. (Cited on pages 14 and 37.)

[Hall & Brenner 2008] E J Hall and D J Brenner. *Cancer risks from diagnostic radiology*. The British Journal of Radiology, vol. 81, issue no. 965, pages 362–378, May 2008. (Cited on page 88.)

[Handoo *et al.* 2002] S. K. Handoo, S Agarwal and S. K. Agarwal. *Physicochemical, mineralogical, and morphological characteristics of concrete exposed to elevated temperatures*. Cem. Concr. Res., vol. 32, issue no. 7, art. no. 1009–1018, 2002. (Cited on page 93.)

[Helfen *et al.* 2005] L.B Helfen, P. MikulÃk, F. Dehn and T. Baumbach. *Three-dimensional imaging of cement microstructure evolution during hydration*. Adv. Cem. Res., vol. 17, issue no. 3, art. no. 103–111, Jan 2005. (Cited on page 93.)

[Henke *et al.* 1993] B. L. Henke, E. M. Gullikson and J. C. Davis. *X-ray interactions: photoabsorption, scattering, transmission, and reflection at E=50-30000 eV, Z=1-92*. Atomic Data and Nuclear Data Tables, vol. 54, pages 181–342, 1993. data available at `http://www-cxro.lbl.gov`. (Cited on page 10.)

[Herzen *et al.* 2009] Julia Herzen, Tilman Donath, Franz Pfeiffer, Oliver Bunk, Celestino Padeste, Felix Beckmann, Andreas Schreyer, Christian David*et al.* *Quantitative phase-contrast tomography of a liquid phantom using a conventional x-ray tube source*. Opt. Express, vol. 17, issue no. 12, pages 10010–10018, 2009. (Cited on pages 2, 48 and 53.)

[Herzen *et al.* 2014] Julia Herzen, Marian S. Willner, Alexander A. Fingerle, Peter B. Noël, Thomas Köhler, Enken Drecoll, Ernst J. Rummeny and Franz Pfeiffer. *Imaging Liver Lesions Using Grating-Based Phase-Contrast Computed Tomography with Bi-Lateral Filter Post-Processing*. PLoS ONE, vol. 9, issue no. 1, art. no. e83369, 2014. (Cited on pages 2 and 47.)

[Herzen 2010] J. Herzen. *A grating interferometer for materials science imaging at a second-generation synchrotron radiation source*. PhD thesis, Universität Hamburg, 2010. (Cited on page 96.)

[Hetterich *et al.* 2013] Holger Hetterich, Sandra Fill, Julia Herzen, Marian Willner, Irene Zanette, Timm Weitkamp, Alexander Rack, Ulrich Schüller, Mojtaba Sadeghi, Richard Brandl and et al. *Grating-based X-ray phase-contrast tomography of atherosclerotic plaque at high photon energies*. Zeitschrift für Medizinische Physik, vol. 23, issue no. 3, pages 194–203, Sep 2013. (Cited on page 75.)

[Hetterich *et al.* 2014] Holger Hetterich, Marian Willner, Sandra Fill, Julia Herzen, Fabian Bamberg, Alexander Hipp, Ulrich Schüller, Silvia Adam-Neumair, Stefan Wirth, Maximilian Reiser and et al. *Phase-Contrast CT: Qualitative and Quantitative Evaluation of Atherosclerotic Carotid Artery Plaque*. Radiology, vol. 271, issue no. 3, pages 870–878, Jun 2014. (Cited on pages 2 and 47.)

[Hubbell 1969] John Howard Hubbell. *Photon cross sections, attenuation coefficients, and energy absorption coefficients from 10 keV to 100 GeV*. Rapport technique, NSRDS-NBS, 1969. (Cited on pages 12 and 50.)

[Ingham 2011] Jeremy Ingham. *Microscopy for the Built Environment*. Infocus Magazine, vol. 22, art. no. 4, 2011. (Cited on page 94.)

[James 1967] R.W. James. The optical principles of the diffraction of x-rays. Crystalline state. Bell, 1967. (Cited on pages 14, 37 and 49.)

[Kalef-Ezra *et al.* 1998] J.A. Kalef-Ezra, A.H. Karantanas, T. Koligliatis, A. Boziari and P. Tsekeris. *Electron density of tissues and breast cancer radiotherapy: a quantitative CT study*. International Journal of Radiation Oncology, Biology, Physics, vol. 41, pages 1209–1214, 1998. (Cited on page 36.)

[Kalra *et al.* 2004] Mannudeep K. Kalra, Michael M. Maher, Thomas L. Toth, Leena M. Hamberg, Michael A. Blake, Jo-Anne Shepard and Sanjay Saini. *Strategies for CT Radiation Dose Optimization1*. Radiology, vol. 230, issue no. 3, pages 619–628, Mar 2004. (Cited on page 75.)

[Kenntner 2012] J. Kenntner. *Fabrication of x-ray gratings with high aspect ratios for phase contrast computer tomography*. PhD thesis, Karlsruhe Institute of Technology, 2012. (Cited on page 29.)

[Köhler & Roessl 2012] Thomas Köhler and Ewald Roessl. *Simultaneous de–noising in phase contrast tomography*. AIP Conf. Proc., vol. 1466, art. no. 78–83, 2012. (Cited on pages 52 and 100.)

[Köhler *et al.* 2011] Thomas Köhler, Klaus Jürgen Engel and Ewald Roessl. *Noise properties of grating-based x-ray phase contrast computed tomography*. Med. Phys., vol. 38, issue no. S1, art. no. S106, 2011. (Cited on pages 51, 60, 71 and 72.)

[Lau 1948] E. Lau. *Beugungserscheinungen an Doppelrastern*. Annalen der Physik, vol. 437, issue no. 7-8, pages 417–423, 1948. (Cited on page 21.)

[Le Saout *et al.* 2006] Gwenn Le Saout, Eric Lécolier, Alain Rivereau and HélÃ¨ne Zanni. *Chemical structure of cement aged at normal and elevated temperatures and pressures*. Cem. Concr. Res., vol. 36, issue no. 1, art. no. 71–78, Jan 2006. (Cited on page 93.)

[Leemann *et al.* 2006] Andreas Leemann, Beat Münch, Philippe Gasser and Lorenz Holzer. *Influence of compaction on the interfacial transition zone and the permeability of concrete*. Cem. Concr. Res., vol. 36, issue no. 8, pages 1425–1433, Aug 2006. (Cited on page 93.)

[Li *et al.* 2013] Ke Li, Joseph Zambelli, Nicholas Bevins, Yongshuai Ge and Guang-Hong Chen. *Spatial resolution characterization of differential phase contrast CT systems via modulation transfer function (MTF) measurements.* Phys. Med. Biol., vol. 58, issue no. 12, art. no. 4119–4135, May 2013. (Cited on page 100.)

[Malecki *et al.* 2012] A. Malecki, G. Potdevin and F. Pfeiffer. *Quantitative wave-optical numerical analysis of the dark-field signal in grating-based X-ray interferometry.* Europhysics Letters, vol. 99, issue no. 4, art. no. 48001, 2012. (Cited on pages 40, 41 and 53.)

[Marschner *et al.* 2015] M. Marschner, L. Birnbacher, M. Willner, M. Chabior, A. Fehringer, J. Herzen, P. B. Noël and F. Pfeiffer. *Redefining the lower statistical limit in x-ray phase-contrast computed imaging.* Medical Imaging 2015: Physics of Medical Imaging, Mar 2015. (Cited on page 91.)

[Matcher *et al.* 2004] Stephen J Matcher, C Peter Winlove and Sergei V Gangnus. *The collagen structure of bovine intervertebral disc studied using polarization-sensitive optical coherence tomography.* Phys. Med. Biol., vol. 49, issue no. 7, pages 1295–1306, Mar 2004. (Cited on page 58.)

[McCullough 1975] Edwin C. McCullough. *Photon attenuation in computed tomography.* Med. Phys., vol. 2, issue no. 6, pages 307–320, 1975. (Cited on pages 11, 12, 49 and 50.)

[Meiser *et al.* 2014] J. Meiser, M. Amberger, M. Willner, D. Kunka, P. Meyer, F. Koch, A. Hipp, M. Walter, F. Pfeiffer and J. Mohr. *Increasing the field of view of x-ray phase contrast imaging using stitched gratings on low absorbent carriers.* Proc. SPIE, vol. 9033, art. no. 903355, Mar 2014. (Cited on page 49.)

[Meyer *et al.* 2010] Pascal Meyer, Joachim Schulz and Volker Saile. *Deep X-Ray Lithography.* In Yi Qin, editeur, Micro-Manufacturing Engineering and Technology, pages 202–220. Elsevier, 2010. (Cited on page 48.)

[Mitchell *et al.* 2013] J. Mitchell, T. C. Chandrasekera, D. J. Holland, L. F. Gladden and E. J. Fordham. *Magnetic resonance imaging in laboratory petrophysical core analysis.* Phys. Rep., vol. 526, issue no. 3, art. no. 165–225, May 2013. (Cited on page 93.)

[Modregger *et al.* 2007] Peter Modregger, Daniel Lübbert, Peter Schäfer and Rolf Köhler. *Spatial resolution in Bragg-magnified X-ray images as determined by Fourier analysis.* Phys. Stat. Sol. (a), vol. 204, issue no. 8, art. no. 2746–2752, Aug 2007. (Cited on page 96.)

[Mohr *et al.* 2012] Jürgen Mohr, Thomas Grund, Danays Kunka, Johannes Kenntner, Juerg Leuthold, Jan Meiser, Joachim Schulz and Marco Walter. *High aspect ratio gratings for X-ray phase contrast imaging.* AIP Conf. Proc., vol. 1466, pages 41–50, 2012. (Cited on pages 2 and 48.)

[Momose *et al.* 2003] Atsushi Momose, Shinya Kawamoto, Ichiro Koyama, Yoshitaka Hamaishi, Kengo Takai and Yoshio Suzuki. *Demonstration of X-Ray Talbot Interferometry.* Jpn. J. Appl. Phys., vol. 42, issue no. Part 2, No. 7B, pages L866–L868, Jul 2003. (Cited on pages 17 and 20.)

[Momose *et al.* 2006] Atsushi Momose, Wataru Yashiro, Yoshihiro Takeda, Yoshio Suzuki and Tadashi Hattori. *Phase Tomography by X-ray Talbot Interferometry for Biological Imaging.* Jpn. J. Appl. Phys., vol. 45, issue no. 6A, pages 5254–5262, Jun 2006. (Cited on page 23.)

[Momose 2005] Atsushi Momose. *Recent Advances in X-ray Phase Imaging.* Jpn. J. Appl. Phys., vol. 44, issue no. 9A, pages 6355–6367, Sep 2005. (Cited on pages 1, 14 and 15.)

[Münch *et al.* 2009] Beat Münch, Pavel Trtik, Federica Marone and Marco Stampanoni. *Stripe and ring artifact removal with combined wavelet–Fourier filtering.* Opt. Express, vol. 17, issue no. 10, art. no. 8567, 2009. (Cited on page 98.)

[Nielsen *et al.* 2012] M S Nielsen, T Lauridsen, M Thomsen, T H Jensen, M Bech, L B Christensen, E V Olsen, M Hviid, R Feidenhans'l and F Pfeiffer. *X-ray tomography using the full complex index of refraction.* Phys. Med. Biol., vol. 57, issue no. 19, art. no. 5971–5979, Sep 2012. (Cited on page 99.)

[Nilsen & Monteiro 1993] A Ulrik Nilsen and Paulo JM Monteiro. *Concrete: a three phase material.* Cem. Concr. Res., vol. 23, issue no. 1, art. no. 147–151, 1993. (Cited on page 95.)

[Noël *et al.* 2013] Peter B. Noël, Julia Herzen, Alexander A. Fingerle, Marian Willner, Marco K. Stockmar, Dieter Hahn, Marcus Settles, Enken Drecoll, Irene Zanette, Timm Weitkamp and et al. *Evaluation of the potential of phase-contrast computed tomography for improved visualization of cancerous human liver tissue.* Zeitschrift für Medizinische Physik, vol. 23, issue no. 3, pages 204–211, Sep 2013. (Cited on page 75.)

[Nugent *et al.* 1996] K. A. Nugent, T. E. Gureyev, D. F. Cookson, D. Paganin and Z. Barnea. *Quantitative Phase Imaging Using Hard X Rays.* Physical Review Letters, vol. 77, issue no. 14, pages 2961–2964, Sep 1996. (Cited on page 16.)

[Paganin & Nugent 1998] D. Paganin and K. Nugent. *Noninterferometric Phase Imaging with Partially Coherent Light.* Phys. Rev. Lett., vol. 80, issue no. 12, art. no. 2586–2589, Mar 1998. (Cited on page 97.)

[Paganin *et al.* 2002] D. Paganin, S. C. Mayo, T. E. Gureyev, P. R. Miller and S. W. Wilkins. *Simultaneous phase and amplitude extraction from a single defocused image of a homogeneous object.* J Microsc, vol. 206, issue no. 1, pages 33–40, Apr 2002. (Cited on page 16.)

[Paganin 2006] D. M. Paganin. Coherent X-ray Optics. Oxford University Press, England, 2006. (Cited on page 9.)

[Pagot *et al.* 2003] E. Pagot, P. Cloetens, S. Fiedler, A. Bravin, P. Coan, J. Baruchel, J. Haertwig and W. Thomlinson. *A method to extract quantitative information in analyzer-based x-ray phase contrast imaging.* Appl. Phys. Lett., vol. 82, issue no. 20, art. no. 3421, 2003. (Cited on page 16.)

[Parisatto *et al.* 2014] Matteo Parisatto, Maria Chiara Dalconi, Luca Valentini, Gilberto Artioli, Alexander Rack, Rémi Tucoulou, Giuseppe Cruciani and Giorgio Ferrari. *Examining microstructural evolution of Portland cements by in-situ synchrotron micro-tomography.* J. Mater. Sci., vol. 50, issue no. 4, art. no. 1805–1817, Dec 2014. (Cited on page 93.)

[Pfeiffer *et al.* 2006] Franz Pfeiffer, Timm Weitkamp, Oliver Bunk and Christian David. *Phase retrieval and differential phase-contrast imaging with low-brilliance X-ray sources.* Nature Phys., vol. 2, issue no. 4, pages 258–261, Mar 2006. (Cited on pages 2, 17, 20 and 24.)

[Pfeiffer *et al.* 2007a] F Pfeiffer, O Bunk, C David, M Bech, G Le Duc, A Bravin and P Cloetens. *High-resolution brain tumor visualization using three-dimensional x-ray phase contrast tomography.* Phys. Med. Biol., vol. 52, issue no. 23, pages 6923–6930, Nov 2007. (Cited on pages 1 and 75.)

[Pfeiffer *et al.* 2007b] F. Pfeiffer, O. Bunk, C. Kottler and C. David. *Tomographic reconstruction of three-dimensional objects from hard X-ray differential phase contrast projection images.* Nucl. Instrum. Meth. A, vol. 580, issue no. 2, pages 925–928, 2007. (Cited on page 17.)

[Pfeiffer *et al.* 2007c] F. Pfeiffer, C. Kottler, O. Bunk and C. David. *Hard X-ray phase tomography with low-brilliance sources.* Phys. Rev. Lett., vol. 98, issue no. 10, art. no. 108105, 2007. (Cited on pages 20 and 21.)

[Pfeiffer *et al.* 2008] F. Pfeiffer, M. Bech, O. Bunk, P. Kraft, E. F. Eikenberry, C. Bronnimann, C. Gruenzweig and C. David. *Hard-X-ray dark-field imaging using a grating interferometer.* Nature Materials, vol. 7, issue no. 2, pages 134–137, 2008. (Cited on pages 39 and 52.)

[Pfeiffer *et al.* 2013] Franz Pfeiffer, Julia Herzen, Marian Willner, Michael Chabior, Sigrid Auweter, Maximilian Reiser and Fabian Bamberg. *Grating-based X-ray phase contrast for biomedical imaging applications*. Zeitschrift für Medizinische Physik, vol. 23, issue no. 3, pages 176–185, Sep 2013. (Cited on page 75.)

[Pflederer *et al.* 2009] Tobias Pflederer, Larissa Rudofsky, Dieter Ropers, Sven Bachmann, Mohamed Marwan, Werner G. Daniel and Stephan Achenbach. *Image Quality in a Low Radiation Exposure Protocol for Retrospectively ECG-Gated Coronary CT Angiography*. American Journal of Roentgenology, vol. 192, issue no. 4, pages 1045–1050, Apr 2009. (Cited on page 87.)

[Poludniowski *et al.* 2009] G Poludniowski, G Landry, F DeBlois, P M Evans and F Verhaegen. *SpekCalc a program to calculate photon spectra from tungsten anode x-ray tubes*. Phys. Med. Biol., vol. 54, issue no. 19, pages N433–N438, Sep 2009. (Cited on page 51.)

[Qi *et al.* 2010] Zhihua Qi, Joseph Zambelli, Nicholas Bevins and Guang-Hong Chen. *Quantitative imaging of electron density and effective atomic number using phase contrast CT*. Phys. Med. Biol., vol. 55, issue no. 9, art. no. 2669–2677, Apr 2010. (Cited on pages 3 and 99.)

[Ranger *et al.* 2007] Nicole T. Ranger, Ehsan Samei, James T. Dobbins and Carl E. Ravin. *Assessment of Detective Quantum Efficiency: Intercomparison of a Recently Introduced International Standard with Prior Methods 1*. Radiology, vol. 243, issue no. 3, pages 785–795, Jun 2007. (Cited on page 33.)

[Raupach & Flohr 2011] Rainer Raupach and Thomas G Flohr. *Analytical evaluation of the signal and noise propagation in x-ray differential phase-contrast computed tomography*. Phys. Med. Biol., vol. 56, issue no. 7, pages 2219–2244, Apr 2011. (Cited on pages 60 and 84.)

[Raupach & Flohr 2012] Rainer Raupach and Thomas Flohr. *Performance evaluation of x-ray differential phase contrast computed tomography (PCT) with respect to medical imaging*. Med. Phys., vol. 39, issue no. 8, art. no. 4761, 2012. (Cited on pages 75, 82, 90 and 91.)

[Revol *et al.* 2010] Vincent Revol, Christian Kottler, Rolf Kaufmann, Ulrich Straumann and Claus Urban. *Noise analysis of grating-based x-ray differential phase contrast imaging*. Review of Scientific Instruments, vol. 81, issue no. 7, art. no. 073709, 2010. (Cited on pages 69 and 70.)

[Reznikova *et al.* 2008] Elena Reznikova, Juergen Mohr, Martin Boerner, Vladimir Nazmov and Peter-Juergen Jakobs. *Soft X-ray lithography of high aspect ratio SU8 submicron structures*. Microsyst. Technol., vol. 14, issue no. 9-11, pages 1683–1688, Jan 2008. (Cited on pages 2, 32 and 48.)

[Ruiz-Yaniz *et al.* 2015] M. Ruiz-Yaniz, I. Zanette, A. Rack, T. Weitkamp, P. Meyer, J. Mohr and F. Pfeiffer. *X-ray-refractive-index measurements at photon energies above 100 keV with a grating interferometer*. Phys. Rev. A, vol. 91, issue no. 3, art. no. 033803, Mar 2015. (Cited on pages 3 and 47.)

[Sarapata *et al.* 2014a] A. Sarapata, M. Chabior, C. Cozzini, J. I. Sperl, D. Bequé, O. Langner, J. Coman, I. Zanette, M. Ruiz-Yaniz and F. Pfeiffer. *Quantitative electron density characterization of soft tissue substitute plastic materials using grating-based x-ray phase-contrast imaging*. Review of Scientific Instruments, vol. 85, issue no. 10, art. no. 103708, Oct 2014. (Cited on pages 37, 41, 42 and 43.)

[Sarapata *et al.* 2014b] A. Sarapata, J. W. Stayman, M. Finkenthal, J. H. Siewerdsen, F. Pfeiffer and D. Stutman. *High energy x-ray phase contrast CT using glancing-angle grating interferometers*. Med. Phys., vol. 41, issue no. 2, art. no. 021904, Feb 2014. (Cited on pages 47, 78, 82, 83, 85, 86, 87, 88 and 89.)

[Sarapata *et al.* 2015a] A Sarapata, M Ruiz-Yaniz, I Zanette, A Rack, F Pfeiffer and J. Herzen. *Multi-contrast 3D X-ray imaging of porous and composite materials*. Appl. Phys. Lett., vol. 106, April 2015. (Cited on pages 96 and 97.)

[Sarapata *et al.* 2015b] Adrian Sarapata, Marian Willner, Marco Walter, Thomas Duttenhofer, Konradin Kaiser, Pascal Meyer, Christian Braun, Alexander Fingerle, Peter B. Noël, Franz Pfeiffer and et al. *Quantitative imaging using high-energy X-ray phase-contrast CT with a 70 kVp polychromatic X-ray spectrum*. Optics Express, vol. 23, issue no. 1, art. no. 523, 2015. (Cited on pages 50, 54, 55, 56, 57, 58 and 85.)

[Scherer *et al.* 2014] Kai Scherer, Lorenz Birnbacher, Michael Chabior, Julia Herzen, Doris Mayr, Susanne Grandl, Aniko' Sztro'kay-Gaul, Karin Hellerhoff, Fabian Bamberg and Franz Pfeiffer. *Bi-Directional X-Ray Phase-Contrast Mammography*. PLoS ONE, vol. 9, issue no. 5, art. no. e93502, May 2014. (Cited on page 2.)

[Scholkmann *et al.* 2014] Felix Scholkmann, Vincent Revol, Rolf Kaufmann, Heidrun Baronowski and Christian Kottler. *A new method for fusion, denoising and enhancement of x-ray images retrieved from Talbot-Lau grating interferometry*. Phys. Med. Biol., vol. 59, issue no. 6, art. no. 1425–1440, Feb 2014. (Cited on page 100.)

[Schulz *et al.* 2010] G. Schulz, T. Weitkamp, I. Zanette, F. Pfeiffer, F. Beckmann, C. David, S. Rutishauser, E. Reznikova and B. Muller. *High-resolution tomographic imaging of a human cerebellum: comparison of absorption and grating-based phase contrast*. Journal of The Royal Society Interface, vol. 7, issue no. 53, pages 1665–1676, Jul 2010. (Cited on pages 1 and 47.)

[Shemesh *et al.* 2012] Noam Shemesh, Carl-Fredrik Westin and Yoram Cohen. *Magnetic Resonance Imaging by Synergistic Diffusion-Diffraction Patterns*. Phys. Rev. Lett., vol. 108, issue no. 5, art. no. 058103, Jan 2012. (Cited on page 93.)

[Singh *et al.* 2012] Sarabjeet Singh, Mannudeep K. Kalra, Synho Do, Jean Baptiste Thibault, Homer Pien, Owen O. J. Connor and Michael A. Blake. *Comparison of Hybrid and Pure Iterative Reconstruction Techniques With Conventional Filtered Back Projection*. Journal of Computer Assisted Tomography, vol. 36, issue no. 3, pages 347–353, 2012. (Cited on pages 89 and 90.)

[Snigirev *et al.* 1995] A. Snigirev, I. Snigireva, V. Kohn, S. Kuznetsov and I. Schelokov. *On the possibilities of x-ray phase contrast microimaging by coherent high-energy synchrotron radiation*. Review of Scientific Instruments, vol. 66, issue no. 12, art. no. 5486, 1995. (Cited on page 16.)

[Stampanoni *et al.* 2011] Marco Stampanoni, Zhentian Wang, Thomas Thüring, Christian David, Ewald Roessl, Mafalda Trippel, Rahel A. Kubik-Huch, Gad Singer, Michael K. Hohl and Nik Hauser. *The First Analysis and Clinical Evaluation of Native Breast Tissue Using Differential Phase-Contrast Mammography*. Investigative Radiology, vol. 46, issue no. 12, pages 801–806, 2011. (Cited on page 2.)

[Stutman & Finkenthal 2012] D. Stutman and M. Finkenthal. *Glancing angle Talbot-Lau grating interferometers for phase contrast imaging at high x-ray energy*. Appl. Phys. Lett., vol. 101, issue no. 9, art. no. 091108, 2012. (Cited on pages 60 and 76.)

[Stutman & Finkenthal 2014] Dan Stutman and Michael Finkenthal. *Large field of view grating interferometers for x-ray phase contrast imaging and ct at high energy*, February 10 2014. US Patent App. 14/176,655. (Cited on page 83.)

[Stutman *et al.* 2011] Dan Stutman, Thomas J Beck, John A Carrino and Clifton O Bingham. *Talbot phase-contrast x-ray imaging for the small joints of the hand*. Phys. Med. Biol., vol. 56, issue no. 17, pages 5697–5720, Aug 2011. (Cited on page 75.)

[Stutman *et al.* 2013] D. Stutman, J. W. Stayman, M. Finkenthal and J. H. Siewerdsen. *High energy x-ray phase-contrast imaging using glancing angle grating interferometers*. Medical Imaging 2013: Physics of Medical Imaging, Mar 2013. (Cited on pages 77, 81, 84 and 90.)

[Tang *et al.* 2011] Xiangyang Tang, Yi Yang and Shaojie Tang. *Characterization of imaging performance in differential phase contrast CT compared with the conventional CT - Noise power spectrum NPS(k)*. Med. Phys., vol. 38, issue no. 7, art. no. 4386, 2011. (Cited on page 76.)

[Tapfer *et al.* 2013] Arne Tapfer, Rickmer Braren, Martin Bech, Marian Willner, Irene Zanette, Timm Weitkamp, Marija Trajkovic-Arsic, Jens T. Siveke, Marcus Settles, Michaela Aichler and et al. *X-Ray Phase-Contrast CT of a Pancreatic Ductal Adenocarcinoma Mouse Model.* PLoS ONE, vol. 8, issue no. 3, art. no. e58439, Mar 2013. (Cited on page 75.)

[Tapiovaara & Siiskonen] M. Tapiovaara and T. Siiskonen. *PCXMC, a Monte Carlo program for calculating patient doses in medical x-ray examinations*, stuk-a231 2nd édition. (Cited on page 81.)

[Thibault *et al.* 2007] Jean-Baptiste Thibault, Ken D. Sauer, Charles A. Bouman and Jiang Hsieh. *A three-dimensional statistical approach to improved image quality for multislice helical CT.* Med. Phys., vol. 34, issue no. 11, art. no. 4526, 2007. (Cited on page 90.)

[Thuering *et al.* 2014] T. Thuering, M. Abis, Z. Wang, C. David and M. Stampanoni. *X-ray phase-contrast imaging at 100 keV on a conventional source.* Sci. Rep., vol. 4, art. no. 5198, Jun 2014. (Cited on pages 3 and 47.)

[Trtik *et al.* 2013] Pavel Trtik, Ana Diaz, Manuel Guizar-Sicairos, Andreas Menzel and Oliver Bunk. *Density mapping of hardened cement paste using ptychographic X-ray computed tomography.* Cem. Concr. Compos., vol. 36, art. no. 71–77, Feb 2013. (Cited on pages 94 and 100.)

[Vedantham & Karellas 2013] Srinivasan Vedantham and Andrew Karellas. *X-ray phase contrast imaging of the breast: Analysis of tissue simulating materials.* Med. Phys., vol. 40, issue no. 4, art. no. 041906, 2013. (Cited on page 45.)

[Vogel & Oman 1996] C. R. Vogel and M. E. Oman. *Iterative Methods For Total Variation Denoising.* SIAM J. SCI. COMPUT, vol. 17, pages 227–238, 1996. (Cited on page 90.)

[Wang *et al.* 2009] Zhen-Tian Wang, Ke-Jun Kang, Zhi-Feng Huang and Zhi-Qiang Chen. *Quantitative grating-based x-ray dark-field computed tomography.* Appl. Phys. Lett., vol. 95, issue no. 9, art. no. 094105, 2009. (Cited on pages 18, 20 and 94.)

[Wang *et al.* 2013] Z Wang, C A Clavijo, E Roessl, U van Stevendaal, T Koehler, N Hauser and M Stampanoni. *Image fusion scheme for differential phase contrast mammography.* J. Instrum., vol. 8, issue no. 07, art. no. C07011, Jul 2013. (Cited on page 100.)

[Weitkamp *et al.* 2005] T. Weitkamp, A. Diaz, C. David, F. Pfeiffer, M. Stampanoni, P. Cloetens and E. Ziegler. *X-ray phase imaging with a grating interferometer.* Opt. Express, vol. 13, issue no. 16, pages 6296–6304, 2005. (Cited on pages 17, 20 and 28.)

[Weitkamp *et al.* 2006] Timm Weitkamp, Christian David, Christian Kottler, Oliver Bunk and Franz Pfeiffer. *Tomography with grating interferometers at low-brilliance sources*. Developments in X-Ray Tomography V, Aug 2006. (Cited on pages 21, 24, 30 and 31.)

[Weitkamp *et al.* 2010] Timm Weitkamp, Irene Zanette, Christian David, Jose Baruchel, Martin Bech, Pascal Bernard, Hans Deyhle, Tilman Donath, Johannes Kenntner, Sabrina Lang, Jürgen Mohr, Bert Müller, Franz Pfeiffer, Elena Reznikova, Simon Rutishauser, Georg Schulz, Arne Tapfer and Jean-Paul Valade. *Recent developments in x-ray Talbot interferometry at ESRF-ID19*. Proc. SPIE, vol. 7804, pages 780406–780406–10, 2010. (Cited on pages 39 and 94.)

[White *et al.* 1977a] D. R. White, R. J. Martin and R. Darlison. *Epoxy resin based tissue substitutes*. The British Journal of Radiology, vol. 50, issue no. 599, pages 814–821, Nov 1977. (Cited on page 63.)

[White *et al.* 1977b] DR White, RJ Martin and R Darlison. *Epoxy resin based tissue substitutes*. 1977. (Cited on pages 36 and 66.)

[White 1978] D. R. White. *Tissue substitutes in experimental radiation physics*. Medical Physics, vol. 5, issue no. 6, 1978. (Cited on page 40.)

[Wilkins *et al.* 1996] S. W. Wilkins, T. E. Gureyev, D. Gao, A. Pogany and A. W. Stevenson. *Phase-contrast imaging using polychromatic hard X-rays*. Nature, vol. 384, issue no. 6607, pages 335–338, Nov 1996. (Cited on page 17.)

[Willner *et al.* 2013] Marian Willner, Martin Bech, Julia Herzen, Irene Zanette, Dieter Hahn, Johannes Kenntner, Juergen Mohr, Alexander Rack, Timm Weitkamp and Franz Pfeiffer. *Quantitative X-ray phase-contrast computed tomography at 82 keV*. Opt. Express, vol. 21, issue no. 4, art. no. 4155, Feb 2013. (Cited on pages 3, 47, 48, 50, 51 and 59.)

[Willner *et al.* 2014] M Willner, J Herzen, S Grandl, S Auweter, D Mayr, A Hipp, M Chabior, A Sarapata, K Achterhold, I Zanette and et al. *Quantitative breast tissue characterization using grating-based x-ray phase-contrast imaging*. Phys. Med. Biol., vol. 59, issue no. 7, pages 1557–1571, Mar 2014. (Cited on pages 2, 47, 63 and 66.)

[Wilson 1950] A. J. C. Wilson. The optical principles of the diffraction of x-rays by r.w. james, volume III. International Union of Crystallography (IUCr), Jan 1950. (Cited on pages 14 and 49.)

[Wu *et al.* 2003] X. Wu, A. E. Deans and H. Liu. Biomedical photonics handbook. CRC Press, 2003. (Cited on page 77.)

[Yaffe *et al.* 2009] M. J. Yaffe, J. M. Boone, N. Packard, O. Alonzo-Proulx, S.-Y. Huang, C. L. Peressotti, A. Al-Mayah and K. Brock. *The myth of the 50–50 breast.* Med. Phys., vol. 36, issue no. 12, art. no. 5437, 2009. (Cited on page 67.)

[Yang *et al.* 2014] F. Yang, F. Prade, M. Griffa, I. Jerjen, C. Di Bella, J. Herzen, A. Sarapata, F. Pfeiffer and P. Lura. *Dark-field X-ray imaging of unsaturated water transport in porous materials.* Appl. Phys. Lett., vol. 105, issue no. 15, art. no. 154105, Oct 2014. (Cited on page 100.)

[Yaroshenko *et al.* 2014] Andre Yaroshenko, Katharina Hellbach, Martin Bech, Susanne Grandl, Maximilian F. Reiser, Franz Pfeiffer and Felix G. Meinel. *Grating-based X-ray dark-field imaging: a new paradigm in radiography.* Curr. Radiol. Rep., vol. 2, issue no. 7, art. no. 1–9, May 2014. (Cited on page 100.)

[Yohannes *et al.* 2012] Indra Yohannes, Daniel Kolditz, Oliver Langner and Willi A Kalender. *A formulation of tissue- and water-equivalent materials using the stoichiometric analysis method for CT-number calibration in radiotherapy treatment planning.* Physics in Medicine and Biology, vol. 57, issue no. 5, art. no. 1173, 2012. (Cited on page 40.)

[Yoon *et al.* 2012] Min A. Yoon, Se Hyung Kim, Jeong Min Lee, Hyoun Sik Woo, Eun Sun Lee, Se Jin Ahn and Joon Koo Han. *Adaptive Statistical Iterative Reconstruction and Veo.* Journal of Computer Assisted Tomography, vol. 36, issue no. 5, pages 596–601, 2012. (Cited on page 90.)

[Zanette *et al.* 2012] I. Zanette, M. Bech, A. Rack, G. Le Duc, P. Tafforeau, C. David, J. Mohr, F. Pfeiffer and T. Weitkamp. *Trimodal low-dose X-ray tomography.* Proceedings of the National Academy of Sciences, vol. 109, issue no. 26, pages 10199–10204, 2012. (Cited on pages 78 and 79.)

[Zanette *et al.* 2013] Irene Zanette, Timm Weitkamp, Geraldine Le Duc and Franz Pfeiffer. *X-ray grating-based phase tomography for 3D histology.* RSC Adv., vol. 3, issue no. 43, art. no. 19816, 2013. (Cited on page 1.)

[Zbijewski *et al.* 2011] W. Zbijewski, P. De Jean, P. Prakash, Y. Ding, J. W. Stayman, N. Packard, R. Senn, D. Yang, J. Yorkston, A. Machado and et al. *A dedicated cone-beam CT system for musculoskeletal extremities imaging: Design, optimization, and initial performance characterization.* Med. Phys., vol. 38, issue no. 8, art. no. 4700, 2011. (Cited on pages 84 and 90.)

[Zhu *et al.* 2010] P. Zhu, K. Zhang, Z. Wang, Y. Liu, X. Liu, Z. Wu, S. A. McDonald, F. Marone and M. Stampanoni. *Low-dose, simple, and fast grating-based X-ray phase-contrast imaging.* Proceedings of the National Academy of Sciences, vol. 107, issue no. 31, pages 13576–13581, Jul 2010. (Cited on page 91.)

[Zingg *et al.* 2008] Anatol Zingg, Lorenz Holzer, Andres Kaech, Frank Winnefeld, Joachim Pakusch, Stefan Becker and Ludwig Gauckler. *The microstructure of dispersed and non-dispersed fresh cement pastes – New insight by cryo-microscopy.* Cem. Concr. Res., vol. 38, issue no. 4, pages 522–529, Apr 2008. (Cited on page 93.)

List of publications

Peer-reviewed publications as first author:

1. A. Sarapata, M. Ruiz-Yaniz, I. Zanette, A. Rack, F. Pfeiffer, and J. Herzen, "Multi-contrast 3D X-ray imaging of porous and composite materials," Applied Physics Letters **106**, 16 (2015).

2. A. Sarapata, M. Willner, M. Walter, T. Duttenhofer, K. Kaiser, P. Meyer, C. Braun, A. Fingerle, P. B. Noël, F. Pfeiffer, and J. Herzen, "Quantitative imaging using high-energy X-ray phase-contrast CT with a 70 kVp polychromatic X-ray spectrum," Optics Express **23**, 523-535 (2015).

3. A. Sarapata, JW. Stayman, M. Finkenthal, JH. Siewerdsen, F. Pfeiffer, D. Stutman, "High energy X-ray phase contrast CT using glancing-angle grating interferometers," Medical Physics **41**, 021904 (2014).

4. A. Sarapata, M. Chabior, C. Cozzini, J. I. Sperl, D. Bequé, O. Langner, J. Coman, I. Zanette, M. Ruiz-Yaniz and F. Pfeiffer, "Quantitative electron density characterization of soft tissue substitute plastic materials using grating-based X-ray phase-contrast imaging," Review of Scientific Instruments **98**, 094101 (2014).

Peer-reviewed publications as co-author:

5. F. Yang, F. Prade, M. Griffa, I. Jerjen, C. Di Bella, J. Herzen, A. Sarapata, F. Pfeiffer, and P. Lura, "Dark-field X-ray imaging of unsaturated water transport in porous materials", Applied Physics Letters **105**, 154105 (2014).

6. M. Willner, J. Herzen, S. Grandl, S. Auweter, D. Mayr, A. Hipp, M. Chabior, A. Sarapata, K. Achterhold, I. Zanette, T. Weitkamp, A. Sztrókay, K. Hellerhoff, M. Reiser and F. Pfeiffer, "Quantitative breast tissue characterization using grating-based x-ray phase-contrast imaging", Physics in Medicine and Biology **59**, 1557-1571 (2014).

List of scientific presentations

Oral presentations:

1. Title: *"Taking Grating-based X-ray Phase Contrast Imaging to Clinically Relevant X-ray Energies"*, presentation at the **Radiological Society of North America (RSNA) Conference**, 30th November 2014, Chicago (USA).

2. Title: *"Multi-contrast imaging with X-ray Talbot(-Lau) interferometry for materials science applications"*, invited lecture at the **EMPA - Swiss Federal Laboratories for Materials Science and Technology**, 30th October 2014, Dübendorf (SWITZERLAND).

Poster presentations:

1. Title: *"A high fringe visibility glancing-angle grating interferometer for high energy X-ray phase contrast CT"* at the **International Workshop on X-ray and Neutron Phase Imaging with Gratings**, Garmisch-Partnekirchen, Germany, January 2014.

2. Title: *"A high fringe visibility glancing-angle grating interferometer for high energy X-ray phase contrast CT"* at the **Industrial CT Scanning, German-Austrian-Danish Workshop**, Garching, Germany, October 2013.

Acknowledgements

This thesis has only one author on the cover, but the work that went into its creation was a collaboration of many people. Here I would like to thank all of them for any type of contribution, small or big, scientific or personal. This thesis would have never been created and finished without the help of all those people.

First and foremost, a big 'thank you' goes to my scientific supervisor, Prof. Franz Pfeiffer, who accepted me at his group and guided me through the tough beginnings of grating interferometry. Looking at his accomplishments in the field of X-ray imaging was always inspiring and motivating to push myself forward. Additionally, thank you for providing the financial support and possibilities to share and exchange knowledge at numerous conferences and other scientific events. Oh, and for making me fall in love with the Bavarian Alps by hosting the Seminar Days there.

With many ideas and ways of doing things, sometimes it could be challenging to stay on the right track. Dr. Julia Herzen was always there to guide me, show me the right way, answer my countless questions, and make grating interferometry more bearable. Thank you for that. Same goes to Dr. Michael Chabior who stepped in Julia's shoes when she was absent from the group.

I would like to thank Dr. Dan Stutman, the researcher at Johns Hopkins University for his support and supervision during my stay at his group. Thanks to him I have learned how to look at things from a new perspective, which I believe strongly contributed to a successful completion of this thesis.

My gratitude goes to my collaborators from GE Research Center, namely Cristina Cozzini, Jonathan Sperl, and Dirk Bequé, for keeping me motivated through the weekly meetings and showing me a sneak peek into the 'corporate' world. It was enough for me to 'jump ship' and start working for a company myself.

During my work on this thesis, I had the opportunity to collaborate with Oliver Langner and Johannes Coman from QRM GmbH. Thank you for providing high-quality phantoms and answering my countless emails concerning medical phantoms.

I would like to thank the whole E17 group for a great time, especially my "Grossraumbuero" mates from the IMETUM for the amazing atmosphere during working hours and beyond. I simply cannot emphasize how great it was to work being surrounded by so many interesting and fun people. During my first weeks Dr. Guillaume Potdevin, Thomas Biernath and Andreas Malecki welcomed me into the IMETUM and introduced me to the experimental setup that they built and I could later use for this thesis. Furthermore, I would like to thank Johannes Wolf, Andre Yaroshenko, Sebastian Allner, Lorenz Birnbacher, Christoph Jud, Mathias Marschner, Mark Mueller, Friedrich Prade, Florian Schaff, Kai Scherer, Jonathan

Schock, Markus Schüttler, Saeed Seyyedi, Yash Sharma, Max von Teuffenbach, Marian Willner, Konstantin Böll, Marco Stockmar, Gabriel Fior, Regine Gradl, Constantin Nottbeck, Marie-Christine Zdora and others for the very enjoyable time during working hours and beyond. Yet another special thanks goes to Pidassa Bidola, Karin Burger, Simone Ferstl and Jolanda Schwarz who were sharing the desks next to me and have always made me laugh. I would also like to thank Karin Burger for proof-reading some of the chapters of this thesis and being an amazing "*Masterin of the Ceremony*".

A big part of this thesis was made possible thanks to the incredible bug-free CT reconstruction code written by Andreas Fehringer and the others. Thank you for that! Many of my late-night working hours were spared. My gratitude also goes to Martin Dierolf for keeping such good care of all the computational servers and helping me solve numerous Linux problems.

Living abroad can sometimes be quite challenging. Special thanks to Maite Ruiz and Juliana Martins for making it a bit less difficult by being such great friends.

I would like to thank Sigrid Auweter for her excellent project management and amazing organization skills that I had the pleasure to experience during the preparation of the XNPIG conference in Garmisch-Partenkirchen, Germany in 2014. I have learned a lot and will use that knowledge in my future career.

I would like to thank Nelly de Leris and Klaus Achterhold for helping me with all the administrative work and Brunhilde Vogt for reminding me of the existence of a dosimeter in one of my drawers and the necessity to wear it. Possibly without it I would glow in the dark by now, due to excessive radiation doses.

A very special 'thank you' goes to Luca Silvi from the nuclear reactor for the countless lunches at IPP and the time spent together outside of the university. When I started working at TUM I never imagined I would meet such a good friend for life. *Grazie mille!*

Serdeczne podziękowania dla mojej mamy i babci, które mnie zawsze wspierały i były ze mnie dumne, nawet na odległość. Serdeczne podziękowania należą się rownież mojej cioci Miłoszy i moim kuzynkom, Ewelinie i Sarze za wsparcie i wiarę w moje możliwości.

Last but not least, thanks to Adam Woś for sharing the expat life in Germany with me, all the amazing trips we have made together, teaching me how to properly pronounce grating interferometry and keeping my Polish language 'afloat'. Dziękuje!